Annual Report 1999

AG Magnetismus
Universität Kaiserslautern

Address: Prof. Dr. Burkard Hillebrands
Fachbereich Physik
Universität Kaiserslautern
Erwin-Schrödinger-Straße 56
67663 Kaiserslautern, Germany

Tel.: +49-(0)631-205-4228
Fax: +49-(0)631-205-4095

Postal address: Postfach 3049
67653 Kaiserslautern, Germany

Internet: http://www.physik.uni-kl.de/w_hilleb/w_hilleb.html
E-Mail: hilleb@physik.uni-kl.de

Our Group

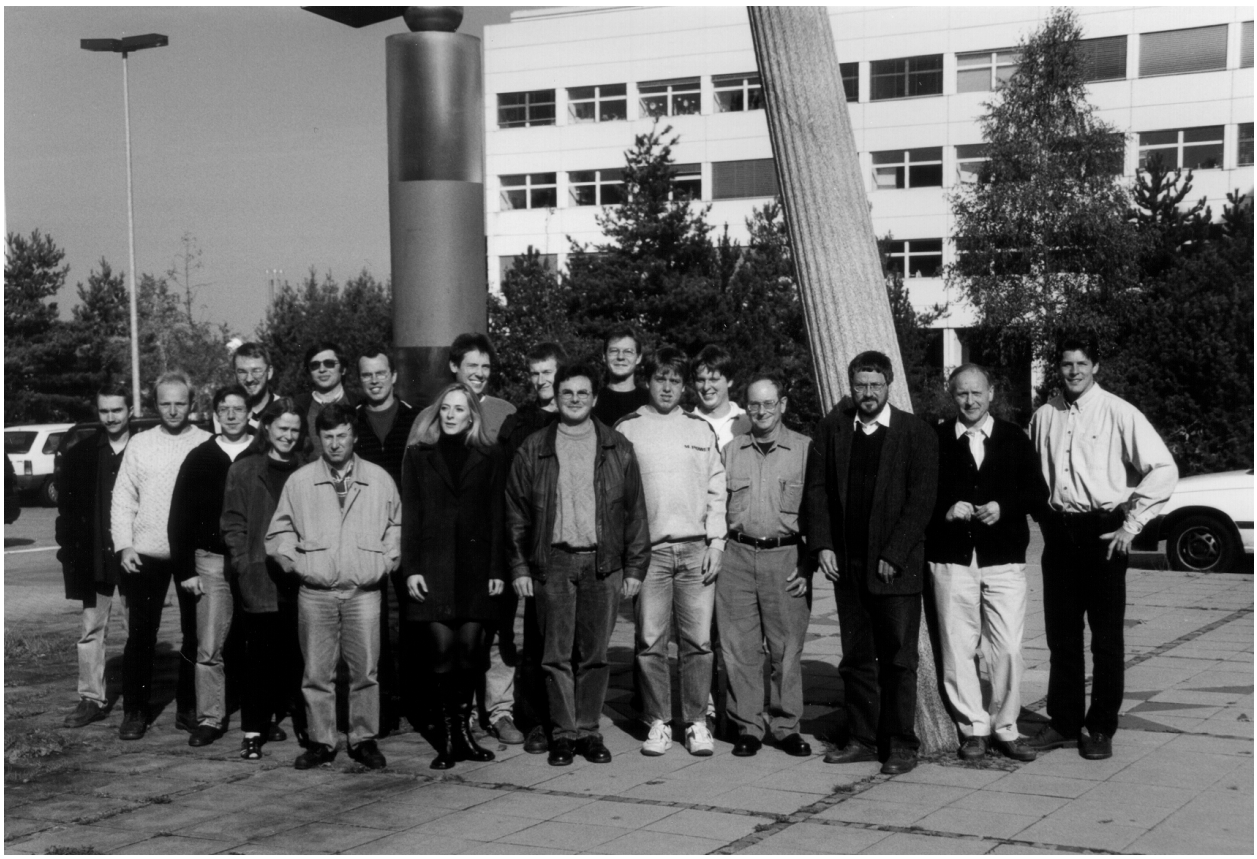

From left to right:

Andreas Rueff, Christian Krämer, Thomas Wittkowski, Tim Mewes, Sybille Müller, Dr. Serguei Demokritov, Bernd Pfaff, Dr. Jürgen Fassbender, Dr. Alexandra Mougin, Oliver Büttner, Stefan Poppe, Martin Bauer, Jörg Jorzick, Radek Lopusnik, Björn Roos, Prof. Dr. Carl Patton, Prof. Dr. Burkard Hillebrands, Dr. Kurt Jung, Marc Rickart.

This report contains unpublished results and should
not be quoted without permission from the authors.

Contents

Chapter 1: Introduction

Dear colleagues and friends,

This is the third annual report on our work, and it covers the period November 1998 to October 1999. We shifted the report period away from the calendar year. October is a good month for writing the report, before classes start, and you may now receive this report before Christmas (so you may read it during your Christmas vacation).

Our main research interest is in magneto-electronics, which has developed into an extremely exciting and productive area. We are increasingly involved in a number of fields related to magneto-electronics, such as the dynamic properties in small magnetic elements and fast switching processes, new tunnel barriers, the growth of epitaxial semiconductor–metal and insulator–metal systems, and exchange bias systems. Highlights of our work in 1999 are: i) Progress in time resolved techniques, both in magneto-optic Kerr effect and in Brillouin light scattering experiments. We report a periodic change in the magnetic ringing in small magnetic structures as a function of the length of a short applied field pulse, and a better understanding of the quantized dynamic modes in magnetic films patterned into wires, dots, squares and rectangles. ii) Fabrication of magnetic tunnel junctions using a novel method for making oxide or nitride barriers. iii) Growth of vicinal magnetic films on insulating and semiconducting substrates. iv) Progress in the fabrication of exchange bias systems, the tailoring of exchange bias by ion irradiation, and the observation of oscillating exchange bias as a function of a nonmagnetic spacer layer between the ferromagnetic and antiferromagnetic layer.

Two new experimental setups are now in operation. Our TIMO experiment is working (TIMO stands for time resolved magneto-optic Kerr magnetometry), which allows one to study the temporal response of the magnetization with spatial resolution upon application of a short magnetic field pulse. Results are reported in Sect. 6.11 and 6.21. A new, second Brillouin light scattering setup has been put into operation. It is equipped with the lately improved Sandercock setup which now contains an interface to the computer control we have developed (see Sect. 6.20).

Our work within magneto-electronics and related areas is part of four international and national networks: the TMR-Dynaspin network funded by the European Union, the network "Nanomagnetism and growth processes on vicinal surfaces" funded by the European Science Foundation, the "Leitprojekt Magnetoelektronik" funded by the Bundesministerium für Bildung und Forschung (BMBF) and industry, and the Center of Competence "Nanoclub Lateral", also funded by the BMBF and industry.

A big event this September was the summer school on "Mesomagnetism, Spin Dynamics and Spin Electronics", jointly organized by the European TMR networks "Dynaspin" and "Submagdev", in Rhodes, Greece. The subject of the school was very close to our activities, and we contributed with two lectures, 6 posters, and 12 attending group members. Impressions from this meeting are shown in the Appendix.

Since January 1st I am heading the Center for Technology Transfer "Hard and wear resistant coatings", founded by now retired Prof. H. Ehrhardt in 1993. Since 1997 the Center is now located at the state operated Technologiezentrum Oberflächen (TZO, Center for Technology of Surfaces) in Rheinbreitbach, a village at the northern boundary of Rheinland-Pfalz near to Bad Honnef, serving the northern area of our state and the Bonn-Cologne industrial area of Nordrhein-Westfalen. The aim of the center is the transfer of knowledge to local industry, preferably small companies and start ups in the field of hard coatings and wear resistant films.

Within this center there is a state-run initiative to incubate new high-tech companies, preferably those emerging from university laboratories. In a first project, Dr. H. Busch and Dr. U. Grabowy have developed stents used to widen a heart artery using nuclear activated coatings to avoid the problem of restenosis. Their project is described in Sect. 6.23.

In August two new long-term guests have arrived. Prof. Dr. Carl E. Patton from Colorado State University spends a sabbatical year funded by the Alexander von Humboldt foundation. He is a world-leading expert in nonlinear spin wave phenomena, and he joins our experiments on nonlinear spin wave propagation. Dr. Alexandra Mougin from the University of Nancy, France joined our group with funding by the European Community. She works in the area of spin dynamics and exchange bias systems.

It is a pleasure to greet all former members of our group via this report. May this annual report help us to stay in touch with each other.

Our work would not have been possible without valuable collaborations with people all over the world. I would like to thank, in alphabetical order, Bernard Bartenlian, Claude Chappert, John Cochran, Horst Dötsch, Claude Fermon, Zdenek Frait, Uwe Hartmann, Boris Kalinikos, Mikhail Kostylev, Achim Lunk, Fabrizio Nizzoli, Carl Patton, Yuri Rapoport, Theo Rasing, Frank Richter, Francoise Rousseaux, John R. Sandercock, Andrei Slavin, Elin Søndergard, Bob Stamps, Evgueni Tsymbal, and Stefan Visnovsky for their interactions with us and their strong input on our work. Collaborations within the Fachbereich Physik at the University of Kaiserslautern (Hans Oechsner, Hans Schmoranzer, Herbert Urbassek and Richard Wallenstein and their groups) and the Institut für Oberflächen- und Schichtanalytik (IFOS) have been very stimulating. I would also like to thank all sponsors, which are the Deutsche Forschungsgemeinschaft, the Bundesministerium für Bildung, Wissenschaft, Forschung und Technologie, the Siemens AG, the Humboldt Foundation, the European Community, the European Science Foundation, the State of Rheinland-Pfalz and the University of Kaiserslautern. My special thanks go to Tim Mewes and Sibylle Müller for their technical help in preparing this report.

If you are interested in our work we would be happy to hear from you. If you have any questions, comments, suggestions, or any kind of criticism, please contact us.

With all my best wishes for Christmas, and a Happy New Year,

Burkard Hillebrands

Kaiserslautern, November 1999

Chapter 2: Personnel

2.1 Members of the Group

Group leader:

Prof. Dr. Burkard Hillebrands

Senior scientists:

Dr. Serguei Demokritov, Wiss. Assistent
Dr. Jürgen Fassbender, Wiss. Assistent
Dr. Kurt Jung, Akad. Direktor

Postdoctoral fellows:

Dr. Alexandra Mougin	since 8/99
Dr. Yun-Jun Tang	until 1/99

PhD students:

Dipl.-Phys. Martin Bauer	
Dipl.-Phys. Oliver Büttner	
Dipl.-Phys. André Frank	
Dipl.-Phys. Jörg Jorzick	
Dipl. Phys. Radek Lopusnik	
Dipl. Phys. Tim Mewes	since 5/99
Dipl. Phys. Stefan Poppe	since 3/99
Dipl. Phys. Marc Rickart	since 1/99
Dipl.-Phys. Björn Roos	
Dipl.-Phys. Thomas Wittkowski	

Diploma students:

Catrin Guhrke	until 2/99
Tim Mewes	until 4/99
Stefan Poppe	until 2/99
Marc Rickart	until 12/98
Christian Krämer	since 9/99
Andreas Rueff	since 1/99

Technician:

Bernd Pfaff

Secretary:

Sibylle Müller

2.2 Visiting Scientists and Postdoctoral Fellows

Dr. Yun-Jun Tang	01.10.97 – 31.01.99
Dipl. Phys. Dimitri Kholin	01.07.99 – 30.09.99
Prof. Dr. Andrei Slavin	04.07.99 – 11.07.99
Dr. Alexandra Mougin	01.08.99 – 28.02.01
Prof. Dr. Carl Patton	16.08.99 – 13.07.00

Dr. Alexandra Mougin

Country: France
Visiting period: 01.08.99 to 28.02.01

I have done my Ph-D thesis entitled "RFe_2(110) magnetostrictive nanosystems (R is a rare earth): growth, morphology and magnetic properties" in Nancy, in the Laboratoire de Physique des Matériaux.

Single crystalline magnetostrictive compounds exhibiting strains and/or reduced dimensions are ideal candidates to study correlation between structure and magnetism.

Single crystalline RFe_2(110) have been grown by molecular beam epitaxy and obey the so-called Stranski Krastanov growth mode. Reflection High Energy Electron Diffraction and Atomic Force Microscopy demonstrate that the nanosystem morphology depends on elaboration parameters (substrate temperature, nominal thickness and lattice mismatch) and evolves from a continuous film with low surface roughness to anisotropic isolated structures.

Layers deposited directly on the buffer layer are submitted to a negative ε_{xy} shear, purely thermal whereas an elastic model account for strains in the RFe_2 / YFe_2(110) bilayer [1].

In RFe_2(110) layers, Mössbauer spectrometry and neutron diffraction show that the easy magnetization directions are modified in comparison with the bulk material ones: a spin reorientation can be induced in $DyFe_2$(110) and $ErFe_2$(110) layers whereas the thermal spin rotation is reduced in Terfenol-D and $SmFe_2$ epitaxial films. These observations are modeled by introducing the modification of the magnetoelastic energy, due to the shear. Both signs of the magnetoelastic constant and of ε_{xy} govern the perpendicular or in-plane behavior of the magnetization.

Moreover, the magnetization reversal processes have been shown to be related to the morphology of the samples [2].

My post doc position in the B. Hillebrands research group is financed by the DYNASPIN network and I am more particularly involved in the bias exchange studies.

The exchange biasing effect is associated with the exchange anisotropy created at the interface between ferromagnetic and antiferromagnetic layers, when the bilayer is cooled in a static magnetic field through the Néel temperature. The exchange bias field is known to be mainly influenced by the interface structure between the ferromagnetic and antiferromagnetic layers so that the understanding of exchange bias requires accurate studies of the linked structural and magnetic properties.

I expect that the stay here will be an opportunity for me to improve my knowledge in exchange bias coupling. Moreover, I hope that this work benefits my own abilities, concerning growth and magnetism.

References

[1] A. Mougin, C. Dufour, K. Dumesnil, N. Maloufi, Ph. Mangin, Phys. Rev. B **59**, 5950 (1999).
[2] K. Dumesnil, A. Mougin, C. Dufour, Ph. Mangin, J. Magn. Magn. Mater. **198-199**, 516 (1999).

Prof. Dr. Carl E. Patton

Country: USA
Visiting period: 16.08.99 to 13.07.00

I am a professor of physics at Colorado State University (CSU), Fort Collins, Colorado, USA. My research group at home is involved in research on microwave ferrite materials, nonlinear microwave dynamics in bulk and thin film magnetic materials, and microwave ferrite device development. This is my fourth sabbatical leave from Colorado. I am delighted to be spending it with Professor Hillebrand's group at the Universität Kaiserslautern under renewal support from the Alexander von Humboldt Foundation. As a somewhat younger academician twenty two years ago (1977), my first sabbatical leave from Colorado was also in Germany, at Freiburg Universität, and also under Humboldt Foundation support.

My main objective for this sabbatical is to gain a working knowledge of the state-of-the-art space and time resolved Brillouin light scattering (BLS) system developed in Professor Hillebrands's group. At CSU (not the German political party), we are upgrading our existing BLS system to obtain similar capabilities. I hope to learn as much as I can about the system here and apply that experience to new experiments on microwave magnetic excitations and devices when I return to Colorado. While in Kaiserslautern, I would also like to initiate new experiments which integrate the wavevector selectivity techniques we have developed in Colorado [1, 2] with the space and time resolved techniques developed here.

Two additional scientific objectives for my sabbatical are (1) to work with the group to develop new theoretical approaches and simple clearly defined experiments to elucidate the processes of magnetization reversal and high speed switching in magnetic thin films and small particles, and (2) to develop "A Child's Guide to Units in Electromagnetism" which can serve as a practical pedagogy for a clear understanding of units in electromagnetism in general and magnetics in particular.

References

[1] *A wave vector selective light scattering magnon spectrometer*, W.D. Wilber, W. Wettling, P. Kabos, C.E. Patton, W. Jantz, J. Appl. Phys. **55**, 2533 (1984).
[2] *Brillouin light scattering and magnon wave vector distributions for microwave magnetic envelope solitons in yttrium iron garnet thin films*, H. Xia, P. Kabos, H.Y. Zhang, P. Kolodin, C.E. Patton, Phys. Rev. Lett. **81**, 449 (1998).

Prof. Dr. Andrei Slavin

Country: USA
Visiting period: 04.07.99 to 11.07.99

I am a Professor of Physics at the Oakland University, Rochester, Michigan, USA. I am collaborating wth the group of Prof. Hillebrands for over 4 years, and this was my regular summer visit.

As always, my stay at Kaiserslautern was both interesting and stimulating.

I worked on the text of our joint paper on "Linear and Nonlinear Diffraction of Dipolar Spin Waves in Yttrium Iron Garnet Films Observed by Space- and Time-Resolved Brillouin Light Scattering (BLS)". This paper summarizes our joint research work on the diffraction of two-dimensional spin wave packets in magnetic films.

The combination of the unique experimental capabilities of the Kaiserslautern group, where a new method of BLS technique with temporal resolution was developed with theoretical expertise of the Rochester group, allowed us to observe experimentally and describe theoretically a whole range of linear and nonlinear diffraction phenomena. That includes non-reciprocal excitation of surface magnetostatic waves, anisotropic propagation of wave beams with non-collinear group and phase velocities, stationary self-focusing of spin wave beams and formation of spatial solitons, non-stationary spatio-temporal self-focusing of two-dimensional spin wave packets and formation and propagation of spin wave "bullets". We also developed a simple variational approach to the description of wave packet evolution in magnetic films.

Another aim of my short visit was to discuss a program of further collaboration that will concern the problem of two-dimensional wave front reversal of a spin wave packet interacting with the localized parametric pumping, and calculation of the spin wave spectra of magnetic dot arrays.

I really enjoyed the warm hospitality of Prof. Hillebrands' group and hope to pay another visit next year.

2.3 Group Member Photo Gallery

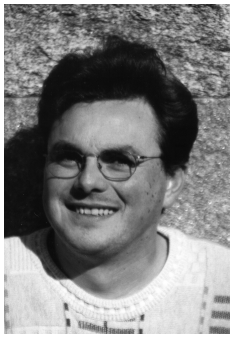

Martin Bauer
Ph.D. student

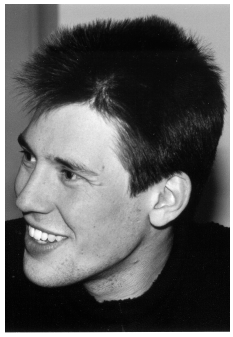

Oliver Büttner
Ph.D. student

Dr. Serguei Demokritov
Senior scientist

Dr. Jürgen Fassbender
Senior scientist

André Frank
Ph.D. student

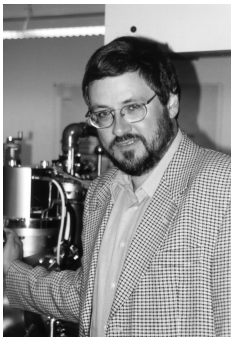

Prof. Dr. Burkard Hillebrands
Group leader

Jörg Jorzick
Ph.D. student

Dr. Kurt Jung
Senior scientist

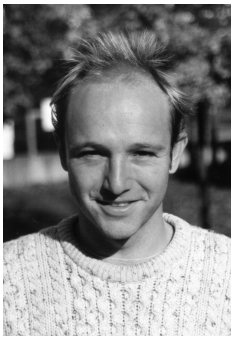

Christian Krämer
Diploma student

Radek Lopusnik
Ph.D. student

Tim Mewes
Ph.D. student

Dr. Alexandra Mougin
Postdoctorial fellow

Sibylle Müller
Secretary

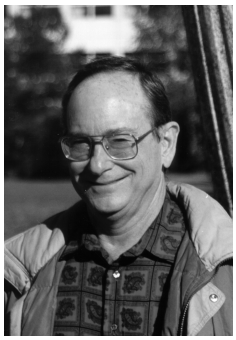

Prof. Dr. Carl Patton
Guest scientist

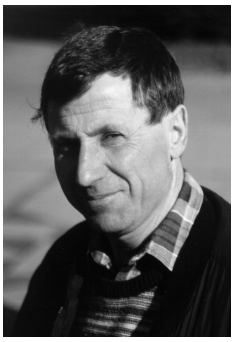

Bernd Pfaff
Technician

Stefan Poppe
Ph.D. student

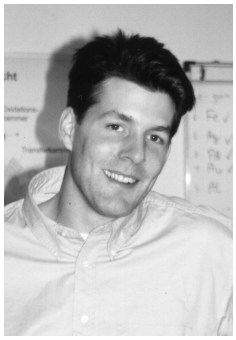

Marc Rickart
Ph.D. student

Björn Roos
Ph.D. student

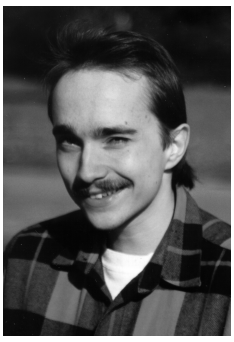

Andreas Rueff
Diploma student

Thomas Wittkowski
Ph.D. student

Chapter 3: Research Topics

We study mostly magnetic phenomena in ultrathin films and multilayers. Many activities belong to the field of magneto-electronics, a rapidly developing area bridging the gap between conventional magnetism and semiconductor physics in view of potential applications as sensor devices and magnetic random access memories. One key issue is the fabrication of high-quality epitaxial film and multilayer systems and devices using molecular beam epitaxy.

Our scientific work concentrates mostly on problems in basic research, which emerge from applications of magnetic structures in data storage and sensor devices. We investigate both material sciences aspects of magnetic films, multilayers and patterned structures, and high frequency magnetic properties like linear and nonlinear spin waves, time dependent magnetization effects, and the time structure of the magnetic switching process.

In detail, our research subjects are:

1) Investigations of growth and structure of thin magnetic epitaxial films and multilayers

To study magnetic phenomena with the necessary precision, the preparation of samples with highest possible structural quality is very important. We achieve this by using molecular beam epitaxy (MBE), in which the standard *in situ* methods for chemical and structure analysis are employed. They comprise Auger spectroscopy for chemical analysis, low and high energy electron diffraction (LEED, RHEED), and a combined *in situ* scanning tunneling and atomic force microscope (STM/AFM).

2) Anisotropies of ultrathin magnetic films and exchange bias systems

Of interest to us is the determination and the origin of all contributing magnetic anisotropies, of magnetic moments at interfaces, of coupling phenomena between magnetic films, and of the influence of atomic defects, steps, roughness and interdiffusion on the magnetic properties. An important issue is to clarify the origin of the exchange bias mechanism, a shift of the hysteresis loop along the field axis in bilayers of ferromagnetic and antiferromagnetic films.

We perform *in situ* Brillouin light scattering spectroscopy (BLS) and magneto-optic Kerr-magnetometry in the MBE system. *Ex situ*, the samples are investigated using Brillouin light scattering, vector Kerr magnetometry and vibrating sample magnetometry (VSM).

3) Tunneling magnetoresistance junctions

We investigate transport phenomena based on the magnetic tunneling effect with the aim to develop new magnetic sensors. In a dedicated project we put special emphasis on the development of new methods to improve the structural quality of the insulating tunneling layers. We also conduct a program to search for new tunneling barrier materials.

4) Modification of magnetic properties in thin films by patterning

Patterning of magnetic films allows one to generate materials with new magnetic properties, like magnetic dot or wire arrays. Such structures probably will play a dominant role in future data storage and sensor applications. We focus on the investigation of the basic mag-

netic properties of such structures. For patterning we use a UV-laser interference lithography technique. In the department we have access to electron beam lithography and photo lithography.

5) Time resolved investigations of the magnetization reversal

For memory devices it is of special importance how fast and secure magnetic domains can be written or the magnetization of single magnetic object can be reversed. These switching phenomena take place on the nanosecond time scale. A time-resolved magneto-optic Kerr effect experiment and a Brillouin light scattering experiment are used to address the time-evolution of the magnetization reversal upon the application of short magnetic field pulses.

6) Nonlinear properties of microwave excited spin waves

Using Brillouin light scattering we measure the intensities of spin waves propagating in a magnetic film with spatial resolution. The spin waves are excited by microwaves using a stripe antenna. Using a pulsed microwave source and a multi-time-gate technique, measurements are performed with time resolution. Central problems are the propagation of spin waves in the linear and nonlinear intensity regimes, the formation of instabilities (e.g. self-focusing), the propagation of nonlinear excitations (solitons, magnetic "bullets") and collision experiments of these excitations, as well as three wave processes.

7) Elastic properties of hard, super-hard and inhomogeneous films and multilayers

We prepare hard and super-hard films and investigate their elastic properties using Brillouin light scattering. Research subjects are amorphous carbon (a-C:H and ta-C:H) and boron nitride films, which are prepared using unbalanced magnetron sputtering. The elastic constants are determined from the dispersion curves of surface and film phonons (Rayleigh and Sezawa modes). Our aim is to prepare hard and super-hard films with minimized internal stresses.

Chapter 4: Equipment

A) Preparation and characterization of thin films and multilayers

1. multi-chamber molecular beam epitaxy system (Pink GmbH) comprising
   a. deposition chamber
      (electron beam and Knudsen sources, RHEED, LEED, Auger)
   b. scanning tunneling and atomic force microscopy chamber
      (*in situ* STM/AFM, Park Scientific)
   c. Brillouin light scattering and Kerr magnetometry chamber
      (magnetic field 1.2 T, temperature range 80 – 400 K)
   d. load lock chamber
   e. preparation chamber
      (optical coating, heating station 2300° C)
   f. transfer chamber
   g. atom beam oxidization chamber with *in situ* four-probe resistively measurement stage
2. two-chamber UHV deposition system
3. two-magnetron sputtering system
4. scanning tunneling and atomic force microscope (TopoMetrix)

B) Patterning of magnetic films

1. UV laser interference lithography setup
2. clean room facility with flow box, spin coater, etc.
3. reactive ion beam etching facility with *in situ* metal coater

C) Magnetic characterization

1. vibrating sample magnetometer with alternating gradient magnetometer option (magnetic field 1.6 T, room temperature)
2. vibrating sample magnetometer
   (magnetic field 5 T, temperature range 2 – 350 K)
3. vector Kerr magnetometer
   (longitudinal and transverse Kerr effect, magnetic field 1.2 T, temperature range 2 – 350 K, automated sample positioning)
4. high-field polar Kerr magnetometer
   (magnetic field 5 T, temperature range 2 – 350 K)
5. Kerr magnetometer with time resolution and setup for generation of short field pulses
6. confocal Kerr microscope (under construction)
7. magnetic force microscope with 0.1 T magnet (TopoMetrix)
8. two Brillouin light scattering spectrometers, computer controlled and fully automated (magnetic field 2.2 T) with stages for
   a. low temperature measurements (2 – 350 K)
   b. space-time resolved measurements for spin wave intensity mapping (resolution 50 µm, 0.83 ns)
   c. *in situ* measurements
   d. elastic measurements
9. microwave setup (up to 32 GHz) comprising a network analyzer, microwave amplifiers, modulators, pulse generators, etc.
10. magneto-transport setup (magnetic field 1.5 T, temperature range 20 – 400 K)

Chapter 5: Transfer of Technology

1. Magnetism

With our facilities within the Department of Physics at the University of Kaiserslautern we offer consultance and transfer of technology in the areas of thin film magnetism, magnetic film structures and devices, magnetic sensors, and in corresponding problems of metrology.

We are equipped to perform magnetic, transport, elastic and structural measurements of films and multilayer systems.

This is in detail:

- magnetometry (magnetic field up to 5 T, temperature range 2 – 400 K) using vibrating sample magnetometry, Kerr magnetometry, Brillouin light scattering spectroscopy
- magnetic anisotropies (out-of-plane and in-plane), optionally with high spatial resolution
- magneto-transport properties
- test of homogeneity of magnetic parameters
- exchange stiffness constants in magnetic films
- elastic constants
- surface topography

2. Center for Technology Transfer "Hard and wear resistant coatings" (Transfer-Stelle "Hartstoff- und Verschleißschutzschichten")

Aim of the Center for Technology Transfer is to assist companies in applications of thin film coatings to increase surfaces hardness and wear resistivity with the aim to reduce production costs and to increase product quality.

The Center is part of the University of Kaiserslautern. It is located at the TZO (Technologiezentrum für Oberflächentechnik GmbH) in Rheinbreitbach, Germany.

The following services are offered:

- Consultance in tribological problems
- Analysis of wear problems
- Development of product specific coatings
- Optimization of coatings
- Coating of samples and small scale production series
- Consultance for implementation of coating procedures into the production process
- Courses and seminars concerning coating problems

Address:

Transfer-Stelle "Hartstoff- und Verschleißschutzschichten"

Maarweg 30

53619 Rheinbreitbach, Germany

Scientific director:

Prof. Dr. B. Hillebrands	phone: +49 631 205 4228 e-mail: hilleb@physik.uni-kl.de

Contact:

Dr. K. Jung	phone: +49 631 205 2278 e-mail: jung@physik.uni-kl.de

Representatives in Rheinbreitbach:

Dr. C. Osthöver	phone: +49 2224 900 693 e-mail: idst_ost@t-online.de
Dr. S. Sattel (TZO)	phone: +49 2224 942 113 e-mail: rtzo@rz-online.de

Please contact us for more informations.

Chapter 6: Experimental Results

A. Nonlinear Spin Waves

6.1 Collision of spin wave envelope solitons with different phases

O. Büttner, M. Bauer, S.O. Demokritov, and B. Hillebrands[1]

In the physics of nonlinear wave processes the collision of solitons is frequently discussed. Recently we have studied this phenomenon by directly measuring the collision of nonlinear spin wave packets of different dimensionality in magnetic films [1]. For our experiments we used the time and space resolved Brillouin light scattering spectroscopy (BLS) technique, which allowed us to visualize for the first time directly the collision process of two counter-propagating spin wave solitons and two spin wave bullets.

It is a well known fact that solitons are stable upon head on collisions with each other. However, this does not exclude the possibility of interactions between solitons during the collision process itself. If one soliton approaches a second one, the potential energy is modified by the second soliton generating an interaction. An important parameter for the collision is the phase of the solitons. In two dimensions, where optical solitons can exist, phase changes may lead to a merging, a scattering or a spiraling of the solitons which pass each other with a fixed scattering parameter [2-5].

We have performed experiments to study the influence of the mutual phase difference between two counter-propagating, quasi-one-dimensional spin-wave envelope solitons upon their head on collision. For this purpose we used a standard microwave setup with two stripline transducers to excite two spin wave packets in a yittrium iron garnet (YIG) sample, which collide after they formed solitons. The sample has a thickness of 5 µm, a length of 25 mm and a width of 1.5 mm. The microwave radiation is produced by a network analyzer and amplified by a broadband amplifier which provides input powers of up to 750 mW, sufficient to create solitons in the sample. A fast switcher with a switching time of 2 ns is used to generate microwave pulses of a length of 20 ns to excite the wave packets. The microwave signal is split into two separate lines which are connected to the two microstrip antennas. One of these lines contains a phase shifter used to adjust the relative phase of the two colliding solitons. The scattering process is monitored using the time and space resolved BLS technique. The spatial resolution is 50 µm, limited by the size of the laser focus. The mesh size of the measurement is 0.05×0.05 mm^2, and the time resolution is below 2 ns.

Shown in Fig. 1 is the spin wave intensity in the sample integrated along the direction of the antenna as a function of the position on the sample. The five columns present the two wave packets at five subsequent moments in time, T_1...T_5, for four phase differences of the wave packets as indicated on the right hand side of the figure. The solid lines show the experimental data, and

[1] In collaboration with M.P. Kostylev, B.A. Kalinikos, St. Petersburg Electrotechnical University, Russia; Yu. Rapoport, V. Grimalsky, T. Shevchenko Kiev State University, Ukraine; Yu. Kivshar, Australian National University, Canberra, Australia; and A.N. Slavin, Oakland University, Rochester, Michigan, USA.

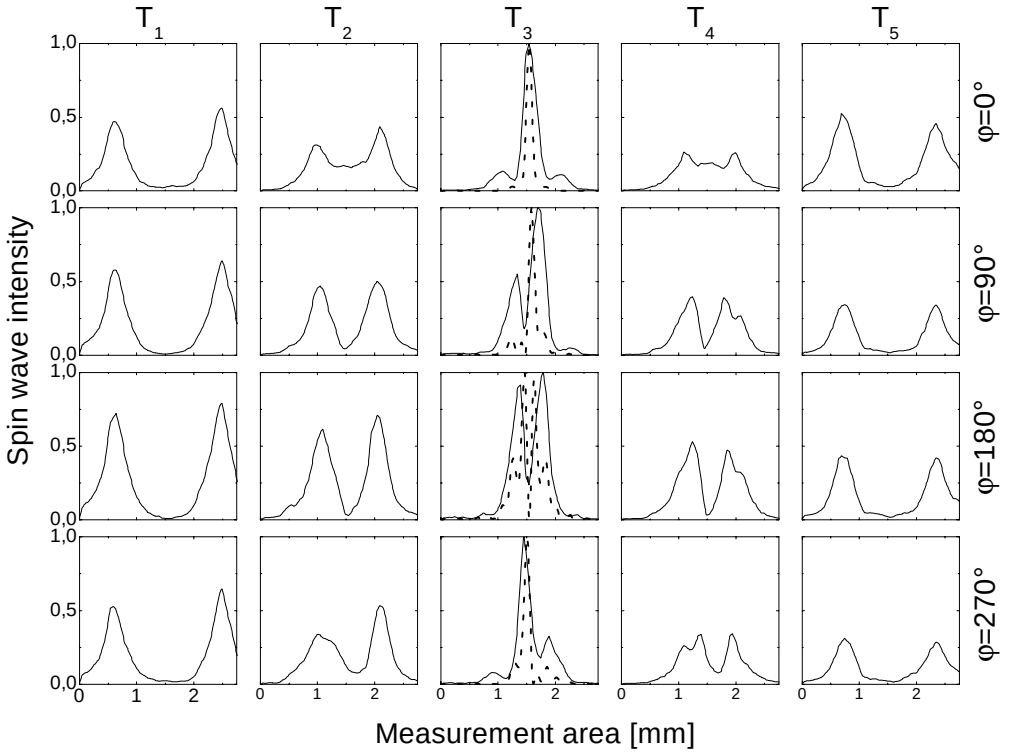

Fig. 1: Collision of two solitons as a function of their phases. The graphs show the spin wave intensity as a function of the position for five subsequent moments in time, T_1...T_5, for a phase shift of φ = 0°, 90°, 180°, and 270°. The straight lines show the results of the experiment, the dashed lines for T_3 show the result of a simulation.

the dashed lines for T_3 show the result of a simulation based on the nonlinear Schrödinger equation.

The phase has a major influence on the wave pattern during the collision, as can be seen in the graphs in the middle of the figure for T_3 where the solitons completely overlap each other. In the upper panel, for φ = 0° there is a large peak in the center with two small peaks symmetrically positioned on the left and right side of the peak. For φ = 90° the peak in the center is not present, and there appear two new peaks, with the left one smaller than the right one. A change in phase of 90° to φ = 180° phase difference leads again to a completely different picture. Now there are two peaks situated symmetrically to the left and to the right of the center peak at the positions where the minima were found for φ = 0°. Note, that comparing these minima to the asymmetrical ones for φ = 90°, there positions are slightly shifted. Finally, for φ = 270°, there are still two peaks, but now again one is smaller than the other, as was the case for φ = 90°. In contradiction to the latter case, the left one is now larger. By inspection of the cases for φ = 90° and φ = 270° we find, that the peaks do not just change their amplitude. Instead they completely disappear and new peaks are formed at different positions.

In the graphs for T_3 there is also shown a simulation of the soliton collision based on a numerical solution of the nonlinear Schrödinger equation, which is in very good agreement with the experiment.

A comparison with the collision of linear wave packets shows, that the structure is a linear interference effect between the amplitudes of the two solitons, as shown in the figure. There is no

measurable difference between linear and nonlinear collisions. It will be a subject of further studies to find out if this is just because of the parameters of this special experiment or if this is a fundamental property of spin wave envelope solitons in waveguides.

Work supported by the Deutsche Forschungsgemeinschaft.

References

[1] O. Büttner, M. Bauer, S.O. Demokritov, B. Hillebrands, M.P. Kostylev, B.A. Kalinikos, A.N. Slavin, Phys. Rev. Lett. **82**, 4320 (1999).
[2] W.E. Torruellas, Z. Wang, D.J. Hagan, E.W. Van Stryland, G.I. Stegeman, L. Torner, C.R. Menyuk, Phys. Rev. Lett. **74**, 5036 (1995).
[3] V. Tikhenenko, J. Christou, B. Luther-Davies, Phys. Rev. Lett. **76**, 2698 (1996).
[4] M. Shih, M. Sergev, G. Salamo, Phys. Rev. Lett. **78**, 2551 (1997).
[5] V.V. Stevlina, Yu.S. Kivshar, A.V. Buryak, Opt. Lett. **23**, 156 (1998).

6.2 Two-dimensional radiation patterns of magnetostatic spin waves

O. Büttner, M. Bauer, S.O. Demokritov, and B. Hillebrands[1]

For the application of ferrite films in signal processing, the radiation characteristics of the antenna exciting the spin waves in the ferrite film is of large interest. Here a wide film is studied, i.e., the film is much wider than the width of the excitation antenna. The radiation characteristics of magnetostatic backward volume waves was studied for different carrier wavevectors and lengths of the input antenna using the space resolved Brillouin light scattering spectroscopy [1,2].

The film material yttrium iron garnet (YIG) was used, and the spin waves were excited by a microstrip antenna of finite length l_a. This leads to a finite spectral width of the wavevectors of the spin waves. The direction of the wavevector relative to the in-plane external magnetic bias field is given by the angle ϕ where:

$$\phi = \arctan \frac{k_y}{k_z} \quad . \tag{1}$$

Here, the antenna is aligned along the *y*-direction and the external magnetic field is directed along the *z*-direction. k_z is the carrier wavevector. The maximum of the angle ϕ is given for $k_y = 2\pi/l_a$ where l_a is the length of the antenna:

$$\phi_m = \arctan \frac{2\pi}{l_a k_z} \quad . \tag{2}$$

Due to the fact that magnetostatic spin waves in YIG films are dispersive, the direction of the group velocity of a wave does not correspond to the direction of its carrier wavevector. The direction of the group velocity $\mathbf{v}_g$ can be calculated using the dispersion relation $\omega(\mathbf{k})$:

$$\mathbf{v}_g = \text{grad}\, \omega(\mathbf{k}) \quad . \tag{3}$$

The angle of the group velocity relative to the external magnetic field is:

$$\theta = \arctan \frac{v_y}{v_z} \quad . \tag{4}$$

The experiments described below were performed in a wide YIG film with a length of 26 mm and a width of 18 mm. The thickness of the film was 7 µm.

Figure 1 shows for three different cases the spatial intensity distribution of the excited spin waves. In the left part of each panel the angle of the group velocity as a function of the angle of the wavevector with the external magnetic field is shown, whereas the right part of each panel shows the spin wave distribution in the sample in a gray-scale code. Dark corresponds to low and light corresponds to high spin wave intensity. The black bars on the axes in the left pictures show the interval of the angle of the wavevectors and the corresponding interval of the angle of the group velocity. The black bars in the right pictures near the *y*-axis show the position of the input antenna.

[1] In collaboration with A.N. Slavin, Oakland University, Rochester, Michigan, USA.

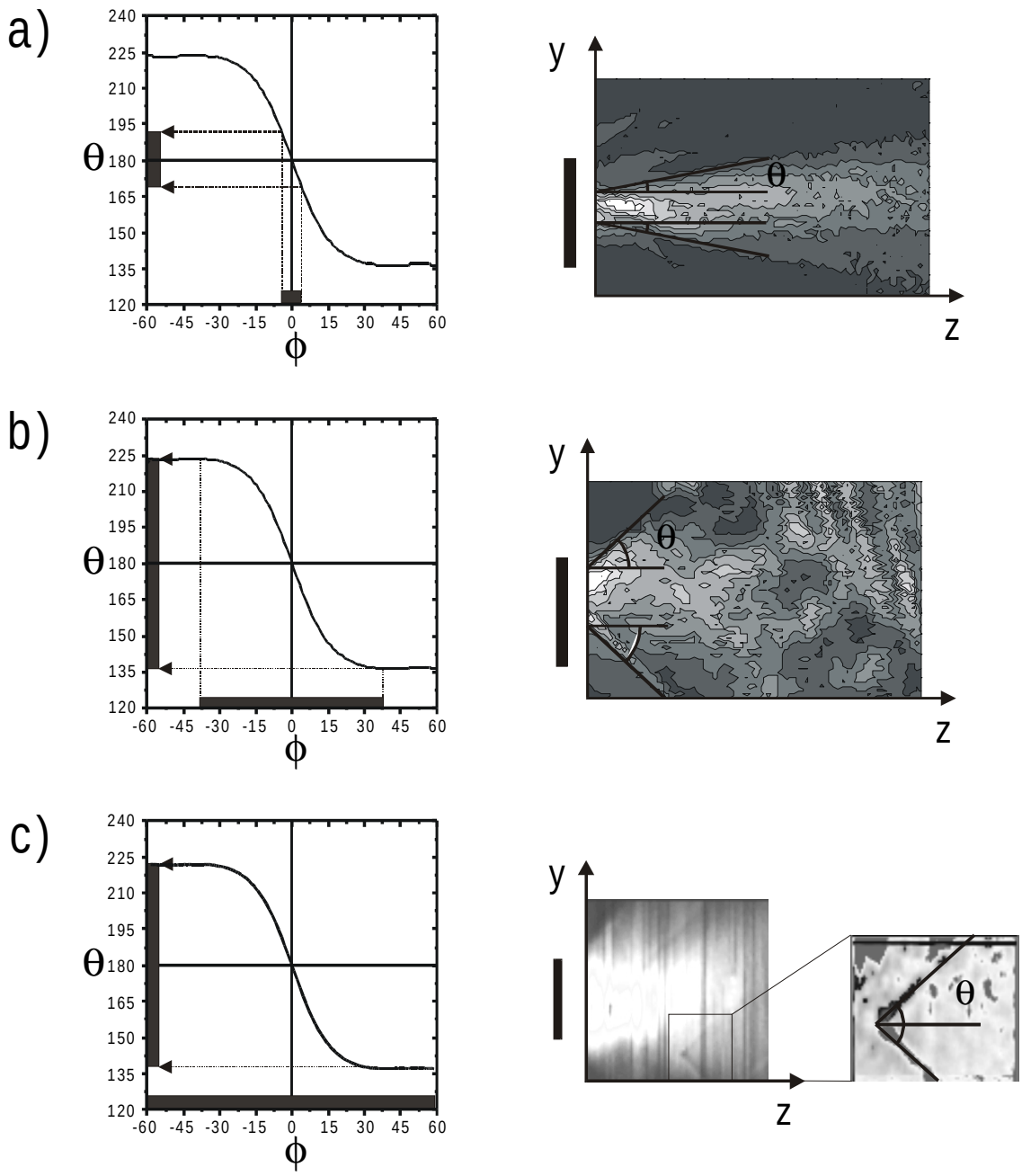

Fig. 1: Pattern of microwave excited spin waves for different carrier wavevectors and different lengths of the excitation antenna. The left part of the figure shows the function θ(ϕ). The angular interval of the wavevectors is shown on the abscissa and the angular interval of the group velocities is shown on the ordinate by the black bars. The right part of the figure shows the spin wave intensity distribution in the sample and, by the black lines, the maximum angle of the spin wave propagation shown in the left panels by the dashed arrows. The black bar near the *y*-axis shows the position of the input antenna. a) case for a long antenna and a large carrier wavevector. b) case for a long antenna and a small carrier wavevector. c) case of a point-like antenna (shown in the magnified section) and a large carrier wavevector. Parts a) and b) are corrected for damping.

Figure 1a corresponds to a large carrier wavevector and a long antenna. The external field in this case is $H = 1928$ Oe and the microwave frequency is $\nu = 7.3$ GHz which leads to a carrier wavevector of $k_z = 350$ cm^{-1}. The length of the antenna was $l_a = 2.5$ mm. With these parameters

the angle interval of the wavevector is $-4° < \phi < 4°$ and from the graph in Fig. 1a the angle interval of the group velocity is found to be $169° < \theta < 191°$. The black lines in the right part of Fig. 1a indicate the maximum angles, and obviously most of the spin waves are radiated in this angle interval.

Figure 1b corresponds to a small carrier wavevector. In this case $H = 1928$ Oe, $\nu = 7.48$ GHz and $l_a = 2.5$ mm. This leads to a carrier wavevector of $k_z = 32$ cm^{-1} and to $-36° < \phi < 36°$. The angle of the group velocity is $137° < \theta < 223°$. Again the black lines in the right part of the figure show the angular range which is in a good agreement with the experiment.

Figure 1c demonstrates another excitation pattern. The spin waves are again excited by an antenna of a length of $l_a = 2.5$ mm. The external field is $H = 2109$ Oe and the microwave input frequency is $\nu = 7.98$ GHz which results in a carrier wavevector of $k_z = 80$ cm^{-1}. From this follows $-17° < \phi < 17°$ and $147° < \theta < 213°$. The inset in Fig. 1c shows a magnification of an area of the film where a point-like defect is located. This defect acts as an antenna which has an effective length of $l_a \approx 0.1$ mm, This leads to a very wide interval of the angles of the wavevector ϕ. As it can be seen in the left panel of Fig. 1c, this interval covers the plateau of the function $\theta(\phi)$. Thus an essential part of the spin waves excited by this point-like antenna is propagating along the direction, which corresponds to $\theta = \theta_m$. For above experimental conditions $\theta_m = 42°$, which is in a very good agreement with the experimental value.

Work supported by the Deutsche Forschungsgemeinschaft.

References

[1] O. Büttner, M. Bauer, S.O. Demokritov, B. Hillebrands, Yu.S. Kivshar, V. Grimalsky, Yu. Rapoport, A.N. Slavin, submitted to Phys. Rev. B.

[2] *Space- and time-resolved Brillouin light scattering from nonlinear spinwave packets,* O. Büttner, M. Bauer, A. Rueff, S.O. Demokritov, B. Hillebrands, A.N. Slavin, M.P. Kostylev, B.A. Kalinikos, Ultrasonics, in press.

6.3 Spin wave patterns in magnetic waveguides

A. Rueff, O. Büttner, M. Bauer, S.O. Demokritov, and B. Hillebrands[1]

Narrow magnetic films (magnetic waveguides) are interesting objects for studies of spin wave propagation because of their applicability as active parts in microwave circuits. In the last years the propagation of microwave excited spin waves in these waveguides was intensively investigated using microwave techniques [1-4]. The application of the space resolved Brillouin light scattering technique allows one to study the two-dimensional distribution of spin-wave intensities and to observe such effects like the mode beating [5, 6]. In this contribution the study of the influence of the sample width and of the carrier wavevector on the spin wave intensity distribution pattern in waveguides is reported.

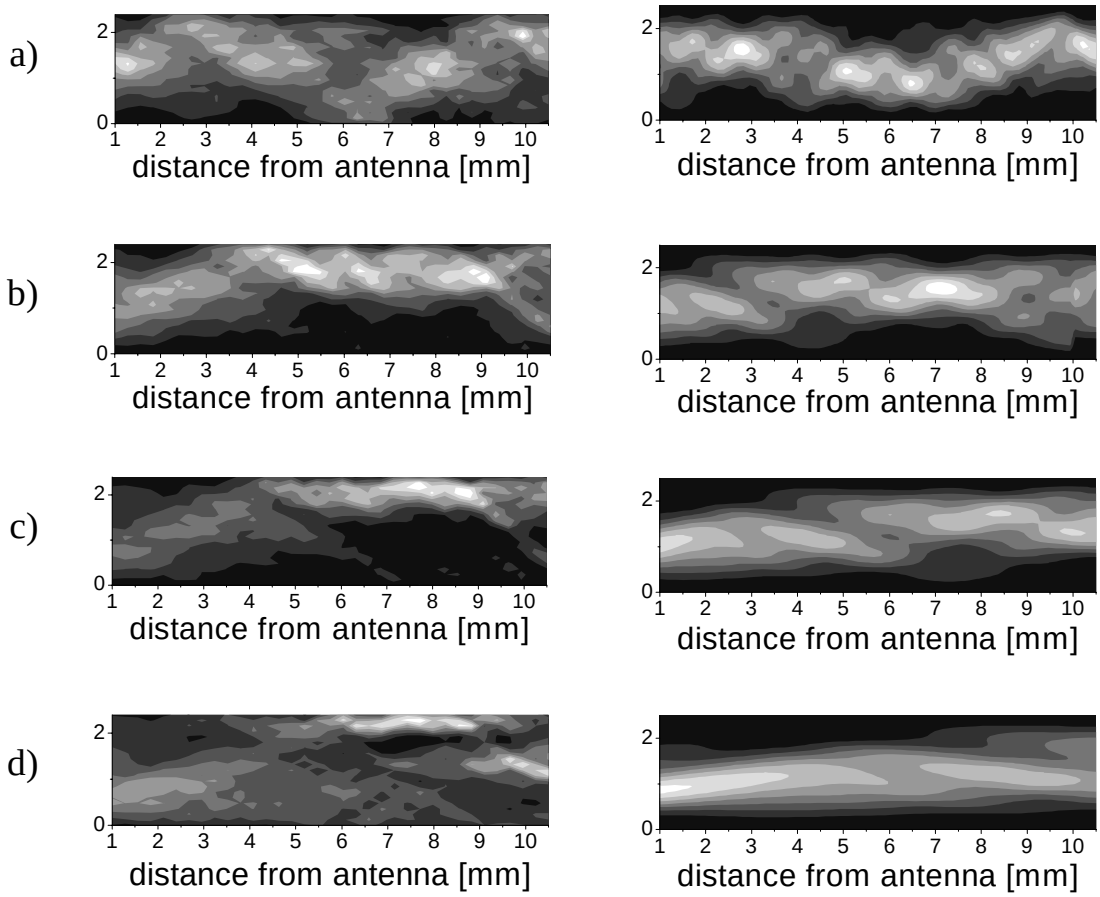

Fig. 1: Spin wave intensity distribution in a waveguide for different carrier wavevectors. The input antenna is at the left side at the position $x = 0$. The left panels show the results of the experiments and the right panels show the result of a numerical simulation based on the nonlinear Schrödinger equation. In this grayscale representation dark areas corresponds to low and bright areas to high spin wave intensities. The parameters of the experiment and of the simulation are a) $k = 46$ cm^{-1}, $S = 8.7 \cdot 10^3$ cm^2/s; b) $k = 100$ cm^{-1}, $S = 4.0 \cdot 10^3$ cm^2/s; c) $k = 150$ cm^{-1}, $S = 2.7 \cdot 10^3$ cm^2/s; d) $k = 284$ cm^{-1}, $S = 1.4 \cdot 10^3$ cm^2/s.

[1] In collaboration with A.N. Slavin, Oakland University, Rochester, USA, M.P. Kostylev and B. Kalinikos, Electrotechnical University St. Petersburg, Russia.

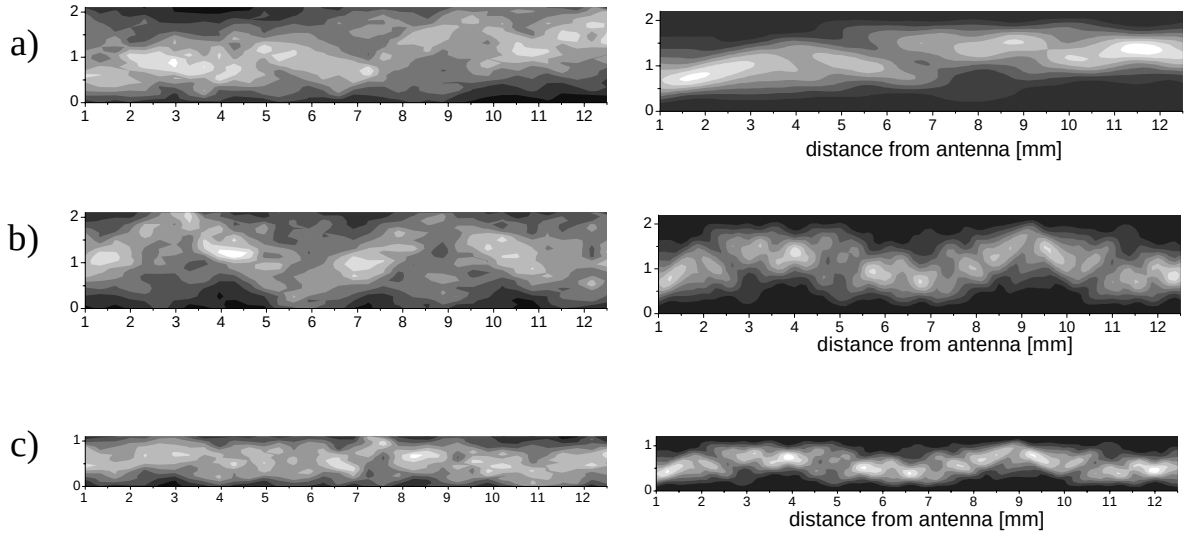

Fig. 2: Spin wave intensity distribution for different carrier wavevectors and sample sizes. The input antenna is at the left side at the position $x = 0$. The left panels shows the experimental results and the right panels show the result of a simulation based on the nonlinear Schrödinger equation. The grayscale code is the same as in Fig. 1. The parameters for the experiments and the simulation are: a) $S = 2.5 \cdot 10^3$ cm^2/s, $d = 2.2$ mm; b) $S = 8.9 \cdot 10^3$ cm^2/s, $d = 2.2$ mm; c) $S = 2.7 \cdot 10^3$ cm^2/s, $d = 1.2$ mm.

Spin waves excited in a magnetic film by an antenna are pinned at the edges of the film. The pinning leads to the formation of width modes with a profile which can be described by the function:

$$a_n(y,z,t) = a_n(z,t)\sin\left(\frac{n\pi}{d}y\right) \tag{1}$$

where z is the in-plane direction perpendicular to the antenna, y is the in-plane direction parallel to the antenna and along the width of the film, d is the width of the film and n is the order of the width mode. a_n is the amplitude of each mode. Width modes of different orders with the same frequency have slightly different carrier wavevectors and therefore different phase velocities. The latter lead to a characteristic snake like interference pattern [6], which can be numerically simulated by means of the nonlinear Schrödinger equation (NLS):

$$\frac{\partial a_n}{\partial t} + v_g \frac{\partial a_n}{\partial t} - iS\frac{\partial^2 a_n}{\partial y^2} + i\frac{T}{2}\sum_{ijm} a_i a_j^* a_m \delta\left(k_i - k_j + k_m - k_n\right) = 0 \tag{2}$$

where v_g is the group velocity, S is the diffraction parameter, T is the parameter which describes the strength of the nonlinear coupling between the modes, a_n is the amplitudes of the n-th mode and k_n is the carrier wavevector.

Figure 1 shows the influence of the carrier wavevector, which determines the value of the diffraction parameter, on the spin wave pattern in the sample. The left panels show in a grayscale code the spin wave intensity distribution measured in the experiment for a 2.5 mm wide and 25 mm long yttrium iron garnet (YIG) sample with a thickness of 5 µm. In the figure dark areas correspond to low and bright areas correspond to high spin wave intensities. The area accessible by the measurement is from a distance of 1 mm to a distance of 10.5 mm from the input antenna

in propagation direction and 2.4 mm along the width of the sample, as is indicated at the axes. The right panels show the results of the spin wave intensity simulation with the experimental parameters. The input power in the measurements was P_{in} = 10 mW, and the other parameters were a) $k = 46\ cm^{-1}$, $S = 8.7 \cdot 10^3\ cm^2/s$; b) $k = 100\ cm^{-1}$, $S = 4.0 \cdot 10^3\ cm^2/s$; c) $k = 150\ cm^{-1}$, $S = 2.7 \cdot 10^3\ cm^2/s$; d) $k = 284\ cm^{-1}$, $S = 1.4 \cdot 10^3\ cm^2/s$. The group velocity is $v_g = 5 \cdot 10^5$ cm/s. As can be seen, the main effect of the carrier wavevector and the diffraction is, that it changes the beating frequency of the interference pattern, i. e. the larger S the higher the mode beating frequency. The results of the simulation are in good agreement with the experiment.

Next the influence of the width of the sample on the spin wave pattern was investigated. By inserting the above mode profile into the NLS one obtains that the beating wavelength of the spin wave pattern should scale with the diffraction parameter divided by the square of the film width, i. e. for all experiments with the same S/d^2 value the patterns should be the same.

In Fig. 2 the results of the experiments for two different sample widths are shown. The left panels show the result of the experiment and the right panels show the result of the simulation. The input power in these experiments was P_{in} = 10 mW. Figure 2a shows the result for a carrier wavevector of $k = 160\ cm^{-1}$, which gives $S = 2.5 \cdot 10^3\ cm^2/s$, and for a sample width of d = 2.2 mm. In Fig. 2b the carrier wavevector was changed to $k = 45\ cm^{-1}$ which leads to $S = 8.9 \cdot 10^3\ cm^2/s$. This gives $S/d^2 = 1.8 \cdot 10^6\ s^{-1}$. It is obvious that the beating wavelength changes with the diffraction parameter. In Fig. 2c the carrier wavevector was chosen to be the same as in a), i. e. $k = 147\ cm^{-1}$ which gives $S = 2.7 \cdot 10^3 cm^2/s$. But the width of the sample in this experiment was chosen to be d = 1.2 mm. This gives $S/d^2 = 1.9 \cdot 10^6\ s^{-1}$ which is approximately the same value as in b). Comparing Figs. 2b and 2c it is obvious, that the mode beating frequency is the same. Again the simulations shown on the right hand side are in good agreement with the experiment. From these experiments it is clear that the spin wave patterns in the waveguides scale with the parameter S/d^2.

Work supported by the Deutsche Forschungsgemeinschaft.

References

[1] A.V. Bagada, G.A. Melkov, A.A. Serga, A.N. Slavin, Phys. Rev. Lett. **79**, 2137 (1997).
[2] P.A. Kolodin, P. Kabos, C.E. Patton, B.A. Kalinikos, N.G. Kovshikov, M.P. Kostylev, Phys. Rev. Lett. **80**, 1976 (1998).
[3] B.A. Kalinikos, N.G. Kovshikov, C.E. Patton, Phys. Rev. Lett. **80**, 4301 (1998).
[4] B.A. Kalinikos, N.G. Kovshikov, C.E. Patton, Appl. Phys. Lett. **75**, 265 (1999).
[5] M. Bauer, C. Mathieu, S.O. Demokritov, B. Hillebrands, Phys. Rev. B **56**, R8483 (1997).
[6] O. Büttner, M. Bauer, C. Mathieu, S.O. Demokritov, B. Hillebrands, P.A. Kolodin, M.P. Kostylev, S. Sure, H. Dötsch, V. Grimalsky, Yu. Rapoport, A.N. Slavin, IEEE Trans. Mag. **34**, 1381 (1998).

B. Magnetic Tunnel Junctions

6.4 Preparation of thin insulating barrier layers for tunnel magneto-resistance junctions using ionized atom beams

B.F.P. Roos, M. Rickart, S.O. Demokritov, and B. Hillebrands

The physical properties and technical applications of tunnel magneto-resistance (TMR) junctions were under intensive investigations during the last years. The major technological issue is the preparation of a thin insulating tunnel barrier layer to achieve a magneto-resistance effect of large enough strength. Two major methods have been established up to now: plasma oxidation/nitration and thermal oxidation. Results of these methods are very promising, but one of the major problems is still the rapid drop of the TMR-effect with increasing bias voltage. The bias-voltage dependence results from impurities and defects inside the barrier layer which cause spin-flip scattering of electrons and a loss of the spin polarization of the tunneling current. For thermal oxidation and plasma oxidation the pressure inside the reaction chamber is rather high. Contaminating particles are deposited on the top of the forming tunneling barrier to a non-negligible degree. During the plasma oxidation process high energetic plasma ions produce additional defects in the barrier.

To produce TMR junctions with a weak bias-voltage dependence, it is necessary to develop a method of oxidation or nitration which produces a homogeneous barrier layer with a low concentration of impurities and defects. The oxidation/nitration process must take place with high efficiency enabling a short preparation time. A low pressure inside the preparation chamber assures that the number of contaminating particles from the chamber walls can be kept low.

The method of oxidation and nitration with a collimated ionized atom beam fulfills all these demands. In this technique a highly excited oxygen or nitrogen plasma is burning in a chamber separated from the reaction chamber. Inside the plasma chamber the pressure is high enough for the gas molecules to dissociate. The ionized atoms are extracted from the plasma chamber into the reaction chamber through a small extraction hole. The configuration of the atom beam source is made in a way, that the extracted beam is collimated. The advantage of this method is

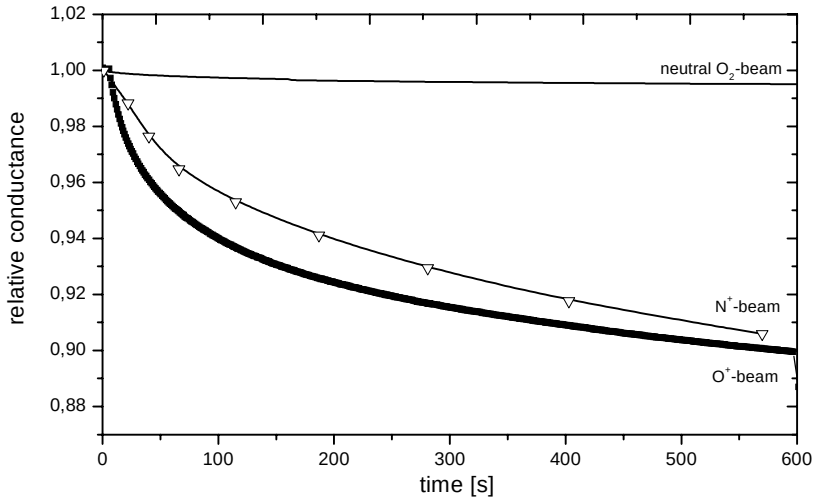

Fig. 1: Conductivity change of a 100 Å thick Al film, exposed to a) a neutral O_2-beam, b) an ionized N^+-beam, and c) an ionized O^+-beam, the latter two with an energy of 40 eV. The neutral molecule beam has little effect on the Al film. The ionized atom beams (O^+ and N^+) change the conductivity rapidly until it reaches saturation.

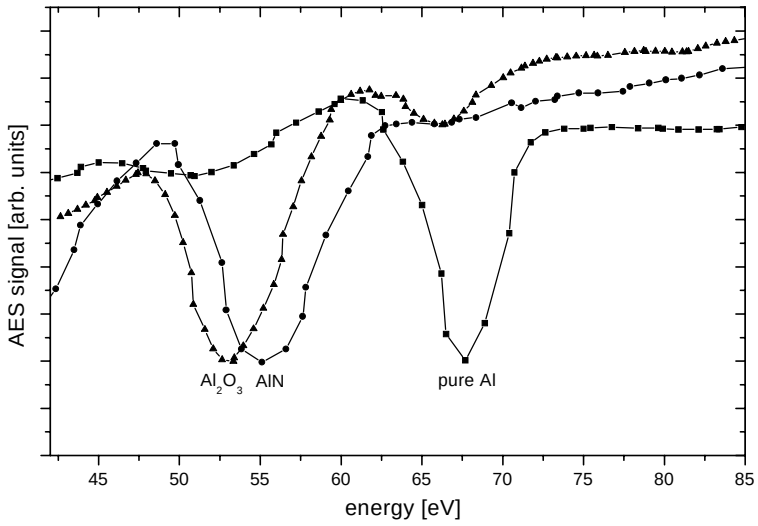

Fig. 2: Auger electron spectroscopy (AES) measurements on pure Al, AlN and Al_2O_3. A chemical shift of the low energy Al-peak is observed. Using AES it is possible to distinguish between pure Al and oxidized/nitrated Al at the barrier interface.

that impurities from the chamber walls are kept inside the plasma chamber. The pressure inside the reaction chamber with the sample is much lower.

The dissociation degree of the ion beam is more than 80%, therefore we call it an atom beam. The reactivity of the beam is rather high for both oxygen and nitrogen gases. To analyze the reactivity of the atom beam, we measured the conductivity of a 100 Å thick Al layer, deposited with MBE onto a thermally oxidized SiO_2 substrate, with an *in situ* four-point measurement stage which is integrated into the reaction chamber. Figure 1 shows the change in time of the conductivity while the Al-layer was exposed to a ionized oxygen or nitrogen beam. To emphasize the high reactivity of the O^+ and N^+-beams with the Al film, the conductivity change of the Al film exposed to a neutral O_2 beam is also displayed. Pressure and flow rates for the neutral and the ionized beams were the same in all these experiments. It is obvious that the reactivity of the ionized atom beam is many times larger then of the neutral O_2 beam.

Auger electron spectroscopy (AES) allows us to analyze the chemical composition of the obtained barriers. For the low energetic Al-peak a chemical shift of several eV occurs depending on the chemical environment of the Al atom. Figure 2 shows three AES spectra taken from pure Al, AlN and from a very shortly oxidized Al_2O_3 sample, respectively. The pure Al peak occurs at an energy of 64 eV. After 120 s in an atomic nitrogen beam the Al peak is shifted to 55 eV, due to the changed chemical environment for Al in AlN, whereas no pure Al peak is observed. That indicates a complete nitration of the first few monolayers of the Al film. A similar picture is observed on the completely oxidized Al layer.

A different situation indicates the spectrum of the shortly (few seconds) oxidized Al-layer. A large peak at 52 eV, indicating Al_2O_3, is clearly seen and the pure Al peak can be still observed. Thus, if the oxidation time is too short for the top Al atomic layers to be completely oxidized, well defined domains of Al_2O_3 and pure Al are coexisting.

The first experiments with ionized atomic beam oxidation/nitration show that the method is suitable to prepare thin Al_2O_3 and AlN barrier layers. The oxidation times are very short compared to standard oxidation/nitration methods. The properties of TMR junctions are described in the following Sect. 6.5.

Work supported by the Deutsche Forschungsgemeinschaft.

6.5 Properties of magnetic tunneling junctions prepared by atom beam oxidation

B.F.P. Roos, S.O. Demokritov, and B. Hillebrands

Research on magneto-resistance materials has been particularly active in recent years. The large magneto-resistance effect of tunneling magneto-resistance junctions (TMR junctions) attracted enormous interest for applications like magnetic random access memory devices (MRAMs) or recording heads. The key issue is a pinhole free preparation of a thin insulating barrier layer between two ferromagnetic electrodes. We prepared several TMR junctions in a multi-chamber MBE system with a base pressure less than $5 \cdot 10^{-10}$ mbar using an contact mask system to realize direct pattering during deposition. The outline of the junction is shown in Fig. 1. The electrodes, which are a 150 Å thick Co film and a 150 Å thick $Ni_{81}Fe_{19}$ (Py) film, as well as the 20 Å thick Al-layer used to fabricate the barrier layer were deposited onto Si/SiO_2 substrates at 290 K using an electron beam evaporator. To form the insulating tunnel barrier layer the samples were transferred into a separate oxidation chamber without breaking the vacuum. The oxidation process of the Al layer was performed with an ionized and collimated atom beam (see previous Sect. 6.4). The junction area is 0.25 mm^2.

Figure 2 shows magnetic hysteresis loops of the individual electrodes (insets) and the complete junction measured using a magneto-optical Kerr effect (MOKE) magnetometer at room temperature. A necessary condition for the observation of the TMR effect is the possibility to switch the magnetization of the two electrodes between the parallel and antiparallel configuration. Because of the different coercivity fields for the Co and the Py layer, an antiparallel magnetic configuration of the electrodes is obtained and the reversal of the magnetization takes place over a few Oe. A similar behavior is observed for the magneto-resistance (MR) curves shown below in Fig. 3.

The MR curves were measured using a four point probe method at various temperatures and bias voltages. Figure 3 show the MR curves of a TMR junction with a resistance of 7.5 kΩ at a bias voltage of 25 mV. The maximum TMR effect is about 10% at room temperature. At low temperatures (35K) the coercivity of the Co electrode increases largely, and the antiparallel configuration is observed over a larger region. The TMR effect increases to more than 20 %.

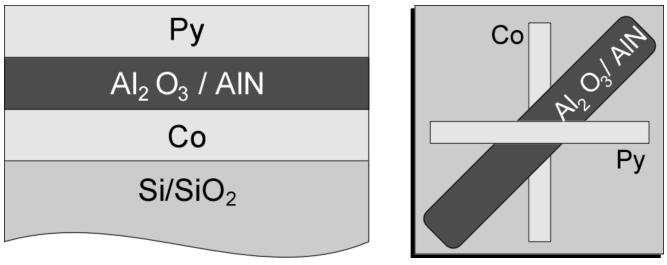

Fig. 1 : Schematic view of a patterned TMR junction. The layer thickness of Co and Py is 150 Å each. The barrier layer varies from 20 to 40 Å.

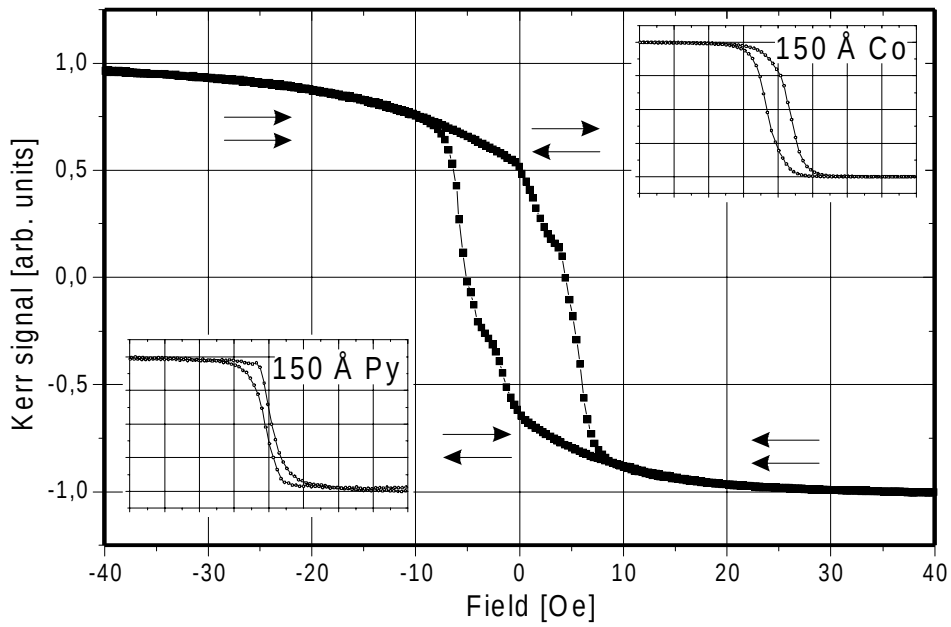

Fig. 2: Magnetic hysteresis loops of the ferromagnetic electrodes (insets, same field range as main figure) and the complete junction measured by MOKE at 290 K.

Depending on the barrier oxidation time the resistance increases exponentially. The samples shown in Fig. 4 were oxidized for 30 s to 120 s. For an oxidation time longer than 60 s, the maximum value of the TMR effect is obtained almost independent of the sample resistance. For a shorter oxidation time the TMR effect drops rapidly. This effect is caused by an incomplete oxidation of the Al layer and the increased number of spin-flip processes.

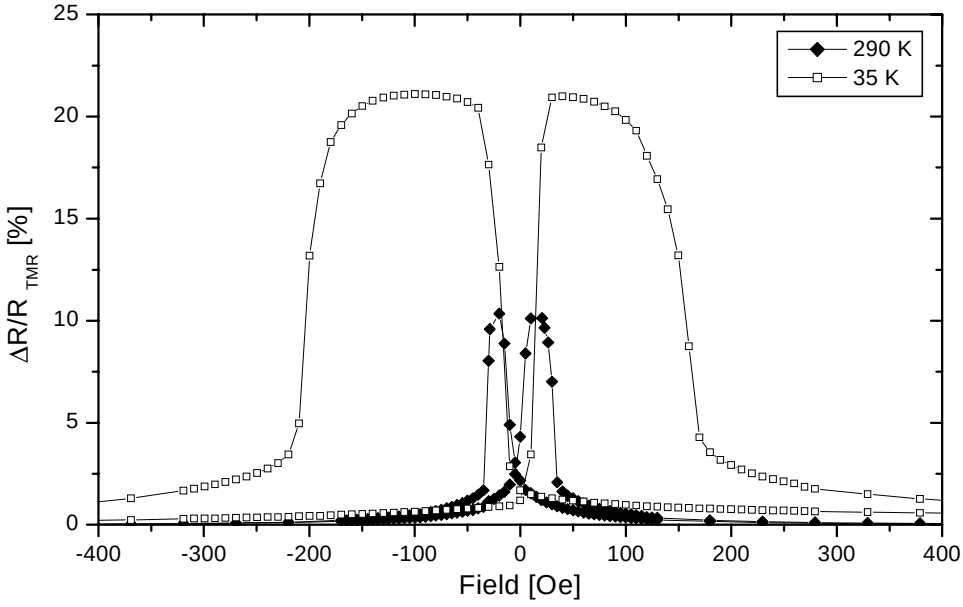

Fig. 3: Magneto-resistance of a TMR junction with a 20 Å thick Al_2O_3 barrier measured at 290 K and at 35 K with a bias voltage of 25 mV. The junction area is 0.25 mm^2.

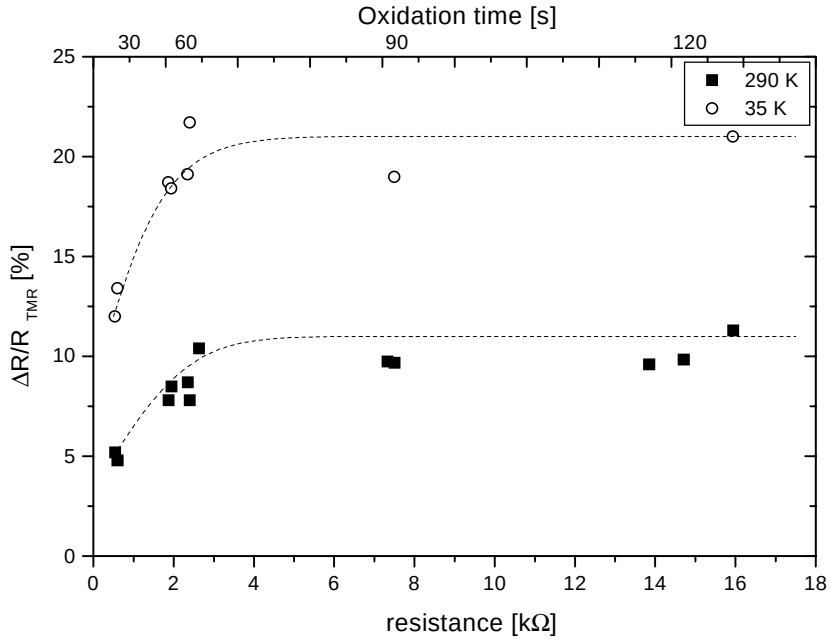

Fig. 4: TMR effect for different junction resistivities. The resistivity can be controlled by the oxidation time, which varies from 30 s to 120 s.

Work supported by the Deutsche Forschungsgemeinschaft.

C. Dynamic Magnetic Phenomena

6.6 Brillouin light scattering from quantized spin waves in micron-size magnetic wires

J. Jorzick, S.O. Demokritov, C. Mathieu, A.N. Slavin, and B. Hillebrands[1]

Recently we have reported the first observation of spin wave quantization in magnetic wires [1]. Here we present a detailed experimental investigation and the development of an appropriate theoretical description of this effect in arrays of magnetic wires of different thicknesses.

The samples were made of 20, 30 and 40 nm thick permalloy ($Ni_{80}Fe_{20}$) films deposited onto Si(111) substrates in UHV by means of e-beam evaporation. Patterning was performed using X-ray lithography and ion beam etching as described in [2]. The samples are arranged in a periodic array with a wire width of w = 1.8 µm and a wire separation of 0.7 µm and 2.2 µm. The length of the wires is 500 µm.

The spin wave properties were tested by Brillouin light scattering (BLS) using a computer controlled tandem Fabry-Pérot interferometer in backscattering geometry. An external field of 500 Oe was applied along the wires. The in-plane wavevector $q_{||}$ of the spin waves tested in the experiment was aligned perpendicular to the field, and it was varied by changing the angle of light incidence.

Figure 1 shows a typical BLS spectrum for a wavevector of $q_{||} = 0.3 \cdot 10^5$ cm^{-1} for the sample with a wire thickness of d = 40 nm, a wire width of w = 1.8 µm and a wire separation of 0.7 µm. Near 7.8, 9.3, 10.4 and 14 GHz four distinct magnetic excitations modes are observed. The mode at 14 GHz is identified as the exchange dominated perpendicular standing spin wave mode

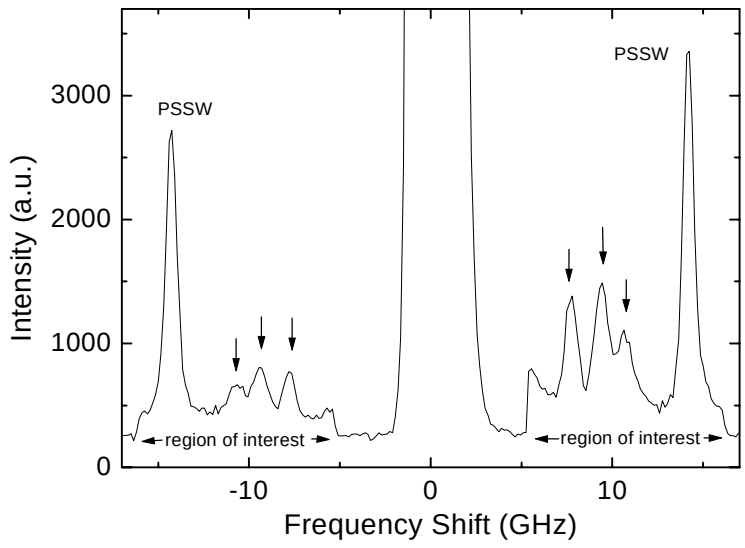

Fig. 1: BLS spectrum of the sample with a thickness of 40 nm, a wire width of 1.8 µm and a wire separation of 0.7 µm obtained for a transferred wavevector of $q_{||} = 0.3 \cdot 10^5$ cm^{-1}. A magnetic field of 500 Oe was applied along the wire axis. Several discrete modes are observed, the mode at 14 GHz is identified as the exchange dominated spinwave mode. In the region of interest (5-17 GHz) the scanning speed was reduced by a factor of three increasing the accumulation time by this factor. PSSW: Perpendicular standing spin wave.

[1] In collaboration with B. Bartenlian, and C. Chappert, IEF, Université Paris Sud, 91405 Orsay, and D. Decanini, F. Rousseaux, and E. Cambril, L2M, Bagneux, France.

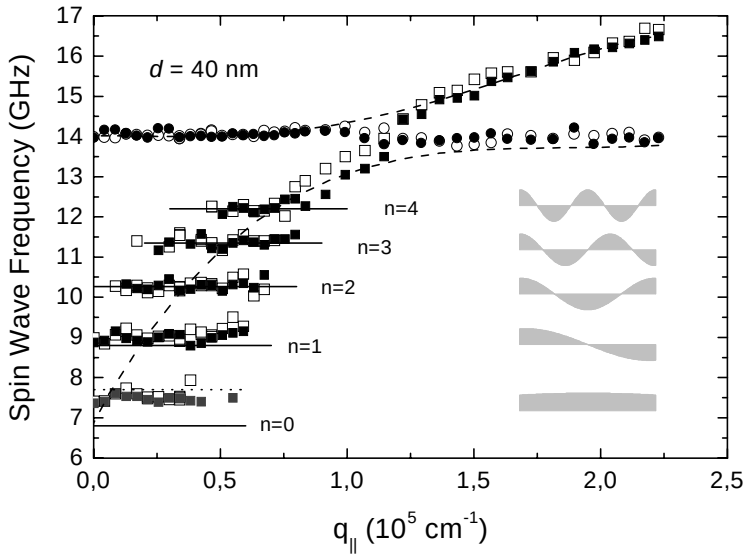

Fig. 2: Dispersion curves for the arrays of wires with a thickness of 40 nm, a wire width of 1.8 µm and different separations of the wires (0.7 µm: open symbols and 2.2 µm: full symbols). The external field applied along the wire axis was 500 Oe. The solid horizontal lines indicate the results of the calculation using Eq. (3) with the quantized values of $q_{\parallel}$. The dotted horizontal line indicates the result of the calculation for $n = 0$ taking account of the finite size effects. The dashed line shows a numerical simulation for a continuous film of the same thickness. On the right hand side the mode profiles are illustrated.

(PSSW), since it appears in the continuous film as well, and since it has a characteristic thickness dependence of $\omega \propto d^{-2}$. By varying the angle of light incidence the magnitude of $q_{\parallel}$ was varied, and the dispersion was obtained as shown in Fig. 2 for the sample with a wire thickness of 40 nm. Open symbols in Fig. 2 indicate arrays with a wire separation of 0.7 µm and full symbols those with 2.2 µm. Inspecting the experimentally observed data one notes the following: (i) For the wavevector interval of $q_{\parallel} = 0 - 0.8 \cdot 10^5$ cm^{-1} the discrete modes show no noticeable dispersion, behaving like standing wave resonances. (ii) Each mode is observed over a continuous range of the transferred wavevector, $q_{\parallel}$. (iii) The lowest modes appear very close to zero wavevector, the higher modes appear at higher values. (iv) The frequency splitting between two neighbored modes decreases with increasing mode number. (v) There is a transition regime ($q_{\parallel} \cong 0.8 - 1.0 \cdot 10^5$ cm^{-1}) where the well resolved dispersionless modes converge towards the dispersion of the continuous film. A numerical simulation for a continuous film of the same thickness is shown as a dashed line in Fig. 2 for reference. (vi) There is no noticeable difference for the data of the samples with the same wire width $w = 1.8$ µm but different wire separations (0.7 µm and 2.2 µm), which indicates that the observed modes are purely caused by the finite width of the wires and no mode coupling exists, and that each wire acts as an independent scatterer for inelastic light.

To describe the obtained results the frequencies of the modes as well as the wavevector interval over which each mode is observed were calculated. For the calculation a Cartesian coordinate system with the *x*-axis perpendicular to the film, the *y*-axis perpendicular to the wires, and the *z*-axis along the wires, which is also the direction of the external applied field, is assumed. The quantized modes are considered to result from a width dependent quantization of the in-plane wavevector of the Damon-Eshbach mode in a single wire. The quantization condition in this case can be written as:

$$q_{\parallel,n} = \frac{n\pi}{w} \quad . \tag{1}$$

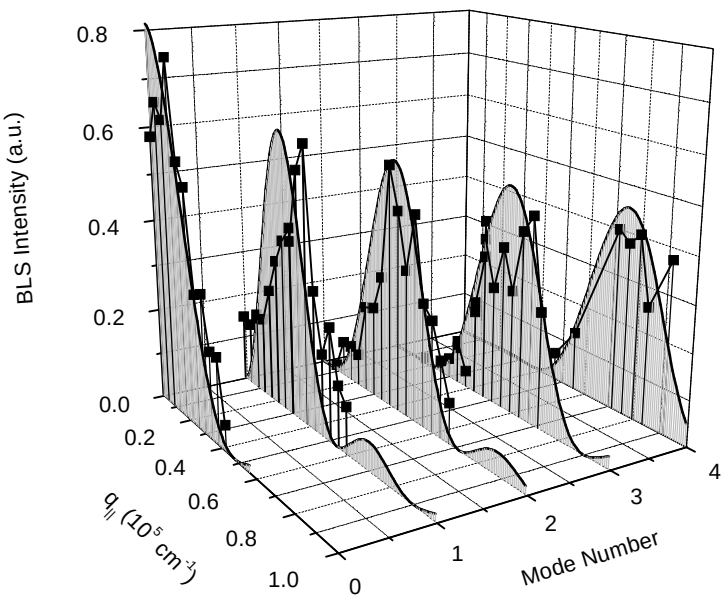

Fig. 3: Measured BLS intensity (full symbols) of the in-plane quantized spin wave modes as a function of the wavevector $q_{\parallel}$ and the mode number n in comparison with the calculated intensities (gray shaded curves).

The calculated mode profiles of the dynamic part of the magnetization are shown in Fig. 2 on the right hand side, and they can be written for the n-th mode as follows:

$$\vec{m}_{\mathrm{n}}(y) = \vec{a}_{\mathrm{n}} \cdot \cos\left(q_{\parallel,\mathrm{n}} \left(y + \frac{w}{2} \right) \right), \; -\frac{w}{2} < y < \frac{w}{2} \quad . \tag{2}$$

This equation describes a standing mode, consisting of two counter propagating waves with quantized wavevectors $q_{\parallel,\mathrm{n}}$. In order to obtain the frequencies of the lateral standing modes with the quantized wavevector $q_{\parallel,\mathrm{n}}$, the values of $q_{\parallel,\mathrm{n}}$ obtained from Eq. (1) are inserted into the dispersion equation of the Damon-Eshbach mode:

$$\nu_{\mathrm{DE}} = \frac{\gamma}{2\pi}\left[H \cdot \left(H + 4\pi M_{\mathrm{s}} \right) + \left(2\pi M_{\mathrm{s}} \right)^2 \cdot \left(1 - e^{-2 q_{\parallel,\mathrm{n}} d} \right) \right]^{1/2} \quad . \tag{3}$$

The results of the calculation are presented in Fig. 2 as solid lines. It is clear from Fig. 2 that Eq. (3) describes the experimentally measured frequencies very good for all modes except for the lowest mode with $n = 0$. The discrepancy is due to the fact that the above approach does not take into account magnetic dipolar fields caused by the finite size of the wires. Since the mode with $n = 0$ has nearly a uniform mode profile (see Fig. 2), the dynamic fields outside the wires are largest for this mode.

A calculation based on the Kittel formula taking this finite size effect into account reproduces the frequency of the mode with $n = 0$ very well (see the dotted line in Fig. 2). Since the group velocity $V_g = \partial\omega / \partial q$ of the dipolar surface spin wave mode (cf. Eq. 3) decreases with increasing wavevector, the frequency splitting between neighboring modes, which are equally spaced in q-space, becomes smaller with increasing wavevector $q_{\parallel,\mathrm{n}}$, until the splitting is smaller than the frequency resolution in the BLS experiment or the line width of the modes.

In order to calculate the wavevector interval over which each mode is observed, a closer look to the scattering process must be taken. The wavevector conservation law in the light scattering process is only valid for a plane wave traveling in an infinite medium. For a restricted geometry

the light scattering intensity is determined by the Fourier component of the dynamic part of the magnetization $m(y)$:

$$m(q_{||}) = \int_{-w/2}^{w/2} m(y) \cdot e^{iq_{||}y} dy \qquad (4)$$

which can be calculated using Eqs. (1), (2), and (4). The resulting cross section profiles $I \propto |m_n(q_{||})|^2$ of the five lowest modes for the arrays with a wire thickness of 40 nm are shown in Fig. 3. There is a very good agreement between the experimental data and the results of the calculation.

A full report is published in [3].

Work supported by the Deutsche Forschungsgemeinschaft.

References

[1] C. Mathieu, J. Jorzick, A. Frank, S.O. Demokritov, B. Hillebrands, B. Bartenlian, C. Chappert, D. Decanini, F. Rousseaux, E. Cambril, Phys. Rev. Lett. **81**, 3968 (1998).

[2] F. Rousseaux, D. Decanini, F. Carcenac, E. Cambril, M.F. Ravet, C. Chappert, N. Bardou, B. Bartenlian, P. Veillet, J. Vac. Sci. Technol. B **13**, 2787 (1995).

[3] J. Jorzick, S.O. Demokritov, C. Mathieu, B. Bartenlian, C. Chappert, F. Rousseaux, A.N. Slavin, B. Hillebrands, Phys. Rev. B **60** (1999), in press.

6.7 Spin wave quantization and dynamic coupling in arrays of micron-size magnetic circular discs

J. Jorzick, S.O. Demokritov, and B. Hillebrands[1]

Patterned magnetic films are attracting interest due to their potential applications as data storage media, in magnetic sensors and in high speed, high-density nonvolatile magnetic random access memories [1, 2]. Progress made in the last decade in lithographic techniques and the analysis of matter made it possible to fabricate well defined, laterally well controlled magnetic structures down to the nanometer size scale. Scaling the size down to the micron and nanometer size is not trivial, because for low-dimensional magnetic structures the demagnetization fields play an important part and the dynamic properties change dramatically; dynamic coupling between the magnetic islands is also possible. Recently we reported on the spin wave quantization in micron size magnetic wires [3] (see also the previous contribution). Subject of this work is the investigation of the dynamic excitations in in-plane magnetized, micron size circular magnetic dots arranged in a square array. We have observed spin wave quantization of the dipolar surface spin wave mode (Damon-Eshbach mode) due to the finite size of the dots. For the samples with an inter-dot distance of 0.1 µm an essential dipolar coupling is found.

The samples were made of permalloy ($Ni_{80}Fe_{20}$) films grown by means of e-beam evaporation in an UHV-evaporation system onto chemically cleaned Si(111). The films were covered by Pd to prevent oxidation. Before being patterned the films were tested by static magneto-optic Kerr effect (MOKE) magnetometry. A low in-plane anisotropy (<5 Oe) and coercivity (<2 Oe) was observed. Patterning was performed by x-ray lithography using a negative resist with Al coating and ion milling. Samples with different dot thicknesses d = 10, 20 and 40 nm, different dot diameters D = 1, 2 µm as well as different inter-dot separations of δ = 0.1, 0.2, 1 and 2 µm were prepared. The overall dimensions are 800×800 µm^2.

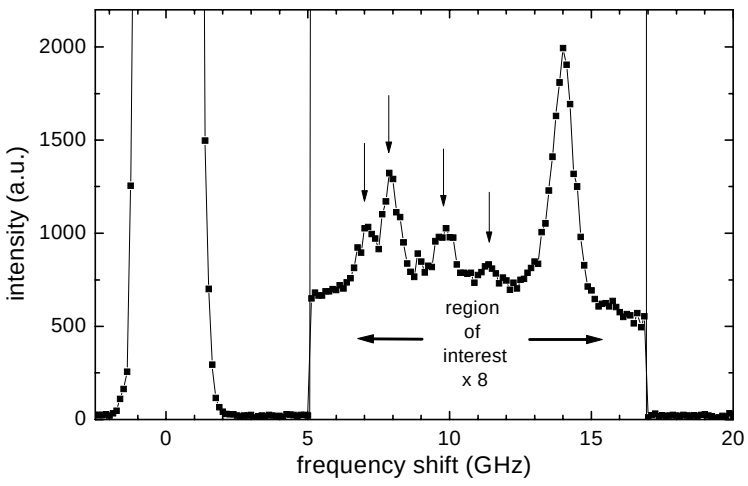

Fig. 1: Typical BLS spectrum for a sample with a dot diameter of 2µm, a thickness of 40 nm and a dot separation of 0.2 µm for a transferred wavevector $q_{\|}$ = 0.21 ·10^5 cm^{-1} and an external field of 600 Oe applied in-plane, demonstrating the existence of several discrete modes indicated by arrows. The peak at 14 GHz corresponds to the perpendicular exchange dominated standing wave. In the region of interest the scanning speed was reduced by a factor of eight, increasing the accumulation time by this factor.

[1] In collaboration with B. Bartenlian, and C. Chappert, IEF, Université Paris Sud, 91405 Orsay, and D. Decanini, F. Rousseaux, and E. Cambril, L2M, Bagneux, France.

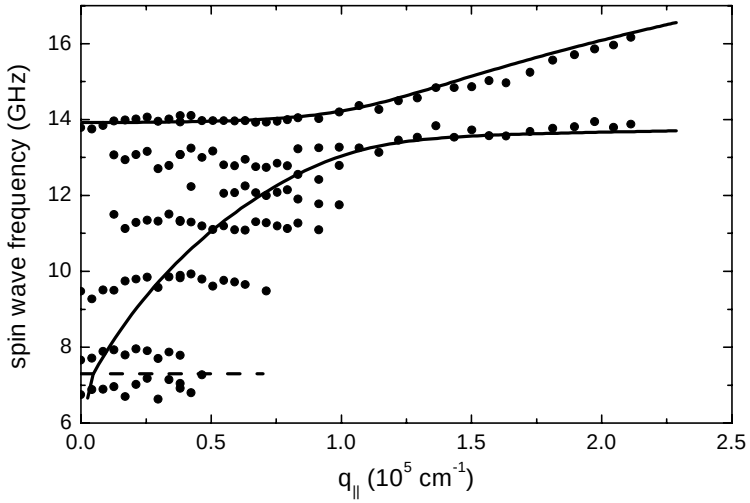

Fig. 2: Obtained spin wave dispersion curve for the sample with a thickness of 40 nm, a dot diameter of 2µm and a dot separation of 0.2 µm. An external field of 600 Oe was applied in-plane along the array lattice. The solid lines show a numerical simulation for a continuous film of the same thickness for reference. The frequency of the uniform mode of a single dot is shown as a horizontal dashed line.

The dynamic properties of the dot arrays were investigated by means of Brillouin light scattering (BLS) in the backscattering geometry. Figure 1 shows the anti-Stokes side of a typical BLS spectrum for the sample with a dot diameter D = 2 µm, a dot thickness of d = 40 nm, and with a dot separation of δ = 0.2 µm for a transferred wavevector of $q_{\|} = 0.21 \cdot 10^5$ cm^{-1} and an external field of 600 Oe applied in the plane of the dots. Near 7.0, 7.9, 9.8, 11.4 and 14 GHz several discrete magnetic excitation modes are clearly observed. The mode at 14 GHz is identified as the exchange dominated, perpendicular standing spin wave mode due to its characteristic thickness dependence $\omega \propto d^{-2}$ and due to the fact, that it also appears in the continuous film. By changing the angle θ of the incident light, the value of the transferred wavevector was varied and the dispersion was obtained as shown in Fig. 2 for the sample with a dot thickness of d = 40 nm, a dot diameter of D = 2µm and a dot separation of δ = 0.2 µm. Several discrete, dispersionless modes are observed over a continuous range of the transferred wavevector, converging for large wavevectors towards the dispersion of a continuous film, which is shown in Fig. 2 as a solid line. The frequency of the uniform mode in a single dot (ω = 7.35 GHz) is also shown in Fig. 2 as a horizontal dashed line, demonstrating the existence of modes above and below this value.

Figure 3 shows the measured dispersions for a sample with a dot thickness of 40 nm, a dot diameter of D = 1 µm and inter-dot distances δ = 0.1 and 1 µm. From comparison of Figs. 2 and 3, it is seen that the wavevector interval where each mode is observed scales approximately with D^{-1} as predicted for the wires, where the wavevector interval from a given spin wave mode confined in a magnetic island is given by the Fourier transform of the mode profile over the island [3]. Having a closer look at Fig. 3 a dependence of the frequencies of the two lowest modes on the dot separation is clearly observed, whereas the frequencies of the higher modes are almost independent of the dot separation. This experimental result is evidence for a dynamic magnetic dipolar interaction between the dots, and it can be understood as follows: The lowest two modes have frequencies near the frequency of the uniform mode and thus also a nearly uniform mode profile for the dynamic part of the magnetization – as it was also shown for magnetic wires [3]. Modes with a nearly uniform mode profile exhibit a stronger dipolar stray field compared to higher order modes with a more nodal mode profile. Therefore, if dynamic dipolar coupling exists, it will exhibit strongest effects for the lowest modes in agreement with the results found in Fig. 3.

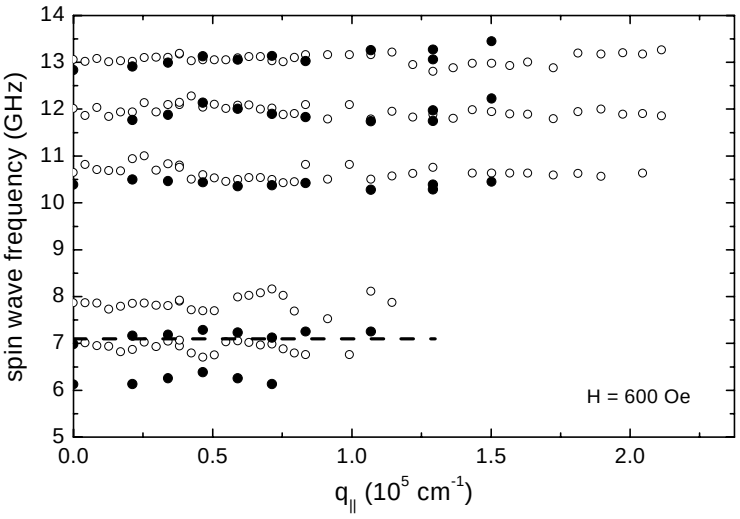

Fig. 3: Dispersion curves for the five lowest modes measured for the samples with a dot diameter of 1 µm and different inter-dot distances ($\delta = 0.1$ µm open symbols, $\delta = 1$ µm full symbols) demonstrating an essential dynamic dipolar coupling for the lowest two modes. The horizontal dashed line indicates the calculated frequency of the uniform mode in a single island.

The experimental findings lead us to the conclusion that the observed dispersionless, resonance-like modes are dipolar surface spin waves quantized due to the lateral confinement in a single magnetic disc. Unfortunately the eigen-functions of the quantized modes are not known likely due to the low symmetry of the problem. Walker considered in his pioneering work [4] an axially magnetized spheroid, where an analytical solution exists, due to the axial symmetry. This is no longer the case for the in-plane magnetized magnetic dots studied here and so the eigenmodes of these magnetic islands are not known.

A full report is published in [5].

Work supported by the Deutsche Forschungsgemeinschaft, the BMBF (Leitprojekt Magnetoelektronik) and the TMR network “Dynaspin”.

References

[1] W.J. Gallagher, S.S.P. Parkin, Y.Lu, X.P. Bian, A. Marley, K.P. Roche, R.A. Altman, S.A. Rishton, C. Jahnes, T.M. Shaw, G. Xiao, J. Appl. Phys. **81**, 3741 (1997).

[2] S.S.P. Parkin, K.P. Roche, M.G. Samant, P.M. Rice, R.B. Beyers, R.E. Scheuerlein, E.J. O’Sullivan, S.L. Brown, J. Bucchigano, D.W. Abraham, Yu Lu, M. Rooks, P.L. Trouilloud, R.A. Wanner, W.J. Gallagher, J. Appl. Phys. **85**, 5828 (1999).

[3] C. Mathieu, J. Jorzick, A. Frank, S.O. Demokritov, B. Hillebrands, B. Bartenlian, C. Chappert, D. Decanini, F. Rousseaux, E. Cambril, Phys. Rev. Lett. **81**, 3968 (1998).

[4] L.R. Walker, Phys. Rev. **105**, 390 (1957).

[5] J. Jorzick, S.O. Demokritov, B. Hillebrands, B. Bartenlian, C. Chappert, D. Decanini, F. Rousseaux, E. Cambril, Appl. Phys. Lett. **75** (1999), in press.

6.8 Static and dynamic properties of arrays of micron-size magnetic rectangular dots

J. Jorzick, C. Krämer, D. Kholin, S.O. Demokritov, and B. Hillebrands[1]

Recently we have reported the quantization of spin waves and static and dynamic magnetic dipolar coupling in arrays of micron size-magnetic wires and circular dots (see preceding Sects. 6.6 and 6.7) [1-3]. The theoretical interpretation of the quantized spin waves in in-plane magnetized circular dots is, however, not trivial. In this contribution we present an experimental spin wave study of micron size rectangular magnetic dots. The results pose a more straightforward to solve theoretical problem.

Permalloy films were prepared onto chemically cleaned Si (1 1 1) substrates by means of e-beam evaporation in a UHV system. The quality of the grown films was tested by means of magneto-optical Kerr effect (MOKE) magnetometry. A small in-plane anisotropy (<5 Oe) and a low coercivity (<2 Oe) were found. Patterning was performed by means of e-beam lithography. The rectangular dots have a thickness of 35 nm, and the lateral dimensions of the three investigated samples are 1×1 μm^2, 1×1.2 μm^2, and 1×1.75 μm^2. They were arranged in an array with the overall dimensions of 800×800 μm^2 as shown in Fig. 1, the spacing between the dots was 0.12 µm. The dynamic properties (spin waves) of the arrays were tested by means of Brillouin light scattering spectroscopy (BLS) in the backscattering geometry, using a computer controlled tandem Fabry-Pérot interferometer in backscattering geometry. The wavevector of the incident light was applied either parallel or perpendicular to the applied magnetic field, so that the geometry of the magnetostatic backward volume mode or the magnetostatic surface mode (Damon-Eshbach mode) was realized. The static magnetic properties of the arrays were checked using MOKE.

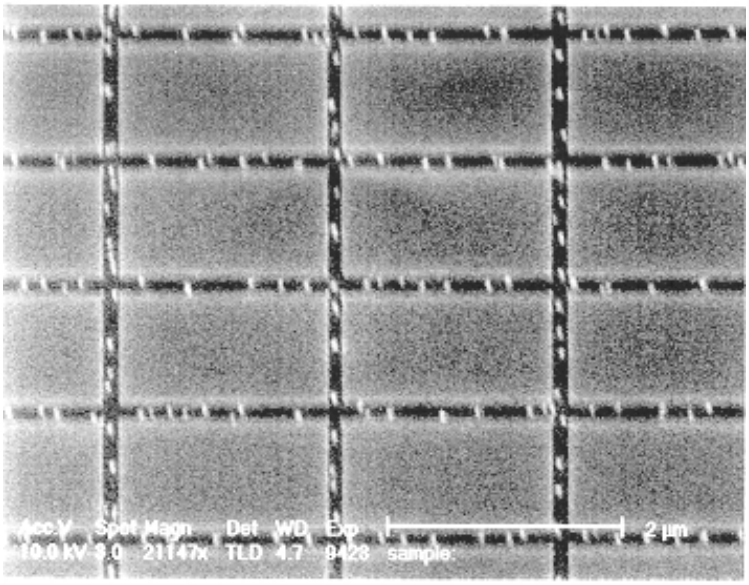

Fig. 1: SEM micrograph of an array of rectangular dots with the lateral dimensions of 1×1.75 μm^2, the spacing between the dots is 0.12 µm.

[1] In collaboration with E. Søndergard, C. Fermon, CEA Saclay, France.

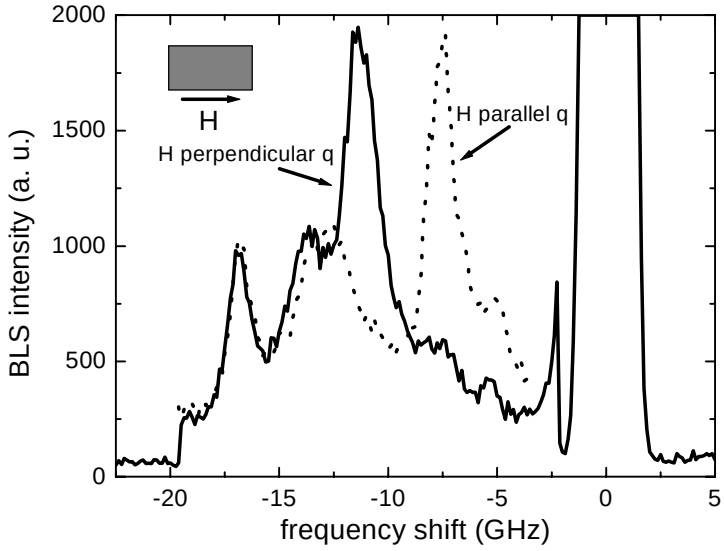

Fig. 2: Stokes side of a BLS spectrum for the 1×1.75 µm^2 sample, a wavevector $q_{||} = 0.75 \cdot 10^5$ cm^{-1} and an external field of 600 Oe. The dotted line shows the spectra for the backward volume mode ($q_{||}$ is parallel to the field) whereas the solid line represents the Damon-Eshbach geometry ($q_{||}$ is perpendicular to the field). Near 17 GHz the exchange dominated perpendicular standing spin wave mode appears for both geometries with the same intensity.

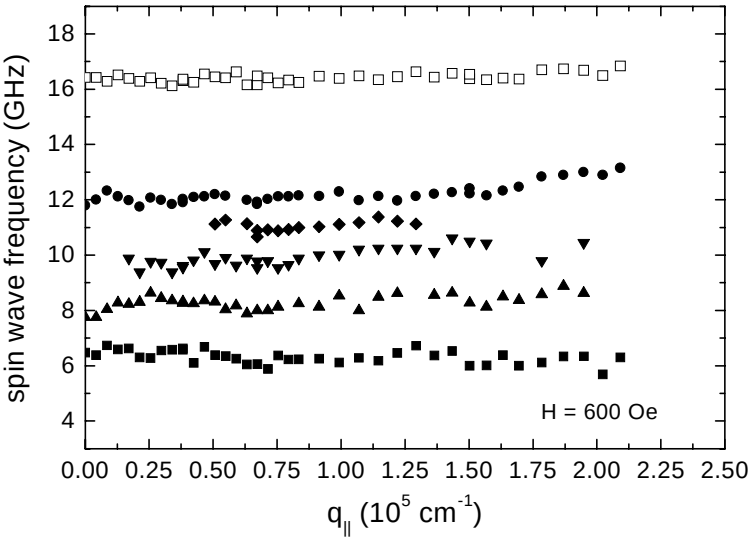

Fig. 3: Obtained dispersion for the sample with a thickness of 35 nm and the lateral dimensions 1×1.2 µm^2 in the Damon-Eshbach geometry. An external field of 600 Oe was applied along the long dot edges. The full symbols indicate the modes quantized due to the finite size of the dot, the open symbols represent the perpendicular standing spin wave mode.

Figure 2 shows the Stokes side of a BLS spectrum for the 1×1.75 µm^2 sample for the two different spin wave geometries. An external field of 600 Oe was applied along the long edges of the dot, the wavevector $q_{||} = 0.75 \cdot 10^5$ cm^{-1} was either parallel or perpendicular to the field. As it is seen in Fig. 2 several distinct modes are observed, which are all magnetic excitations as concluded from the field dependence of their frequencies. The peak at 17 GHz corresponds to the exchange dominated perpendicular standing spin wave mode, while the other peaks correspond to quantized spin wave modes. The modes appear in both geometries at the same frequencies but with different intensities. This can be understood as follows: Due to the lateral confinement the wavevector is not conserved in the light scattering process. The wavevector can be transferred between the light and the spin waves over a finite, continuous region, defined by the Fourier transform of the dynamic part of the magnetization, i.e., the confined spin wave. This applies for both in-plane wavevector components parallel and perpendicular to the scattering plane due to confinement along both directions. We thus believe that the difference in the light scattering intensities in the two geometries is connected with different Fourier components of the dynamic

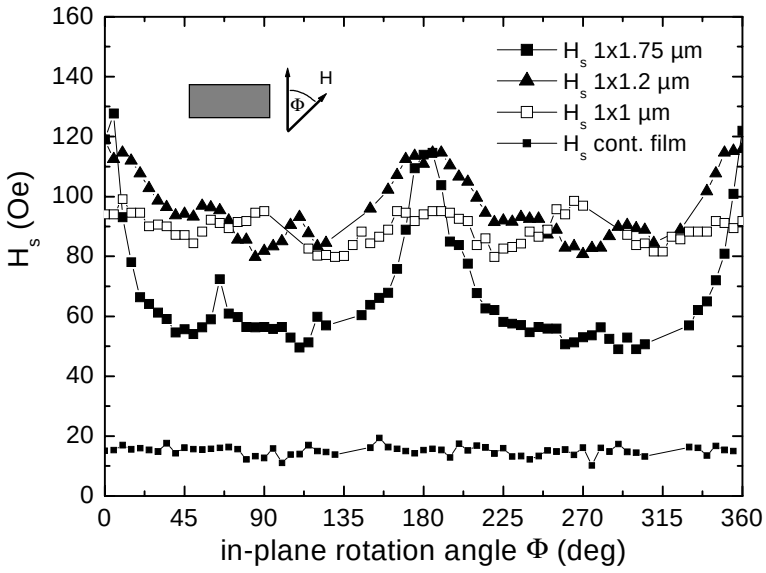

Fig. 4: Saturation field versus the in-plane angle demonstrating the influence of the dot shape for the three investigated arrays; in the lower part the data for the continuous film are shown for reference. For the rectangular dots (1×1.2, 1×1.75 µm^2) a twofold symmetry due to the sample shape is clearly observed, whereas the square sample shows a slight fourfold symmetry.

part of the mode magnetization taken for the in-plane transferred wavevector in the specific scattering process. By changing the angle of the incident light the value of the transferred wavevector was varied and the dispersion of each mode was measured as shown in Fig. 3 for the sample with the dot thickness d = 35 nm and dots with lateral dimensions of 1×1.2 µm^2. Similar to wires (see Sect. 6.6) [2] and circular dots (see Sect. 6.7) [3] several discrete dispersionless modes are observed in a finite wavevector interval.

The static magnetic properties of the arrays under investigation measured by MOKE are illustrated in Fig. 4. The in-plane saturation field is measured as a function of the in-plane angle between the applied field and the long edges of the dots. Since the dots are made of isotropic permalloy, the saturation field is determined by the demagnetization tensor of the dots and reflects their in-plane shape symmetry. In fact, the saturation fields of the rectangular dots demonstrate a

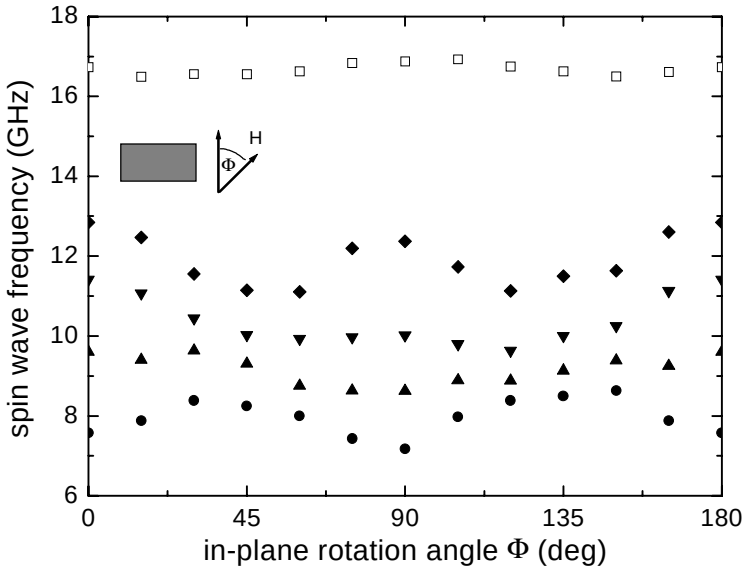

Fig. 5: Spin wave frequency measured as a function of the in-plane rotation angle for the sample with the lateral dimensions 1×1.75 µm^2. The external field of 600 Oe and the wavevector of $q_{||} = 0.42 \cdot 10^5$ cm^{-1} are perpendicular to each other (Damon-Eshbach geometry).

clear twofold in-plane symmetry, whereas the saturation field measured on the array of the square dots (1×1 μm^2) shows a weak fourfold symmetry. The results of the static measurements are in agreement with a calculation based on the approach developed in [4].

The in-plane symmetry of the quantized spin wave modes was also investigated by measuring the frequency of each mode as a function of the in-plane angle. The results of these measurements in the Damon-Eshbach geometry ($\vec{q}_{\parallel} \perp \vec{H}$) are demonstrated in Fig. 5 for the sample with lateral dot dimensions of 1×1.75 μm^2. The observed changes of the mode frequencies are too large to be explained by the in-plane variation of the static demagnetization field. Moreover, it is clear from Fig. 5 that the modes can be divided into two groups: the modes having the same twofold in-plane symmetry as the static field and the modes having a higher (fourfold) symmetry. The measurements performed on the square dots (not shown) reveal the fact that the frequencies of the former modes become in-plane isotropic, while the latter keep their fourfold symmetry.

The observed higher in-plane symmetry of some of the spin wave modes is completely unexpected, since usually the symmetry of the spin waves coincide with the symmetry of the magnetic static ground state. A theory describing quantized spin waves in rectangular dots is needed to explain the observed phenomenon.

Work supported by the Deutsche Forschungsgemeinschaft, the BMBF (Leitprojekt Magnetoelektronik) and the TMR network “Dynaspin”.

References

[1] C. Mathieu, C. Hartmann, M. Bauer, O. Büttner, S. Riedling, B. Roos, S.O. Demokritov, B. Hillebrands, Appl. Phys. Lett. **70**, 2912 (1997).
[2] C. Mathieu, J. Jorzick, A. Frank, S.O. Demokritov, B. Hillebrands, B. Bartenlian, C. Chappert, D. Decanini, F. Rousseaux, E. Cambril, Phys. Rev. Lett. **81**, 3968 (1998).
[3] J. Jorzick, S.O. Demokritov, B. Hillebrands, B. Bartenlian, C. Chappert, D. Decanini, F. Rousseaux, E. Cambril, Appl. Phys. Lett., in press.
[4] R.I. Joseph, E. Schlömann, J. Appl. Phys. **36**, 1579 (1965).

6.9 Magnetization reversal of a Stoner-particle due to short magnetic field pulses

M. Bauer, J. Fassbender, and B. Hillebrands[1]

Magnetic device applications in the field of magnetic sensors and storage elements demand a deeper insight into the switching dynamics caused by magnetic field pulses, especially on the

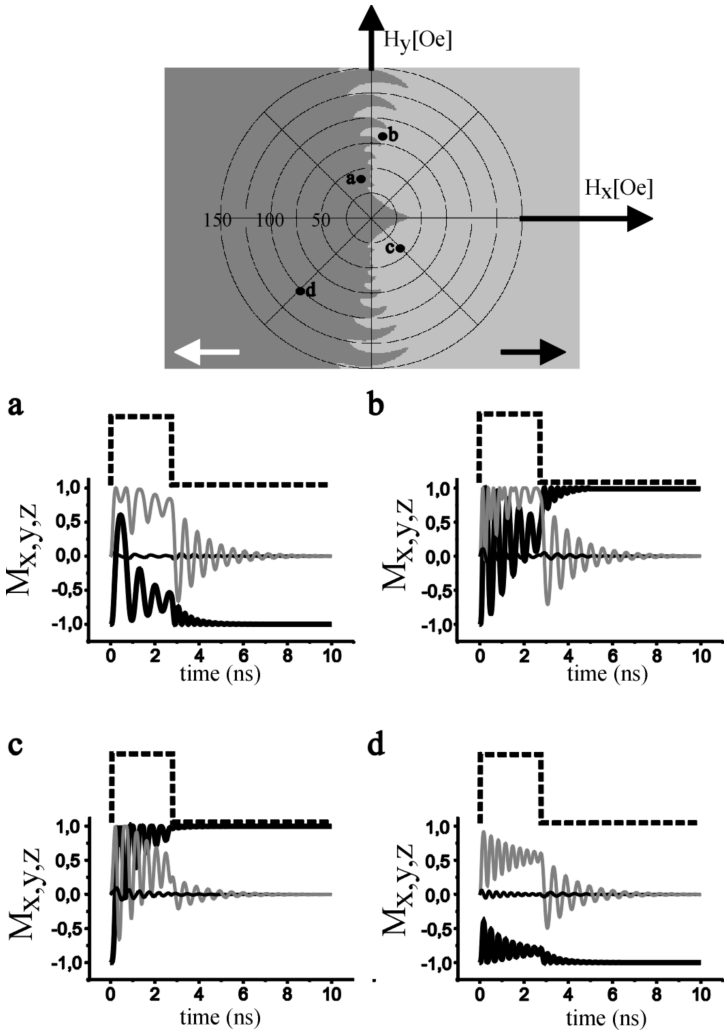

Fig. 1: Switching diagram of an ellipsoidally shaped particle with the demagnetizing factors $N_x = 0.008$, $N_y = 0.012$ and $N_z = 0.980$, i.e., the *x*-axis is the easy magnetization axis. The initial direction of magnetization is along the –*x*-direction. A rectangularly shaped field pulse of 2.75 ns is applied. Bright (dark) areas indicate that the magnetization has switched (not switched) from the –*x*-direction into the +*x*-direction. The direction of each point of the diagram from the center indicates the direction of the applied field pulse. The strength of the field pulse is proportional to the distance from the center. The circles show increments of the field strength of 25 Oe. The four panels display the time evolution of the three magnetization components M_x (bold black line), M_y (thin gray line) and M_z (thin black line) at the positions indicated in the switching diagram. The time structure of the applied field pulse (normalized to one) is shown by the dashed line.

[1] In collaboration with R.L. Stamps, University of Western Australia, Perth, Australia.

time scale where the length of the field pulse is comparable or shorter than the relaxation time of the magnetization. Here dynamic effects dominate the switching behavior [1].

We assume Stoner-like magnetic elements, e.g., ellipsoids, characterized by demagnetizing factors in *x*-, *y*- and *z*-direction N_x, N_y, and N_z. All calculations are performed for permalloy (saturation magnetization $4\pi M_S$ = 10.8 kG, gyromagnetic factor γ = 0.0176/(Oe·ns), Gilbert magnetic damping factor α = 0.008). The motion of the magnetization $\vec{M}$ under the influence of an effective magnetic field $\vec{H}_{\text{eff}}$ including a phenomenological damping mechanism is described by the Gilbert form of the Landau-Lifschitz equation:

$$\frac{\partial \vec{M}}{\partial t} = -\gamma \vec{M} \times \vec{H}_{\text{eff}} - \frac{\gamma\,\alpha}{M_S} \vec{M} \times \left(\vec{M} \times \vec{H}_{\text{eff}}\right). \tag{1}$$

The first term on the right hand side is the precession term and the second is the damping term. The effective field H_{eff} is defined by the sum of all fields acting on the magnetization. The re-

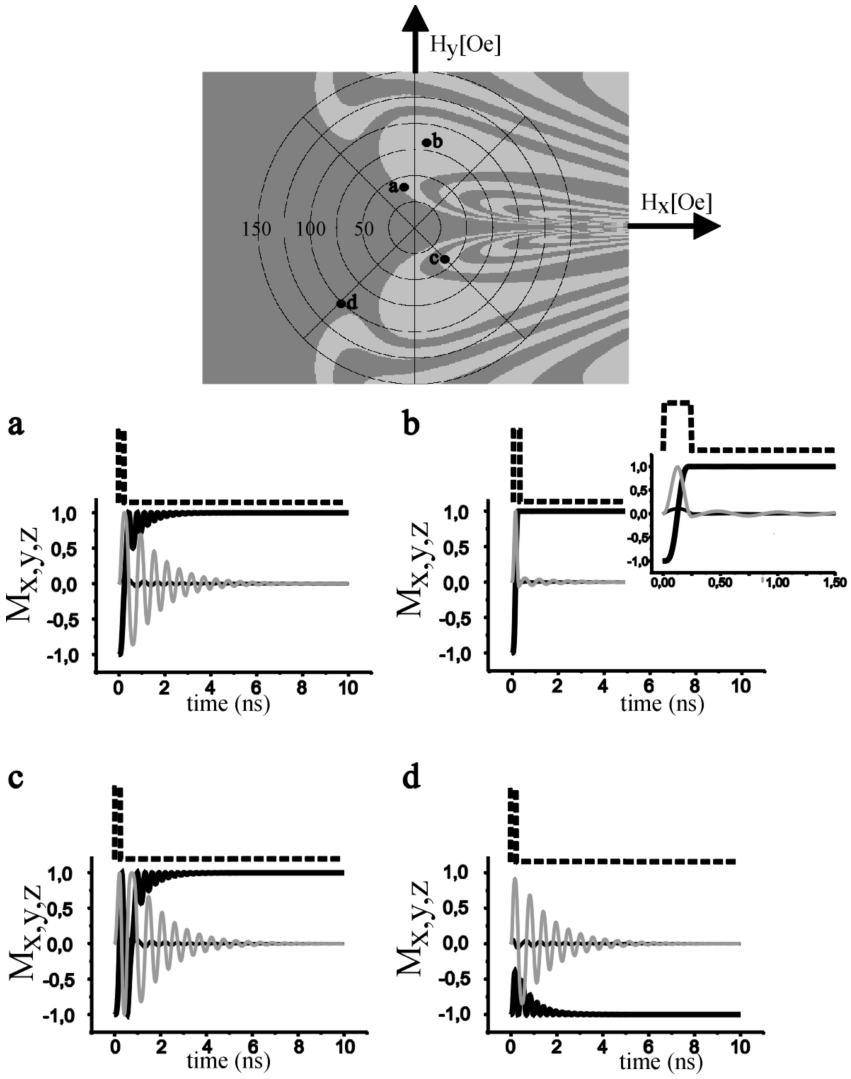

Fig. 2: Switching diagram for a rectangularly shaped field pulse of 0.25 ns. All other parameters as in Fig. 1. For (b) the absence of ringing is shown in the inset with an expanded time scale.

sults are obtained by straightforward numerical integration.

In Figs. 1 and 2 the switching diagrams for the application of a rectangularly shaped field pulse of 2.75 and 0.25 ns duration are presented. In each figure the four diagrams labeled a) to d) show the time evolution of the three mutual magnetization components at different values of field strength and direction.

For long magnetic field pulses the switching behavior is dominated by the magnetization relaxation process. Thus only applied field pulses with a positive *x*-component may lead to a switching of the magnetization from the –*x*- to the +*x*-direction. Only at the boundary (*x*-component of the magnetic field pulse is close to zero) small deviations from this behavior are observed. A closer inspection of point a) in Fig. 1 suggests, that a decrease of the pulse duration leads to a switching, since during the application of the field pulse the precessing magnetization vector has also positive values of its *x*-component. This calculation has been performed for point a) in Fig. 2. For a pulse duration of 0.25 ns switching is achieved. Another remarkable situation is found in point b) of Fig. 2. While switching is usually accompanied by a considerable ringing of the magnetization after pulse termination, the ringing is suppressed here. The origin of this behavior is simply that the pulse terminates at the moment the *z*-component of the magnetization crosses zero. This is energetically favorable since at this point the Zeeman energy, which will be dismissed upon field termination, is the major energy contribution. In all other cases the ringing of the magnetization is qualitatively the same. For ultrafast applications the suppression of the ringing is important since only in this case consecutive pulses can be applied to a memory cell in, e.g., a magnetic random access memory without dead time.

Reference

[1] M. Bauer, J. Fassbender, B. Hillebrands, R.L. Stamps, Phys. Rev. B, in press.

6.10 Switching behavior of Stoner-like magnetic thin film elements

M. Bauer, R. Lopusnik, J. Fassbender, and B. Hillebrands

Subject of this study is the switching behavior of Stoner-like magnetic thin film elements upon the application of very short field pulses. This was recently experimentally realized by the Siegmann group using packets of high-energy electrons of the Stanford linear accelerator to penetrate the magnetic film [1–3]. The magnetic elements are characterized by demagnetizing fields characteristic for ellipsoidally shaped, very thin islands. We model the magnetic sample ($4\pi M_S = 17.8$ kG) by a two-dimensional array of homogeneously magnetized, non-interacting thin film elements, each reflected by a pixel in the graphs shown in Figs. 1 and 2. To compare our results to the experiments reported in [1–3] we assume that an electron pulse of 4 ps duration penetrates through the center of the film (*xy*-plane) in the –*z*-direction creating a strong circular in-plane magnetic field. On this time scale the pulse shape plays no significant role, therefore we use a rectangular one. The magnetic field has a value of 100 kOe at $r = 1$ µm apart from the center and varies with a $1/r$ dependence. The results are obtained by straightforward numerical integration of the Landau-Lifschitz equation with a Gilbert damping term. For further details we refer to [4, 5]. For a sample with a uniaxial perpendicular anisotropy field of 50 kOe Fig. 1 shows the time evolution of all three mutually orthogonal magnetization components (left: M_x/M_S, middle: M_y/M_S, right: M_z/M_S) as a function of time. The gray scale reflects the value of the normalized magnetization components (-1/1 corresponds to black/white). Prior to the magnetic field pulse the sample is homogeneously magnetized along the –*z*-direction. Hence the *x*- and *y*-component are gray in Fig. 1, and the *z*-component is black over the entire image (not shown in Fig. 1). The image size is 100×100 µm^2. At the time $t = 0$ ps a bunch of electrons starts to penetrate perpendicularly through the center of the sample generating a circular in-plane magnetic field, which forces the magnetization vectors radially away from the center. Since the magnetization and the effective field direction are no longer collinear, the magnetization starts to precess about the effective field direction. The area influenced by the in-plane magnetic field pulse is enlarged until the pulse terminates at the time $t = 4$ ps. Hereafter, solely the effective anisotropy field, which is aligned along the *z*-direction, acts on the magnetization. Since M_z varies across the sample, the effective anisotropy field and hence the precession frequency do so as well. A dephasing of neighboring magnetization vectors is the result (cf. $t = 10$ and 36 ps in Figs. 1 and 2). In the areas, where M_z is ± 1 at the time of pulse termination, the relaxation is completed immediately while in the areas where $M_z \approx 0$ the relaxation time is largest. The final magnetization state is reached in the whole sample after $t \approx 550$ ps.

Figure 2 shows the much more complex behavior of an in-plane magnetized film with an in-plane uniaxial anisotropy field of 1 kOe. The main difference is that in this case the in-plane anisotropy field and the shape anisotropy field are perpendicular to each other. Prior to the magnetic field pulse the sample is homogeneously magnetized along the –*x*-direction. The magnetic field pulse is the same as in Fig. 1. The image size is 300×300 µm^2. At the first moment of the field pulse the effective field has only in-plane components, and consequently the magnetization rotates towards the $\pm z$-direction resulting in a strong demagnetizing field. The magnetization vectors start to precess about the effective field direction, which is no longer in-plane, and which changes continuously. At the time the pulse terminates ($t = 4$ ps in Fig. 2) there are areas with large *z*-components of the magnetization near the center of the sample. In these areas the effective field has a large value (due to the shape anisotropy) and its direction is nearly perpendicular (out-of-plane). Further away from the center the effective field value decreases and its direction

turns more and more into the film plane. The perpendicular effective field near the center leads to a rich variety of fine structure in the *x*- and *y*-components of the magnetization (compare $t = 38$ ps and 100 ps in Fig. 2) similar to the dephasing effect for the perpendicularly magnetized sample of Fig. 1. After about $t \approx 800$ ps the *y*- and *z*-components of the magnetization are relaxed, and the magnetization vectors lie parallel to the easy magnetization direction ($\pm x$-direction) in the final state.

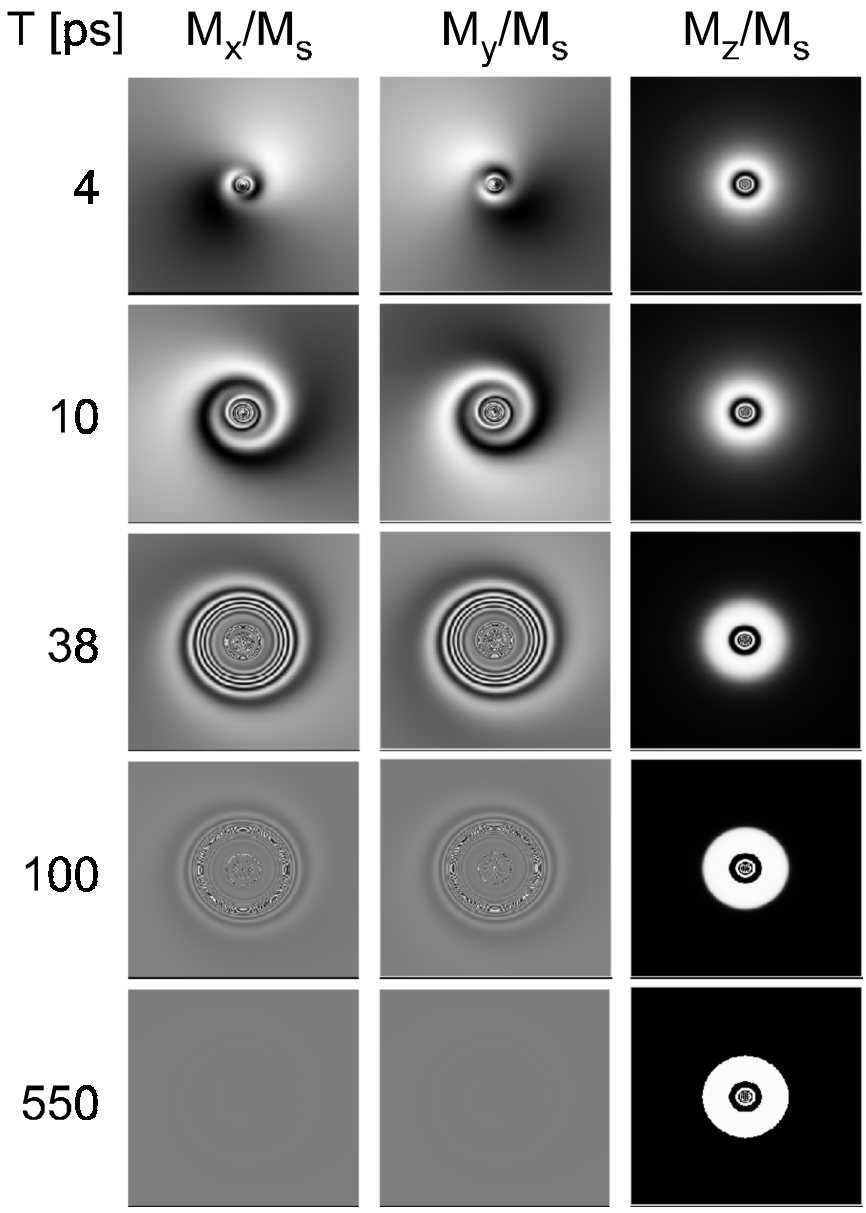

Fig. 1: Three normalized magnetization components M_x/M_s, M_y/M_s and M_z/M_s as a function of time (in ps) for a sample with a perpendicular anisotropy field of 50 kOe. The initial magnetization direction is along the $-z$-axis. The gray scale is a measure of the value of the normalized magnetization component (black/white corresponds to $-1/1$). A magnetic field pulse of 4 ps duration is applied at $t = 0$ ps. Sample area: 100×100 µm^2.

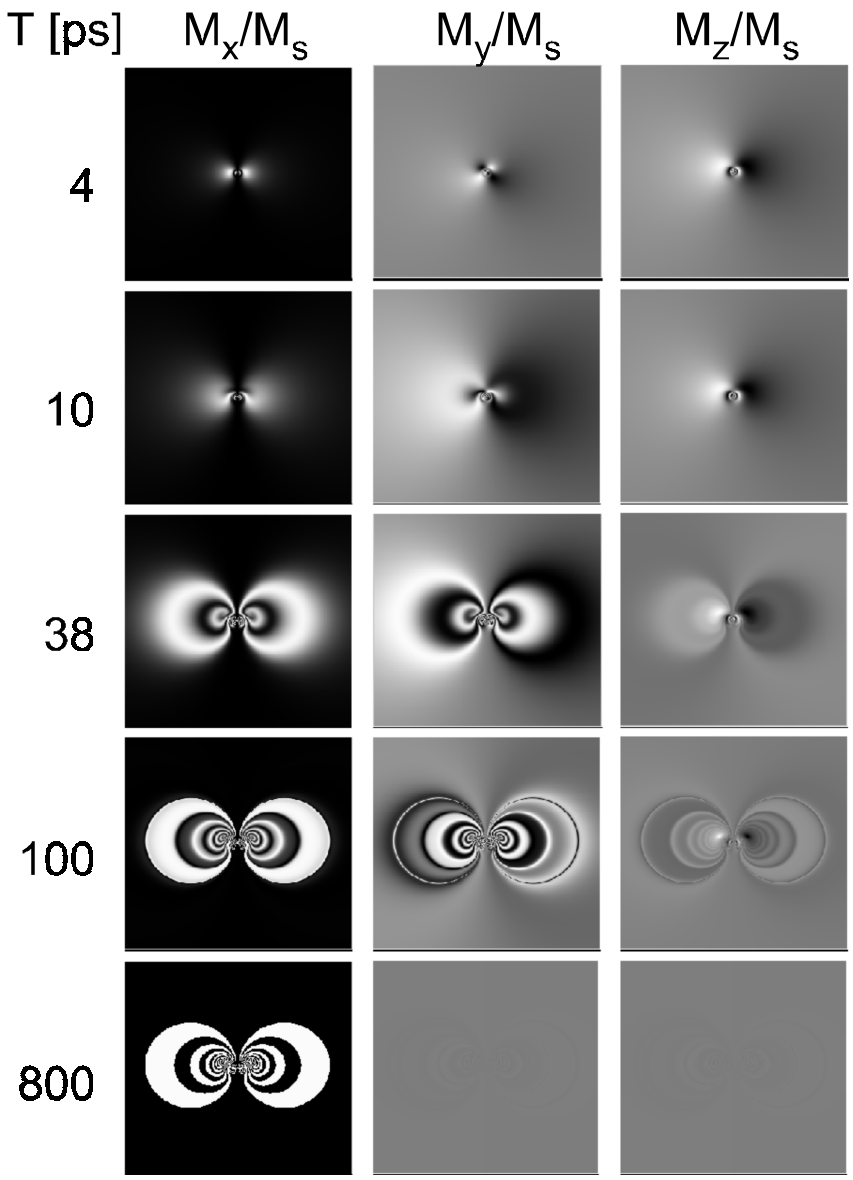

Fig. 2: Same graphic representation for a sample with a uniaxial in-plane anisotropy field of 1 kOe. The initial magnetization direction is along the $-x$-axis. Sample area: 300×300 µm^2. All other parameters are as in Fig. 1.

References

[1] H.C. Siegmann, E.L. Garwin, C.Y. Prescott, J. Heidmann, D. Mauri, D. Weller, R. Allenspach, W. Weber, J. Magn. Magn. Mater. **151**, L8 (1995).
[2] C.H. Back, D. Weller, J. Heidmann, D. Mauri, D. Guarisco, E.L. Garwin, H.C. Siegmann, Phys. Rev. Lett. **81**, 3251 (1998).
[3] C. H. Back, R. Allenspach, W. Weber, S. S. P. Parkin, D. Weller, E. L. Garwin, and H. C. Siegmann, Science **285**, 864 (1999).
[3] M. Bauer, J. Fassbender, B. Hillebrands, R.L. Stamps, Phys. Rev. B, in press.
[4] M. Bauer, R. Lopusnik, J. Fassbender, B. Hillebrands, submitted to J. Magn. Magn. Mater.

6.11 Successful suppression of magnetization precession after application of short field pulses

M. Bauer, R. Lopusnik, J. Fassbender, and B. Hillebrands

For the next generation of magnetic storage devices, like magnetic random access memories (MRAM), not only the data density but also the read/write time is of essential importance. One of the limiting factors in these applications is the time needed to write a single bit, i. e., the time for reversing the magnetization state. Of particular importance is to avoid a large precession amplitude of the magnetization ("ringing") after application of a field pulse used to switch the direction of magnetization. The appearance of ringing will increase the dead time required to make two consecutive switching events successful. It is generally believed, that the adjustment of the magnetic damping parameter, which is responsible for the energy dissipation in the magnetic film, is of key importance. However, we have recently shown by numerical simulations, that, as an alternative approach, ringing can be suppressed by tailoring the applied field pulse [1]. We report first experimental results [2] demonstrating, that the ringing of magnetization after application of a pulsed magnetic field can be suppressed by adjusting the field pulse parameters.

To investigate the dynamic properties, we have developed a time resolved magneto-optical Kerr effect magnetometer utilizing a stroboscopic technique (see Sect. 6.21). Time resolution is realized by application of magnetic field pulses to the sample, and by testing the magnetization state by means of the longitudinal magneto-optic Kerr effect using a time delayed, pulsed ps-IR diode laser operating at a wavelength of λ = 813 nm and a repetition rate from single shot up to 1 MHz (pulse duration of 10 ps, energy of 10 pJ/pulse, over-all time resolution of the setup 100 ps).

Results are presented for a single crystalline lutetium bismuth iron garnet (BIG) sample. The sample size ($1 \times 1.2 \times 0.0015$ mm^3) is chosen to have comparable demagnetization factors as typical for sub-µm-size MRAM memory cells. To verify the theoretical model of the ringing suppression we have chosen BIG over more technologically relevant materials for two reasons: i) iron garnet films are known to exhibit a very low magnetization damping constant leading to a strong magnetization ringing after the field pulse termination. Hence the concept of the pulse field adjustment should show up in large effects. ii) The anisotropy fields and the saturation magnetization are small resulting in low precession frequencies. Thus the magnetization ringing is pronounced and easy to investigate with the time resolution available.

The experiment has been performed in the following way (cf. inset of Fig. 1): A static magnetic field of 4 Oe was applied in the film plane in order to create an easy magnetization direction and a single domain state perpendicular to the plane of light incidence. An in-plane field pulse of 0.6 Oe has been applied along the hard axis leading to a non-zero magnetization component M_x contributing to the longitudinal Kerr effect. The maximum tilt angle between the magnetization and the equilibrium direction is found to be 9°. The time response of the magnetization after field pulse excitation has been investigated for different field pulse durations, T_{pulse}. The results are shown in Fig. 1.

For the shortest magnetic field pulse used in our experiment (T_{pulse} = 1.4 ns), we find a pronounced magnetization ringing after the termination of the field pulse. By successive increase of T_{pulse}, the ringing amplitude decreases and vanishes for T_{pulse} = 3.2 ns. By further increasing T_{pulse} the ringing recovers again with a maximum at T_{pulse} = 4.4 ns. As a function of pulse duration, the ringing amplitude oscillates after pulse termination with a full suppression at

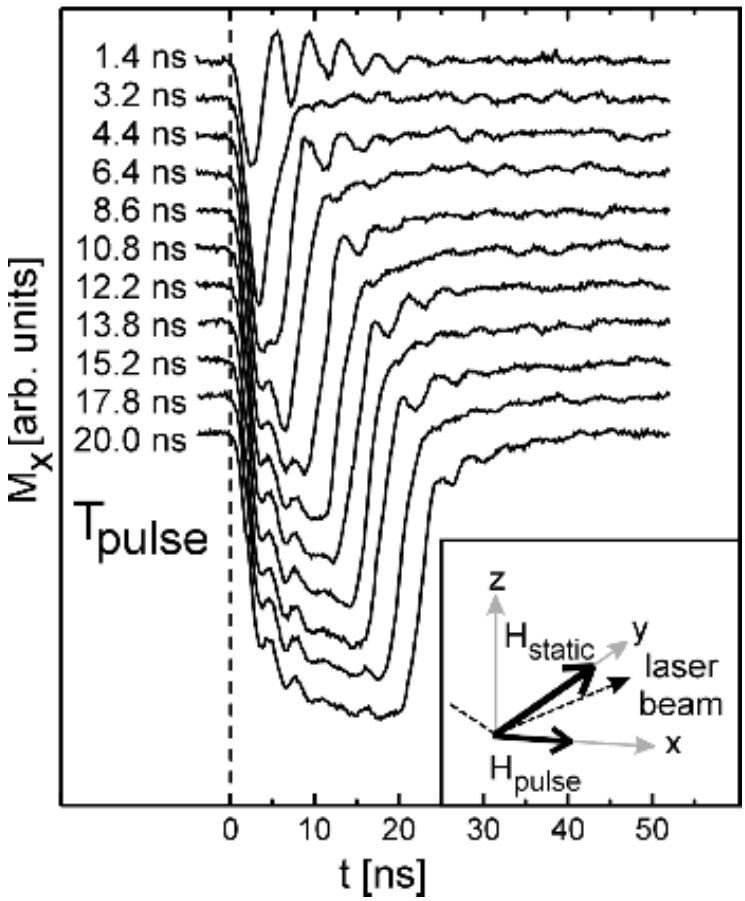

Fig. 1: Time evolution of the x-component of the magnetization, M_x, measured at the center of the sample during and after field pulse excitation for different pulse durations, T_{pulse}, as indicated. The beginning of the pulse launch is at $t = 0$ ns.

Inset: Coordinate system and geometry of the experiment.

T_{pulse} = 3.2 ns, 6.4 ns, 10.8 ns, 13.8 ns, and 17.8 ns; its amplitude decreases in between with increasing pulse duration. The suppression of the magnetization ringing shows up most pronounced by comparing T_{pulse} = 1.4 ns and 3.2 ns. For $T_{pulse} \geq 4.4$ ns, a damped ringing of the magnetization is observed during the application of the field pulse, which is not affected by the pulse duration.

These results can be fully understood by considering the interplay between the Zeeman energy originating from the static and the pulsed magnetic fields. In order to suppress the magnetization ringing, the field pulse must terminate at the moment at which most of the total magnetic energy is contained in the Zeeman energy of the pulsed magnetic field, which will be dismissed upon field termination. Only a small, residual amount of magnetic precession energy remains in the system which is later dissipated by a magnetic dissipation mechanism.

Work supported by Siemens AG, BMBF and the European Union (TMR project Dynaspin). We like to thank H. Dötsch for providing the BIG sample.

References

[1] M. Bauer, J. Fassbender, B. Hillebrands, R.L. Stamps, Phys. Rev. B, in press.
[2] M. Bauer, R. Lopusnik, J. Fassbender, B. Hillebrands, submitted to Appl. Phys. Lett.

D. Magnetic Anisotropies and Exchange Bias Systems

6.12 Magnetic anisotropies of epitaxial Fe films on vicinal to Ag(001)/GaAs(001) substrates

A.R. Frank, J. Jorzick, M. Rickart, M. Bauer, J. Fassbender, S.O. Demokritov, and B. Hillebrands[1]

We report on investigations of the crystallographic structure and the magnetic anisotropies of epitaxial iron films deposited onto periodically stepped Ag(001) surfaces using low energy electron diffraction (LEED), x-ray diffraction (XRD), as well as Brillouin light scattering (BLS) spectroscopy. The focus of the present study lies on the interrelation between the surface morphology of the buffer layers and the magnetic properties of the Fe films. In particular, the break in symmetry at the atomic steps is found to create an uniaxial magnetic anisotropy contribution.

Vicinal to (001) GaAs wafers with *fcc*-Ag buffers were used in this work as substrates for preparation of *bcc*-Fe films [1]. The GaAs wafers of orientation (1 1 11) and (1 1 17), as well as (0 0 1)-oriented substrates for reference, were chemically cleaned and heated in ultrahigh vacuum to remove the oxides and adsorbates. To achieve epitaxial growth of the 1500 Å thick *fcc*-Ag buffer layer the cleaned wafer was covered with a 10 Å thick Fe seed layer. After deposition the Ag buffer was annealed at 570 K for 1 hour to improve the surface morphology. *bcc*-Fe films of different thicknesses were deposited onto the Ag buffer. The films were finally covered with a 20 Å thick Ag film and a 20 Å thick Cr cap layer.

The crystallographic structure of the films was controlled *in situ* by LEED. After annealing the Ag buffer the LEED images show a crossing of vicinal and lattice reflexes as a function of the electron energy, as displayed in Figs. 1a,b. This is a finger print of an ordered step structure on the surface of the Ag buffer layer with an inclination angle relative to the atomic lattice. The

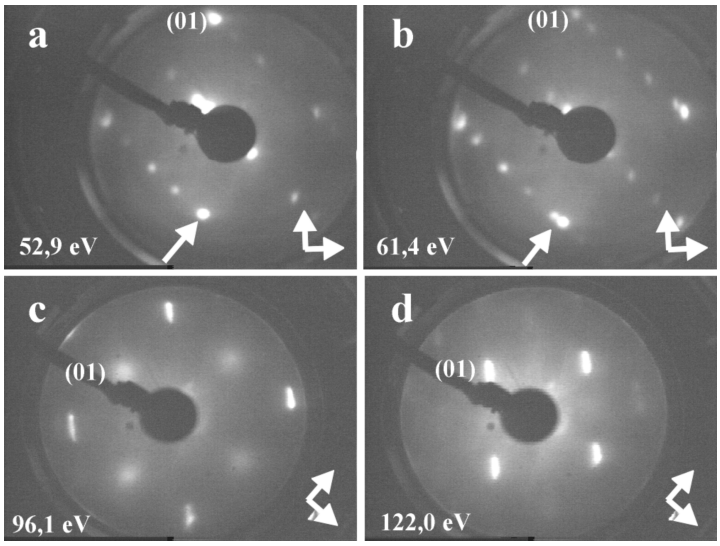

Fig. 1: LEED-images taken from the Ag buffer (a, b) after annealing showing an energy depending spot splitting. The electron energy is in a) 52.9 eV and in b) 61.4 eV. The images of the Fe-film (c, d) show elongated spots along the step direction. The electron energy is in c) 96.1 eV and in d) 122 eV. The (01)-spots of the surface unit cell are marked. The orientation of the sample is indicated by the coordinate system.

[1] In collaboration with M. Scheib, Institut für Oberflächen- und Schichtanalytik GmbH, Universität Kaiserslautern.

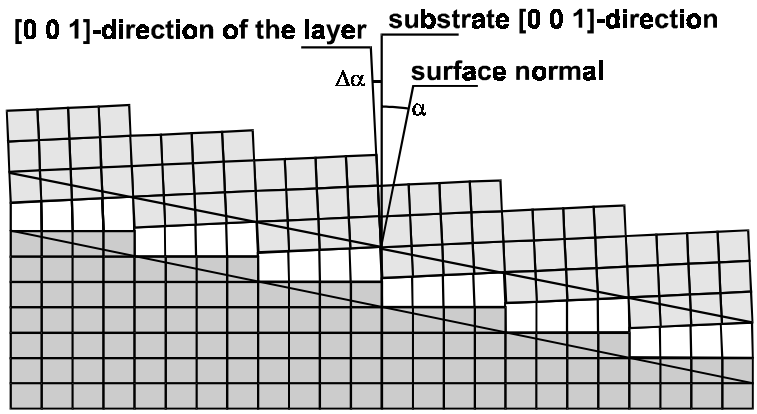

Fig. 2: A model of a vicinal interface generating an additional tilt angle Δα. This additional angle depends on the out-of-plane lattice mismatch and the average terrace width between two atomic steps. The [0 0 1]-direction of the upper and the lower layer and the direction perpendicular to the interface are displayed.

periodicities of the steps [2] with a terrace width of 11.5±2 Å and 18.0±2 Å determined from the LEED data deviate from periodicities resulting from the miscut angle measured by XRD (see below) by less than 10 %, which is within the error of the LEED measurements. LEED images taken from the Fe films show that the energy depending spot crossing vanishes, the LEED-spots are instead elongated (Fig. 1c,d). This indicates a non-regular step distribution on the surface with an averaged terrace size of approximately 8 Å in the direction perpendicular to the steps.

The vicinal miscut of the substrate, the Ag buffer layer and a 1000 Å Fe film was verified by XRD. It was found, that the angles of crystal orientation with respect to the surface normal between the three materials deviate from each other. For the (1 1 17)-oriented sample the vicinal angles of GaAs, Ag and Fe are 4.91° , 6.09° and 3.94° respectively. The angles for the (1 1 11) oriented sample are 6.99°, 8.75° and 5.61°. The observed difference is due to the different crystallographic structures of the substrate and the layers. Although the in-plane mismatch between the substrate and the layers is only a few percent, the out-of-plane lattice mismatch is much larger and of the order of 30 %, since the *bcc* unit cell of Fe grows onto the *fcc* unit cell of Ag with an in-plane rotation angle of 45°, resulting in a ratio of the perpendicular lattice parameters of Ag and Fe of about $\sqrt{2}$. In this context the film-to-film variation of the vicinal angle, as illustrated in Fig. 2, can be understood as follows [3]: For simplicity it is assumed in Fig. 2 that the out-of-plane adoption takes place just within one atomic layer (white layer in Fig. 2), and that the in-plane lattice mismatch is zero. It is seen in Fig. 2 that the [0 0 1]-directions of the lower and the upper layer deviate from each other by an angle Δα. The angle is given by geometric considerations: $\tan \Delta\alpha = (a_1\text{-}a_2)/t$, where a_1 and a_2 are the out-of-plane atomic step heights and t is the average terrace width. This additional inclination angle can be positive or negative depending on the sign of the out-of-plane misfit. In comparison with the experimental results we find that the theoretical value of the tilt angle is confirmed with an accuracy better than 5 % for the Ag-Fe interface. For the GaAs-Ag interface the measured value is only 55 % of the theoretical value for both studied vicinal miscut angles. but the influence of the Fe interlayer and the non-regular step distribution of the GaAs substrate on the additional miscut is unclear.

In order to determine the in-plane and the out-of-plane magnetic anisotropy contributions of twofold and fourfold symmetry, Brillouin light scattering (BLS) experiments on the Damon-Eshbach spin wave modes in the Fe films were performed on the samples with three different orientations of the substrate (1 1 11), (1 1 17) and (0 0 1) within a thickness range of the Fe films from 10 to 60 Å. Figure 3a shows the measured spin wave frequencies for a set of 20 Å thick Fe layers as a function of the in-plane angle φ_H between the direction of the external field and an in-plane [100] reference axis. Maxima in the spin wave frequencies indicate magnetic easy directions. In addi-

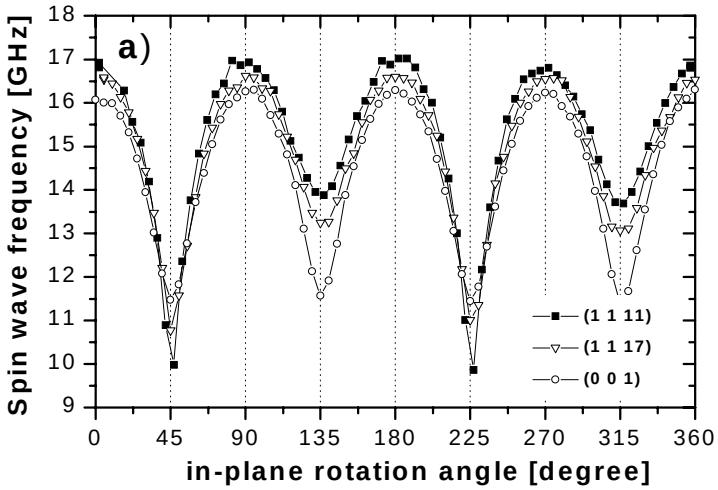

Fig. 3: a) Measured spin wave frequencies in 20 Å thick Fe-layers as a function of the azimuthal angle φ_H for three different substrate orientations. The measurements were taken with an external applied field of 1kOe. The maxima in the spin wave frequency indicate magnetic easy directions of the layer.

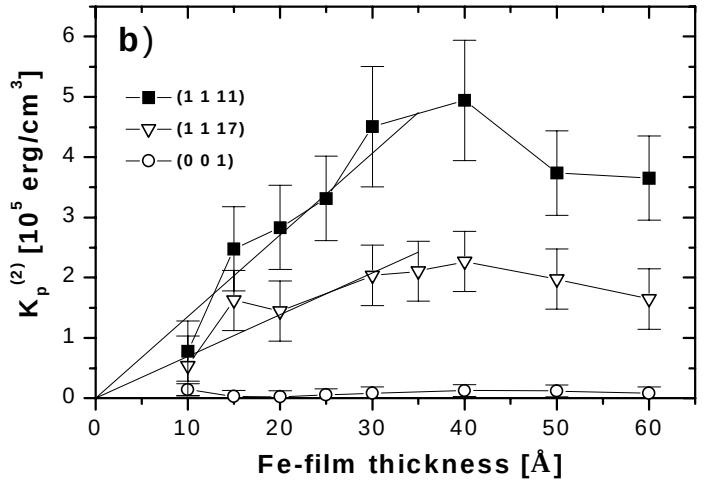

b) The anisotropy constant $K_p^{(2)}$ as a function of the Fe-film thickness for the three different vicinal angles. The straight lines indicate the initial slopes of the dependencies. The experimental data show a maximum of the twofold anisotropy at about 40 Å.

tion to the fourfold anisotropy, characteristic for the sample without miscut, an essential anisotropy contribution with twofold symmetry is clearly measured for the vicinal samples.

Different mechanisms contribute to the two-fold anisotropy contribution. First, bulk magnetocrystalline contributions must be considered. The in-plane anisotropy is determined by the projection of the tensor of the bulk magnetocrystalline anisotropy onto the film surface plane. This tensor has a cubic symmetry in the crystallographic reference frame, and it is independent of the film thickness. The vicinal orientation leads to a rotation of this tensor into the film coordinate system resulting in an twofold in-plane anisotropy, which in turn is independent of the film thickness. However, the measured twofold anisotropy is of one order of magnitude larger than the values one obtains from the rotation of the magnetocrystalline tensor, and it depends dramatically on the Fe film thickness. This means that the anisotropy is likely to be a step induced anisotropy of the Fe film, which can have different origins. Elastic strain (in-plane and out-of-plane) at the interface, especially at the atomic steps, gives rise to a magnetoelastic contribution [4]. In addition the band structure at the interface might be modified due to the reduced coordination number and the chemical environment.

For a quantitative description of the obtained results the anisotropy energy expression is chosen by:

$$E_{\text{ani}} = -K_s^{(2)} \cos^2 \vartheta + K_p^{(4)} \sin^4 \vartheta \cos^2 \varphi \sin^2 \varphi + K_p^{(2)} \sin^2 \vartheta \cos^2(\varphi - \varphi_0) \quad . \tag{1}$$

Here ϑ and φ are the polar and azimuthal angles, and φ_0 is the in-plane angle between the easy axis of the step induced uniaxial in-plane anisotropy and the reference [100] axis. The in- and out-of-plane anisotropy constants $K_p^{(2)}$, $K_s^{(2)}$ with twofold symmetry and the in-plane anisotropy constant $K_p^{(4)}$ with fourfold symmetry were determined by fitting the measured spin wave frequencies as a function of the azimuthal angle φ_H between the [100]-direction of the Fe film and the applied external field using a least squares fit routine. The details of the fit procedure and the underlying theory are described elsewhere [5]. While the obtained values of the out-of-plane anisotropy constant $K_s^{(2)}$ and the in-plane anisotropy constant $K_p^{(4)}$ are almost the same for all orientations, the twofold anisotropy constant $K_p^{(2)}$ increases with increasing film thickness for the Fe film thickness up to 30 Å (see Fig. 3b). The slope of the line is roughly proportional to the square of the vicinal angle. At about 40 Å the curves for both miscut angles show a characteristic maximum. This points to a relaxation behavior within the Fe film with increasing thickness. In other words, the main contribution to the observed anisotropy is due to the disturbance in the lattice of the Fe films near the steps caused by the large out-of-plane lattice mismatch between the Ag and the Fe layer. With increasing thickness of the Fe layer this disturbance is reduced or vanishes completely. This result is confirmed by BLS measurements performed on 1000 Å thick Fe layers displaying no twofold anisotropy contribution for all crystal orientations within the measurement accuracy.

Work supported by the Deutsche Forschungsgemeinschaft and the European Science Foundation.

References

[1] B.F.P. Roos, A.R. Frank, S.O. Demokritov, B. Hillebrands, J. Magn. Magn. Mater. **198-199**, 725 (1999).
[2] M. Henzler, Appl. Phys. **9**, 11 (1976).
[3] H. Nagai, J. Appl. Phys. **45**, 3789 (1974).
[4] D. Sander, Rep. Prog. Phys. **62**, 809 (1999).
[5] B. Hillebrands, Phys. Rev. B **41**,530 (1990).

6.13 Growth and magnetic anisotropies of epitaxial Fe films on vicinal to Ag(001)/MgO(001) substrates

M. Rickart, A.R. Frank, B.F.P. Roos, J. Jorzick, Ch. Krämer, S.O. Demokritov, and B. Hillebrands

The epitaxial growth and the magnetism of layered systems containing 3d magnetic metals is a research topic of great interest both in the areas of pure and applied physics. In this study we examine the epitaxial growth and magnetic anisotropies of Fe films prepared on Ag buffer layers grown on MgO substrates with (0 0 1)-orientation and a vicinal sample with (1 0 8)-orientation. The interrelation between the surface morphology of the buffer layers and the magnetic properties of the Fe films is the main motivation in this investigation.

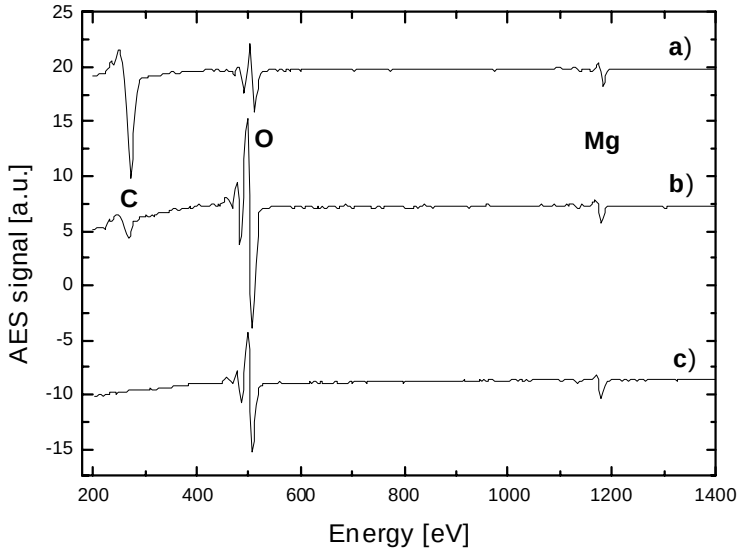

Fig. 1: Auger electron spectroscopy of the MgO substrate. Curve a) shows an AES spectrum of a MgO substrate after precleaning, curve b) shows the spectrum after annealing the substrate at 600 °C for two hours, curve c) shows the spectrum obtained after the bombardment with 25 eV oxygen ions for 5 minutes to remove the high carbon contamination.

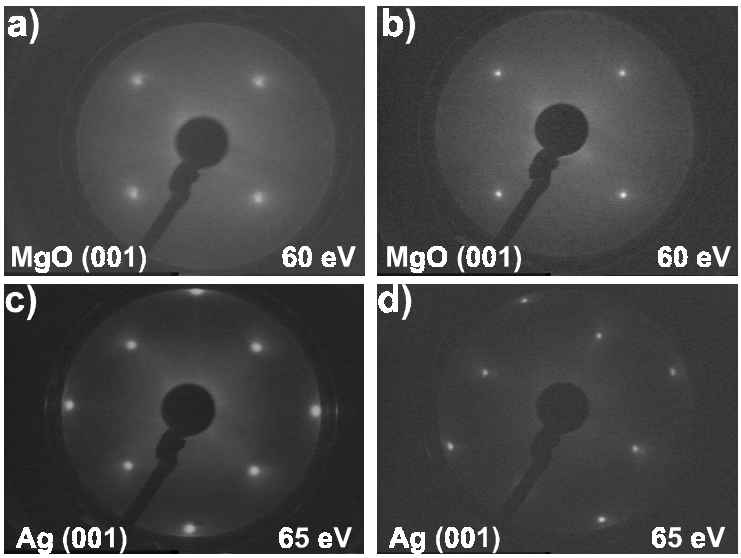

Fig. 2: LEED patterns of the substrate and of the Ag buffer layer: a) MgO(001) before and b) after ion beam oxidation. c) Ag buffer layer grown on a MgO substrate annealed at 600°C. d) Ag buffer layer grown on an ion beam oxidized MgO substrate.

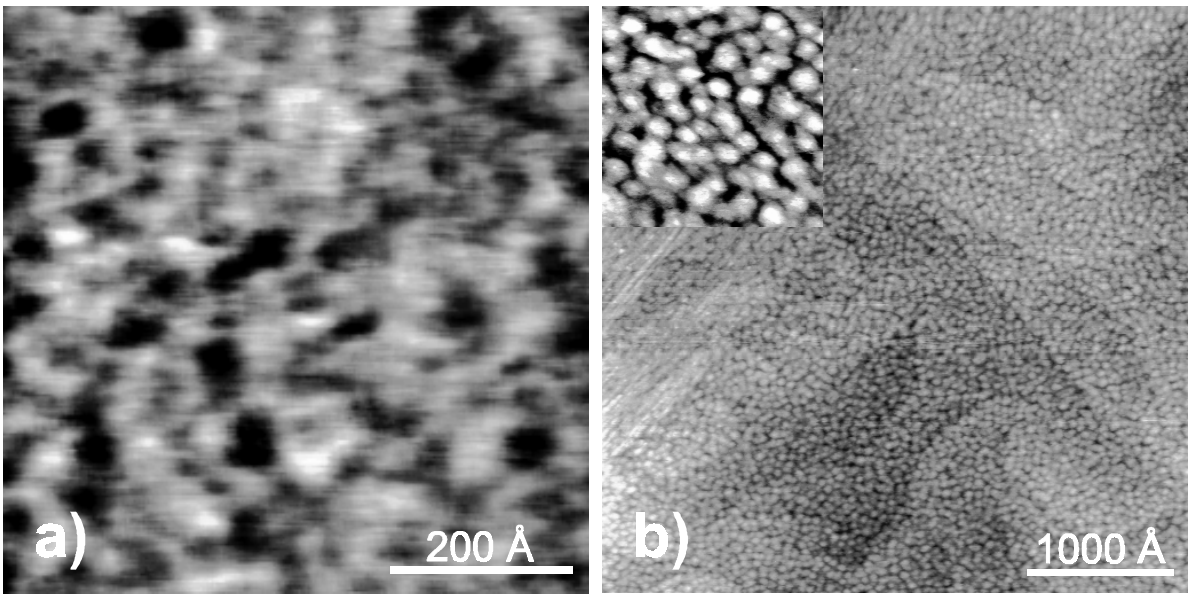

Fig. 3: a) Non-contact atomic force microscopy image of the MgO (0 0 1) substrate. Root mean square roughness RMS = 2.8 Å, Peak-to-Valley-Distance R_{p-v} = 20 Å. b) Scanning tunneling microscopy image of a Fe film grown on Ag (0 0 1) / MgO (0 0 1). RMS = 2 Å, R_{p-v} = 19 Å. Clearly visible are the atomic steps and terraces introduced by the Ag buffer. The inset zooms into a part of the image with a size of 500 Å × 500 Å.

The samples were prepared in a molecular beam epitaxy UHV system with a base pressure less than $5 \cdot 10^{-10}$ mbar. *In situ* crystallographic characterization was performed by low electron energy diffraction (LEED), and the chemical analysis by Auger electron spectroscopy (AES), as displayed in Figs. 1 and 2. Scanning probe microscopy was applied for topographical studies of the surfaces of MgO and Fe, see Fig. 3.

The substrates, polished MgO (0 0 1) wafers, were precleaned by ultrasound in isopropanol before loading them into the preparation chamber. AES reveals a high carbon contamination at the surface (Fig. 1a). To remove these carbon adsorbates the substrate was treated with a low energy (25 eV) O^+-ion beam with a beam current density of 0,15 mA/cm^2 for 5 minutes. As is seen in Fig. 1c, all carbon is removed within the sensitivity of the Auger analysis. The ion beam treatment also has a smoothing effect on the substrate as seen with non-contact atomic force microscopy. The surface roughness is measured to be 2.8 Å RMS, as displayed in Fig. 3a. A comparison of the AES spectra shown in Fig. 1 clearly shows that the ion beam oxidation procedure provides a much cleaner MgO-surface than the usually used annealing method at high (600°C) temperatures for several hours (Fig. 1b). The removal of the carbon contamination results in a better quality of the Ag buffer layer.

The growth of the Fe films is as follows: A 30 Å thin Fe nucleation layer followed by a Ag buffer layer deposited at a temperature of 130 °C with a rate of 1 Å/s were grown onto the substrate. The growth of the buffer was monitored by RHEED. Sharp spots forming Laue circles reveal a low roughness of the buffer over wide terraces corroborated by scanning tunneling microscopy (STM) studies. Sharp and well defined spots are also seen in the LEED measurements as displayed in Fig. 2d. Compared to a sample prepared by oxidation the sample with an annealed substrate shows much broader spots (Fig. 2c).

A high quality of the Ag buffer layer with a well defined surface is the starting point for the study of the growth of thin Fe films. A 30 Å thick *bcc*-Fe film was deposited at room temperature with a rate of 0.1 Å/s. Figure 3 b shows the topography of the Fe film surface measured with STM

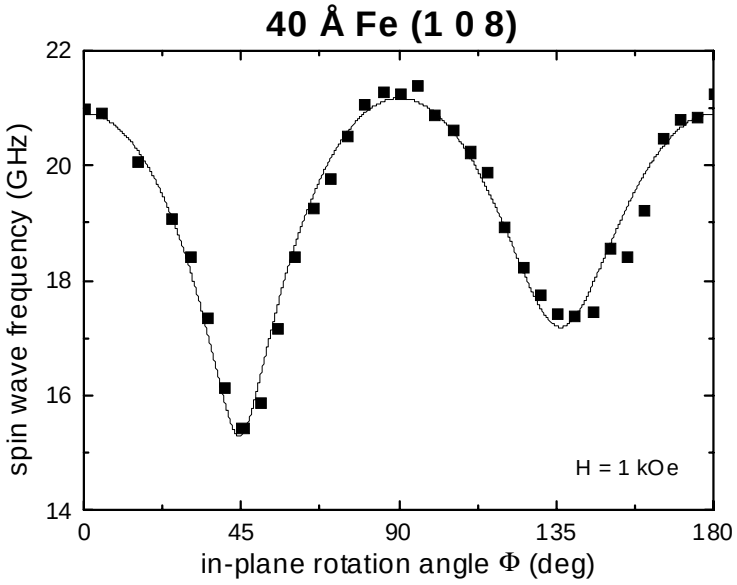

Fig. 4: Measured spin wave frequencies of a 40 Å thick Fe film with (1 0 8)-orientation as a function of the in-plane angle φ of the applied field of 1 kOe. The maxima in the spin wave frequencies indicate the easy axis. An uniaxial magnetic anisotropy is revealed by different frequencies at the two minima. The solid line is the result of the fit described in the text.

which exhibits 500 – 700 Å wide terraces. The surface roughness is 2 Å RMS. The growth mode is found to be the Stranski-Krastanov growth mode. The upper surface of the Fe film is covered by islands of about 50 Å diameter and of a height of one or two atomic layers.

To investigate the magnetic anisotropies of the grown Fe films, the frequency of the Damon-Eshbach spin wave modes of the (1 0 8) oriented vicinal sample were measured by Brillouin light scattering spectroscopy (BLS). Figure 4 shows the measured spin wave frequency versus the in-plane angle of the applied magnetic field. In addition to the dominating crystallographic fourfold anisotropy a twofold anisotropy contribution due to the broken symmetry at the surface was found. The corresponding in-plane anisotropies $K_p^{(4)}$ and $K_p^{(2)}$ as well as the out-of-plane anisotropy constant $K_s^{(2)}$ were obtained by fitting the measured spin wave frequencies (for the definition of these parameters see the previous contribution, Sect. 6.12). The fitted values of the anisotropy constants are $K_p^{(4)} = 3.7 \cdot 10^5$ erg/cm^3, $K_p^{(2)} = 1.2 \cdot 10^5$ erg/cm^3 and $K_s^{(2)} = 1.3 \cdot 10^6$ erg/cm^3.

The investigation of the microscopic origin of the observed anisotropy is the subject of ongoing studies.

Work supported by the Deutsche Forschungsgemeinschaft and the European Science Foundation.

6.14 Exchange anisotropy of epitaxial Fe/MnPd bilayers

T. Mewes, B.F.P. Roos, S.O. Demokritov, and B. Hillebrands[1]

Exchange coupling at the interface between a ferromagnetic and an antiferromagnetic layer is believed to cause exchange biasing, i.e. a shift of the hysteresis loop of the ferromagnetic layer along the field axis. This effect can be described phenomenologically by introducing an unidirectional in-plane interface anisotropy. Although the exchange bias effect has been experimentally studied for many systems, most of them being polycrystalline, the details of the exchange coupling mechanism remains a subject of discussion [1]. For a deeper understanding of the exchange bias effect studies of epitaxial exchange bias systems are needed. We report the fabrication of epitaxial Fe(001)/$Mn_{50}Pd_{50}$ exchange bias bilayers and an experimental study of their magnetic properties. The exchange bias effect in this system is accompanied by induced uniaxial and fourfold in-plane anisotropies.

MnPd has a CuAu-I-type ordered face-centered-tetragonal (*fct*) structure with lattice constants a = 4.07 Å and c = 3.58 Å. Previous studies [2] revealed that the ordered *fct*-structure of MnPd possesses an antiferromagnetic phase with a Néel temperature as high as 540° C.

By rotating the MnPd unit cell by 45° within the (001) plane the lattice misfit between the (001) planes of *bcc* Fe and *fct* MnPd is less than 0.3 %. Thus it can be expected that the MnPd layer grows epitaxially onto a *bcc* Fe(001) layer with the orientation relation: <110>MnPd || <100>Fe.

The samples were grown in an UHV system with a base pressure better then $5 \cdot 10^{-10}$ mbar. Fe and Pd were evaporated by means of a multipocket e-beam evaporator, while Mn was evaporated from an effusion cell. The growth rates were carefully controlled by a quartz microbalance and were 0.1 Å/s for Fe, Pd and 0.2 Å/s for MnPd, respectively. Epitaxial Fe(001)/MnPd samples with the structure Fe(40Å)/MnPd(200Å)/Pd(20Å) were grown at room temperature onto a

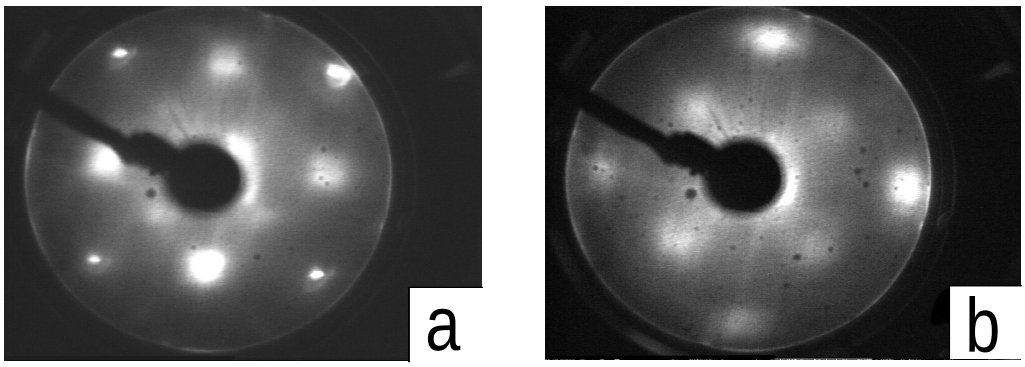

Fig. 1: LEED patterns at different layers of the epitaxial sample GaAs(001)/Fe(10Å)/Ag(1500Å)/Fe(50Å)/MnPd(200Å)/Pd(20Å):
(a): Fe(50Å), at an e-beam energy of 98 eV; (b): MnPd(200Å), at an e-beam energy of 62.9 eV.

[1] In collaboration with Y.J. Tang, X. Zhou and W.S. Zhan, State Key Laboratory for Magnetism, Institute of Physics, Chinese Academy of Sciences, Beijing, China.

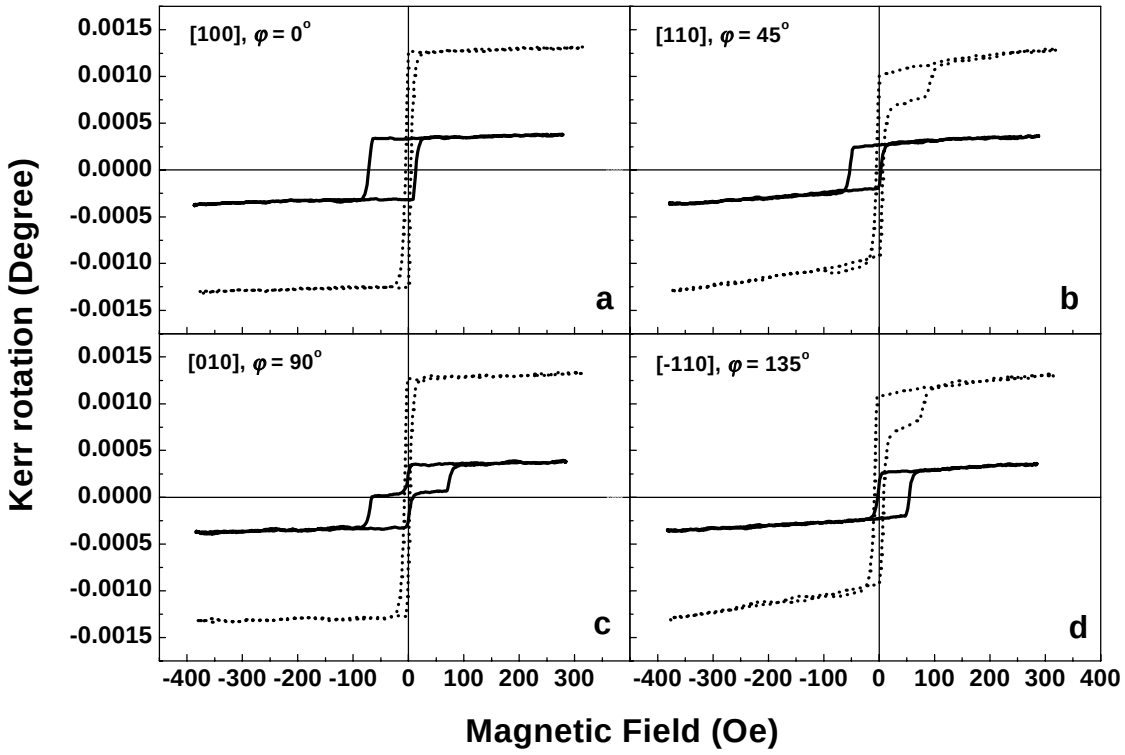

Fig. 2: MOKE hysteresis loops for the epitaxial samples
GaAs(001)/Fe(10Å)/Ag(1500Å)/Fe(40Å)/MnPd(200Å)/Pd(20Å) (solid lines) and
GaAs(001)/Fe(10Å)/Ag(1500Å)/Fe(40Å)/Pd(20Å) (dotted lines) at different orientations of the field with respect to the Fe layer:
(a): H//[100]; (b): H//[110]; (c): H//[010]; (d): H//[-110].
The seeming asymmetry of the hysteresis loops (b and d) for the sample without MnPd layer is due to interference between the linear and the quadratic MOKE contributions.

Ag(001) buffer, deposited onto GaAs(001) according to standard recipes [3]. A 20 Å thick Pd cap layer protects the sample against oxidization. A magnetic field of 50 Oe was applied along the [100] direction of Fe during growth to create the exchange bias effect. Chemical and crystallographic analyses of the prepared films were performed *in situ* by means of a calibrated Auger electron spectrometer and low energy electron diffraction (LEED). The magnetic properties of the prepared films were measured at room temperature by magneto-optic Kerr effect (MOKE) magnetometry. Torque measurements were performed at 77 K with an applied field of 10 kOe.

Fig. 1 presents typical LEED patterns of the Fe and the MnPd layer for an epitaxial Fe(001)/MnPd bilayer. The LEED patterns clearly demonstrate the epitaxial growth of both layers. However, due to an essential spreading of the LEED spots it cannot be definitely concluded that the tetragonal *c*-axis of MnPd is normal to the Fe(001) plane.

If the external field is applied parallel to the [100]-directions which are the magnetic easy axes, the epitaxial Fe(001) films exhibit square hysteresis loops. However, if the field is applied within an angular interval of about 15° around the [110] hard-axes, hysteresis loops with two irreversible jumps are observed as it is shown in Fig. 2b and Fig. 2d. The asymmetric shape of these loops is due to the quadratic magneto-optic Kerr effect contribution [4].

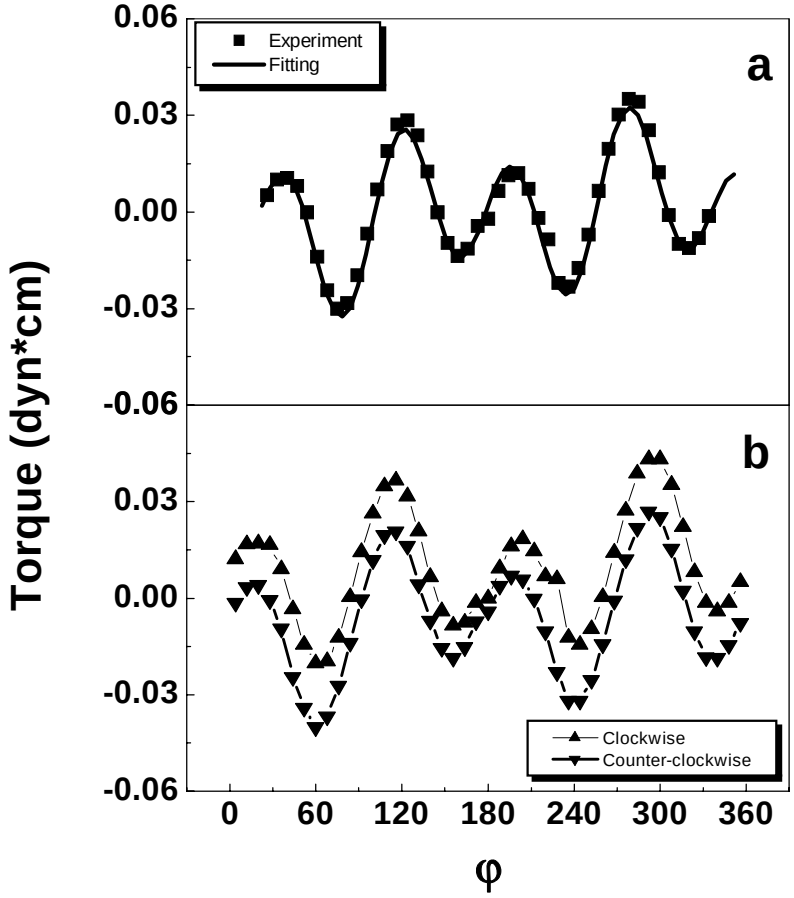

Fig. 3: Torque curves measured at 77K for the epitaxial sample
GaAs(001)/Fe(10Å)/Ag(1500Å)/Fe(50Å)/MnPd(200Å)/Pd(20Å):
(a): calculated and experimental torque curves (averaged over the clockwise and counterclockwise rotation);
(b): measured torque curves of the clockwise and counterclockwise rotation.

The hysteresis loop of the epitaxial Fe(001)/MnPd bilayers is, in general, shifted away from zero field, proving the existence of the exchange bias effect in this system. The shift is most obvious if the external field is applied along the easy [100]-direction (Fig. 4a). An enhanced coercive field compared to the Fe film is also evident. Two-jump hysteresis loops, similar to those observed in the Fe(001) film, are also observed in Fe(001)/MnPd bilayers as it is shown in Fig. 2c. The loops of the epitaxial Fe(001)/MnPd bilayers with the field applied at an arbitrary angle are more complicated than those of the Fe(001) films because of the competition between the unidirectional, the uniaxial and the fourfold anisotropy contributions in the system. From the analysis of the entire set of the obtained hysteresis loops one can conclude that the [100]-direction of Fe is the easy direction of the unidirectional, the uniaxial and the fourfold anisotropy. The [010]-direction is, in turn, an easy direction of the fourfold anisotropy, but the hard direction of the uniaxial anisotropy. However, due to the complexity of the measured magnetization loops it was impossible to determine the anisotropy constants from these measurements.

This task has been accomplished using the torque method. Due to rotational hysteresis [5], the torque results presented in Fig. 3a are the average of the results of the clockwise and counter-

clockwise rotation shown in Fig. 3b. If one supposes that the free energy F of the system can be written as:

$$F = -K_p^{(1)} \cos\varphi + K_p^{(2)} \sin^2\varphi + K_p^{(4)} \sin^2\varphi \cos^2\varphi \quad , \tag{1}$$

where $K_p^{(1)}$, $K_p^{(2)}$ and $K_p^{(4)}$ are the unidirectional, uniaxial and fourfold in-plane anisotropy constants, respectively. φ is the angle between the magnetization and the [100]-direction. The torque T is:

$$T = \partial F / \partial\varphi = -K_p^{(1)} \sin\varphi - K_p^{(2)} \sin 2\varphi - \tfrac{1}{2} K_p^{(4)} \sin 4\varphi \quad . \tag{2}$$

By using Eq. (2), the anisotropy contributions were obtained by fitting the experimental data: $K_p^{(1)} = 3.7 \cdot 10^4$ erg/cm^3, $K_p^{(2)} = 1.1 \cdot 10^5$ erg/cm^3, and $K_p^{(4)} = 4.1 \cdot 10^5$ erg/cm^3 (which is higher than the value measured on the Fe film – $K_p^{(4)} = 3.7 \cdot 10^5$ erg/cm^3). Thus, the exchange interaction between ferromagnetic Fe and antiferromagnetic MnPd, which causes the bias effect described by the unidirectional anisotropy, does not only introduce an additional uniaxial anisotropy, but also increases the already existing fourfold anisotropy in Fe(001) films.

Y. J. Tang would like to thank the Alexander von Humboldt Foundation for financial support during his stay at the University of Kaiserslautern. Work supported by the Deutsche Forschungsgemeinschaft.

References

[1] T.C. Schulthess, W.H. Butler Phys. Rev. Lett. **81**, 4516 (1998).
[2] H.P.J. Wijn, Magnetic Properties of Metals, in: Data in Science and Technology, R. Poerschke (Ed.), Springer-Verlag, Berlin Heidelberg (1991), p.81.
[3] P. Grünberg, S.O. Demokritov, A. Fuss, R. Schreiber, J.A. Wolf and S.T. Purcell, J. Magn. Mag. Mater. **104-107**, 1734 (1992).
[4] K. Postava, H. Jaffres, A. Schuhl, F. Nguyen Van Dau, M. Goiran, A.R. Fert, J. Magn. Magn. Mater. **172**, 199 (1997).
[5] W.H. Meiklejohn and C.P. Bean, Phys. Rev. **102**, 1413 (1956); **105**, 904 (1957).

6.15 Enhanced coercivity of exchange bias Fe/MnPd bilayers

T. Mewes, B.F.P. Roos, S.O. Demokritov, and B. Hillebrands[1]

Exchange coupling at the interface between a ferromagnetic (FM) and an antiferromagnetic (AF) layer can cause the exchange bias effect, i.e., a shift of the hysteresis loop of the FM layer along the field axis characterized by an exchange bias field H_{ex}, which is usually described as an in-plane unidirectional anisotropy [1]. Often the exchange bias effect is accompanied by an enhanced coercivity. Although several models predict correct order-of-magnitude values of the exchange bias field [2-5], they do not properly describe the increased coercivity. It was found that the interfacial roughness might influence the interfacial interaction between the two materials causing local spin dispersion, and resulting in local additional anisotropies. These anisotropies compete with demagnetization fields, and they may serve as an energy barrier to domain

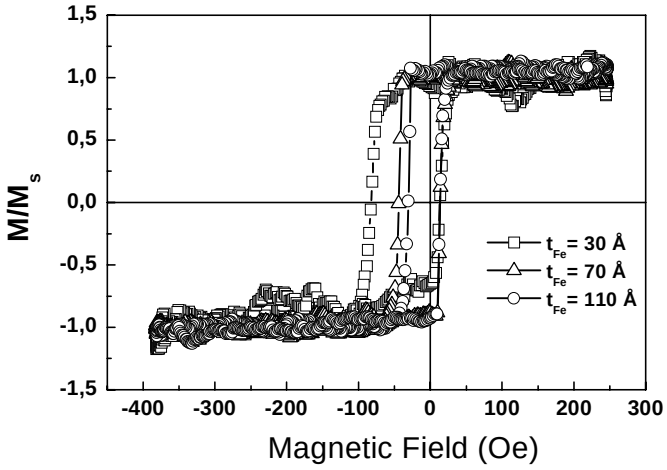

Fig. 1: Easy direction hysteresis loops for the polycrystalline samples $Si/SiO_2/Fe(t_{Fe})/MnPd(200Å)/Pd(20Å)$ at different Fe thicknesses t_{Fe} = 30 Å , 70 Å, and 110 Å.

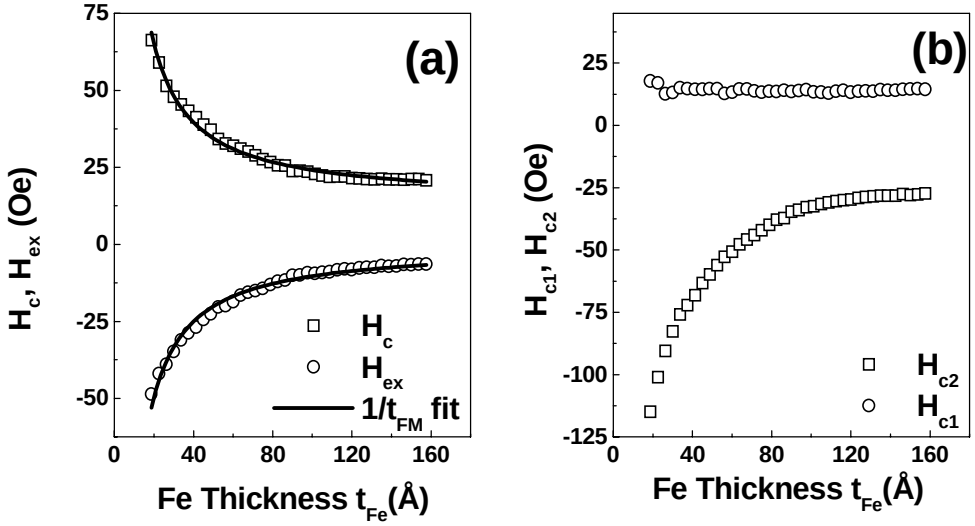

Fig. 2: a) Exchange-bias field H_{ex} and coercivity H_c as a function of the Fe film thickness, t_{Fe}. b) Coercivity H_{c2} on the left hand side of the hysteresis loop and coercivity H_{c1} on the right hand side of the loop of the sample $Si/SiO_2/Fe(t_{Fe})/MnPd(200Å)/Pd(20Å)$ as a function of the Fe film thickness, t_{Fe}.

[1] In collaboration with Y.J. Tang and Y.J. Wang, State Key Laboratory for Magnetism, Beijing, China.

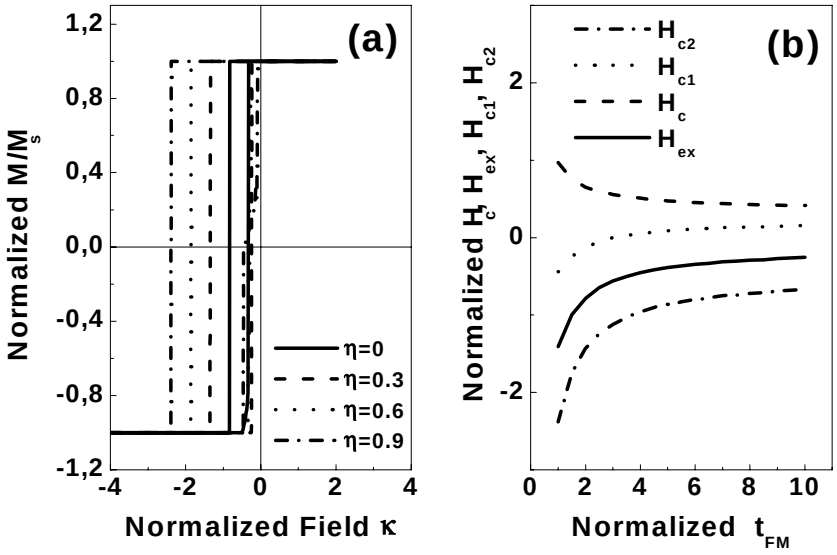

Fig. 3: a) Simulated hysteresis loops of the exchange-bias systems with different fourfold anisotropy contributions; (b) calculated values of exchange-bias field H_{ex}, total coercivity H_c, left and right coercive fields, H_{c1} and H_{c2} as a function of the thickness of the FM layer. In a) the parameter η is proportional to the fourfold in-plane anisotropy contribution $K_p^{(4)}$.

wall motion leading to an increase in the coercivity [6]. In addition, higher order anisotropies, which originate from the exchange interaction between the AF and the FM layers, are also found to have a strong influence on the coercivity [7].

In this contribution we present a study of the enhanced coercivity of the exchange-bias bilayer system Fe/MnPd. By using a phenomenological model we find indications that the enhanced coercivity in this system is caused by higher-order anisotropies which originate from the exchange interaction between the Fe and the MnPd layer.

The samples with the structure Si/SiO_2/Fe(t_{Fe})/MnPd (200 Å)/Pd (20 Å) were grown at room temperature in an MBE system. During growth a magnetic field of 50 Oe was applied along the surface of the samples. *In situ* Auger electron spectroscopy was used to monitor the composition of the MnPd layer. The crystallographic structure of the films was studied by X-ray diffraction with Cu K_α radiation, and the magnetic properties were measured by magneto-optic Kerr effect (MOKE) magnetometry at room temperature.

Figure 1 presents typical easy-direction hysteresis loops of the samples for different Fe thicknesses of t_{Fe} = 30 Å, 70 Å, and 110 Å, respectively. As one can see, the hysteresis loops are shifted to negative fields exhibiting exchange-bias coupling in the system. The thickness dependence of the easy direction exchange-bias field H_{ex} and coercivity H_c are shown in Fig. 2a. H_{ex} varies from about 50 Oe to 5 Oe with increasing Fe thickness from 20 Å to 160 Å following an inverse Fe thickness dependence, indicating that the exchange coupling is an interface phenomenon. A second interesting phenomenon is that the coercivity H_{c1} on the right side of the hysteresis loop remains almost constant with varying Fe thickness, while the coercivity H_{c2} on the left side increases with increasing Fe thickness, as displayed in Fig. 1. Fig. 2b presents the thickness dependence of H_{c1} and H_{c2}, which clearly shows that the increase of coercivity with decreasing Fe thickness is mainly due to the increase of left coercivity H_{c2}.

It is believed that the interfacial roughness may be the cause for the enhanced coercivity since interfacial roughness can provide more interfacial area and spin dispersion causing a higher coercivity [6]. In this case the coercive field is strongly related to the details of the microstructure of the films, which may vary from sample to sample. From our study we believe that there is a more intrinsic property caused by the exchange coupling effect itself, that can produce a higher coercivity. It has been recently shown by micro-magnetic calculations that the spin-flop exchange coupling in the CoO/Co exchange bias system can induce an uniaxial anisotropy, which in turn causes a large contribution to the coercivity [8]. It was also found in our previous studies of the Fe/MnPd system [9] that the unidirectional, uniaxial and fourfold anisotropy contributions are largely increased compared to a pure Fe film. All these enhanced in-plane anisotropies exhibit a strong interfacial character.

To properly understand the enhanced coercivities in our samples, we propose a model based on the idea of Mauri et al. [2] by introducing an additional fourfold anisotropy contribution in the total free energy of the interface of the FM/AF structure (for details see [10]). Minimizing the energy expression one can find the magnetization orientations of both the FM and the AF layer and, thus, simulate the magnetization curves of the bilayer. The exchange-bias field H_{ex} and the coercivity H_c are determined from the obtained curves. Fig. 3a presents calculated magnetization curves in the easy direction for different values of the in-plane fourfold anisotropy constant, $K_p^{(4)}$. The dimensionless factor η shown in the figure is proportional to $K_p^{(4)}$. It is clear from Fig. 3a that with increasing η the left coercivity increases substantially, causing an increase of both the exchange-bias field and the coercivity, while the right coercivity changes only slightly. The thickness dependence of H_c and H_{ex} are also computed. In agreement with the experimental results the proportionality of H_c and H_{ex} to the inverse Fe thickness is obtained in the simulations as shown in Fig. 3b. The calculated left and right coercivities are also presented in Fig. 3b. We have found that contrary to H_{c1}, H_c and H_{ex} the calculated right coercivity H_{c2} even slightly increases with increasing FM layer thickness. Thus, in our model the enhanced coercivity is mainly due to the high value of the left coercivity, H_{c1}. However, more realistic models are needed to reach a quantitative agreement with the experimental results and to obtain a clearer picture of the enhanced coercivities of FM/AF systems.

Y. J. Tang would like to thank the Alexander von Humboldt Foundation for financial support of his stay in Kaiserslautern. Work supported by the Deutsche Forschungsgemeinschaft.

References

[1] W.H. Meiklejohn, C.P. Bean, Phys. Rev. **102**, 1413 (1956); **105**, 904 (1957).
[2] C. Mauri, H.C. Siegmann, P.S. Bagus, E. Kay, J. Appl. Phy. **62**, 3047 (1987).
[3] A.P. Malozemoff, Phys. Rev. B **35**, 3679 (1987); J. Appl. Phys. **63**, 3874 (1988); Phys. Rev. B **37**, 7673 (1988).
[4] N.C. Koon, Phys. Rev. Lett. **78**, 4865 (1997).
[5] T.J. Moran, J. Nogues, D. Lederman, I.K. Schuller, Appl. Phys. Lett. **72**, 617 (1998).
[6] Z. Qian, J.M. Sivertsen, J.H. Judy, J. Appl. Phys. **83**, 6825 (1998).
[7] C. Mathieu, M. Bauer, B. Hillebrands, J. Fassbender, G. Güntherodt, R. Jungblut, J. Kohlhepp, A. Reinders, J. Appl. Phys. **83**, 2863 (1998).
[8] T.C. Schulthess, W.H. Butler, Phys. Rev. B **56**, 83(1997).
[9] Y.J. Tang, B. Roos, T. Mewes, M. Bauer, M. Scheib, S.O. Demokritov, B. Hillebrands, submitted to Phys. Rev. B.
[10] Y.J. Tang, B. Roos, T. Mewes, M. Bauer, M. Scheib, S.O. Demokritov, B. Hillebrands, and Y.J. Wang, Appl. Phys. Lett. **75**, 707 (1999).

6.16 *In situ* Brillouin light scattering investigations on epitaxial and polycrystalline CoO/Co bilayers oxidized by controlled ion beam oxidation

A.R. Frank, J. Jorzick, B.F.P. Roos, M. Rickart, J. Fassbender, S.O. Demokritov, and B. Hillebrands

We report on investigations of the magnetic behavior of the CoO/Co bilayer system measured by *in situ* Brillouin light scattering (BLS) experiments. Poly- and single-crystalline Co layers were grown onto uncovered silicon substrates as well as onto silicon substrates covered with a 1000 Å thick Cu buffer layer in order to achieve epitaxial growth. The initial Co layer thickness was varied in a thickness range from 10 Å to 120 Å. Without breaking the vacuum the samples were oxidized in a low energy oxygen ion beam with an oxidation time range from a few seconds up to more than one hour. The well defined ion beam is characterized by adjustable beam current (0.2 mA/cm^2) and beam energy (30-300 eV), small width of the energy distribution and high atomic oxygen rate. This guaranties a reproducible oxidation process. The ratio of oxygen and argon in the plasma is chosen to 60:40. The vacuum pressure is $2.1 \cdot 10^{-3}$ mbar during oxidation.

The samples were magnetically characterized by means of *in situ* Brillouin light scattering. The frequency of the Damon-Eshbach spin wave mode was measured as a function of the initial Co layer thickness, the temperature and the oxidation time.

In Fig. 1 the spin wave frequency as a function of the film thickness of a polycrystalline CoO/Co sample is shown. The measurements were performed at room temperature and at T = 77 K. For the unoxidized samples the measured frequencies demonstrate only a weak temperature dependence. They are slightly increased at 77 K in comparison with the values obtained at room temperature. This can be attributed to an increased value of the film magnetization and/or anisotropy. The oxidized samples show a reduced spin wave frequency at room temperature over the whole thickness range. The observed drop is correlated with the fact that the spin wave frequency of the Damon-Eshbach mode decreases with decreasing magnetic film thickness. Since the magnetic film thickness is reduced by the oxidation process, the frequency is expected to decrease. From the frequency changes the thickness of the oxidation depth can be estimated. About 20–40 Å Co of the initial ferromagnetic Co layer thickness is transformed into CoO. This

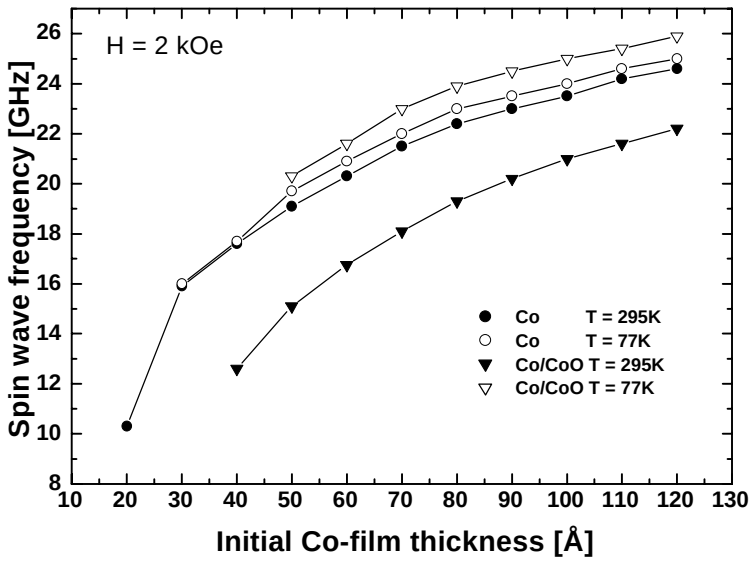

Fig. 1: Spin wave frequency of the Damon-Eshbach mode as a function of the initial Co layer thickness prior and after the oxidation process at room temperature and T = 77K. The oxidation time for the samples was chosen to be 15 min. The applied external field is 2 kOe. Below the thicknesses, where the data points end, no BLS signal was found.

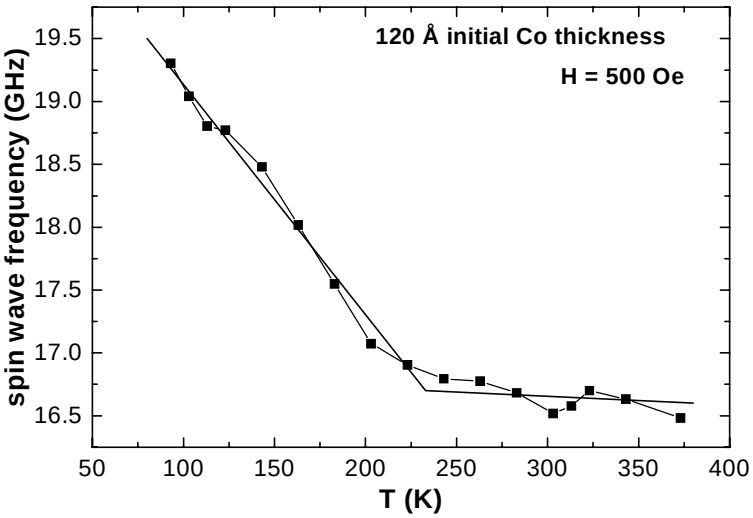

Fig. 2: Spin wave frequency of the Damon-Eshbach mode as a function of temperature. The initial film thickness of the oxidized Co layer is 120 Å. The external applied field is 500 Oe. The straight line is a guide to the eyes.

is confirmed by vibrating sample magnetometry measurements, where the total magnetic moment of the samples is determined. At room temperature the moment has been determined both for a Co layer and a CoO/Co layer with the same initial film thickness of 120 Å. From the decrease in magnetic moment an oxidation depth of 20 Å was obtained. At T = 77 K, the oxidized samples show a large increase in spin wave frequencies, which are even higher than the frequencies obtained from the unoxidized samples with the same initial Co film thickness. This is valid for the full investigated thickness range.

The spin wave frequencies of the 120 Å thick polycrystalline Co film show almost no temperature dependence. On the contrary, the spin wave frequencies of the CoO/Co bilayers demonstrate an essential temperature dependence. Figure 2 shows the temperature dependence of a CoO/Co bilayer film with an initial Co layer thickness of 120 Å. It is seen that below 230 K the spin wave frequency increases with decreasing temperature in a roughly linear manner. The reason for this behavior is yet unclear. This notable change is possibly attributed to the antiferromagnetic ordering which gives rise to a strong influence on the ferromagnetic Co layer and thus to the spin wave frequencies. Another possibility to explain the observed change is a temperature dependent coupling at the interface between the Co and the CoO layer.

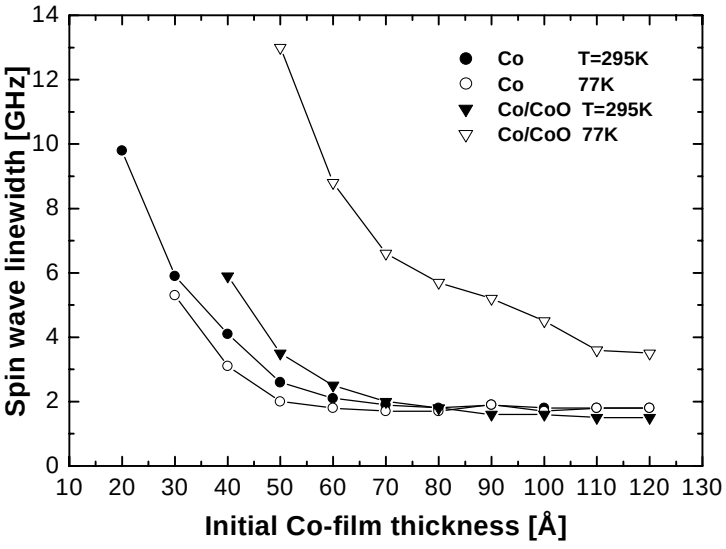

Fig. 3: Spin wave linewidth as a function of the initial Co layer thickness prior and after oxidation and at two different temperatures (T = 77 K and room temperature). Below the thicknesses, where the data points end, no BLS signal was found.

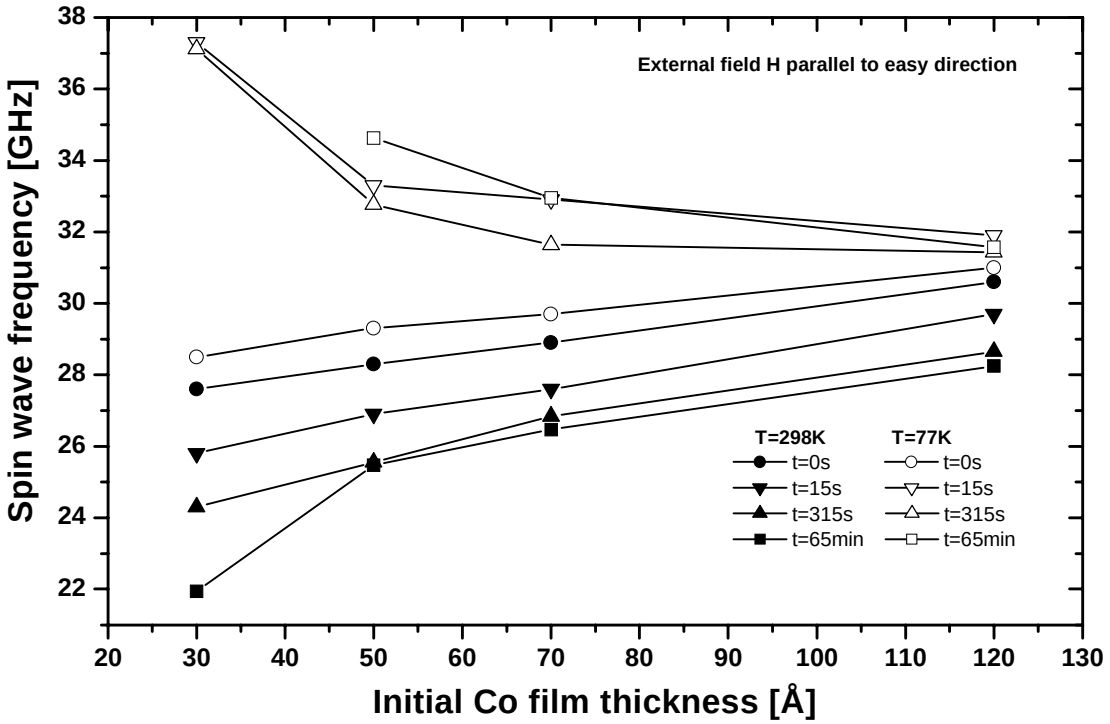

Fig. 4: Spin wave frequency as a function of the initial Co film thickness for the epitaxial samples. The direction of the external field H = 2 kOe is applied parallel to the easy direction of the Co film. Curves with different oxidation times and at two different temperatures (T = 77 K and room temperature) are displayed.

In Fig. 3 the spin wave linewidth for the oxidized and unoxidized samples at room temperature and at T = 77 K is displayed versus the initial Co layer thickness. While the behavior of the unoxidized samples and the oxidized samples at room temperature is very similar, it is found that the oxidized samples at a temperature of 77 K show an essential line width broadening over the full thickness range.

The epitaxially grown Co layers were successively oxidized in three steps up to a total oxidation time of 15 s, 315 s and 65 min. In Fig. 4 the obtained spin wave frequencies as a function of the initial Co layer thickness are displayed. The direction of the external field in the BLS setup is applied parallel to the easy direction of the Co film. It is shown, that the spin wave frequency at a temperature of 77 K increases with increasing oxidation time. This is in contrast to the spin wave frequency behavior measured at room temperature at which the spin wave frequency decreases with increasing oxidation time. The effect is more pronounced at thinner film thicknesses. This indicates a thickness dependent interface mechanism leading to the observed behavior of the spin wave frequencies.

Further investigations are necessary in order to obtain a deeper insight into the physical mechanisms leading to the observed experimental results. Especially the role of the antiferromagnetic order of the CoO and the coupling mechanism at the CoO/Co interface are of great interest.

Work supported by the Deutsche Forschungsgemeinschaft.

6.17 Oscillatory exchange bias effect in FeNi/Cu/FeMn and FeNi/Cr/FeMn trilayer systems

T. Mewes, B.F.P. Roos, S.O. Demokritov, and B. Hillebrands

Oscillatory interlayer exchange coupling between ferromagnetic (FM) layers is known since 1990 [1]. Direct exchange coupling between a FM and an antiferromagnetic (AF) layer at their mutual interface was under intensive investigation in the past decade, since it is believed to play an important role in the exchange bias effect [2–4]. A study of an oscillatory interlayer coupling in layered systems containing FM and AF layers, separated by a spacer, is the subject of this work. The experiments were performed on high quality $Fe_{20}Ni_{80}$/Cu/$Fe_{50}Mn_{50}$ and $Fe_{20}Ni_{80}$/Cr/$Fe_{50}Mn_{50}$ trilayer systems.

Still up to today the details of the microscopic origin of the exchange bias effect are under debate, especially the exact magnetic structure of the AF layer near the FM/AF-interface [5]. To discuss the effects reported in our work, it is sufficient to use a simple picture proposed by Mauri et al. [3] and Malozemoff [4]: while the FM layer is forced into a single domain state by an external field, the AF layer grown on top is formed *in nascendi* in a multidomain state, since the local interaction between the FM and the AF layer shifts locally the equilibrium between different, otherwise energetically degenerated AF domains. After completion of the growth the magnetic structure of the AF layer persists (if not too strong magnetic fields are applied) – and the hysteresis curve is shifted along the field axis by the so-called exchange bias field H_{eb}.

The above mechanism provides exchange biasing independently of whether the FM-AF interaction is ferromagnetic or antiferromagnetic. The sign of the interaction only defines which particular AF domain is energetically preferable for a given orientation of the magnetization of the FM layer [4, 5]. Let us classify these domains as (+)-domain for the case of the FM-type interaction and (–)-domain for the AF-type interaction. Usually, it is almost impossible to determine experimentally the sign of the FM/AF interface interaction [6].

The trilayers used for this study were grown in an UHV-evaporation system of $5 \cdot 10^{-10}$ mbar base pressure. All samples were grown onto chemically cleaned, thermally oxidized 5×10 mm^2 Si/SiO_2 substrates with 100 Å thick $Fe_{50}Mn_{50}$ or Cr buffer layers, and they were covered by a 20 Å thick Cr cap layer to prevent oxidation. To improve the sample quality the films were produced at T_{sub} = 200° C. Results obtained on the trilayer, where Cu and FeMn were deposited at room temperature (RT), will also be shown to demonstrate the sensitive dependence of the magnetic properties on the growth temperature. The better quality of the samples prepared at elevated temperature is not only attested by their pronounced oscillatory exchange bias field (see below), but also by their much smaller coercive field, H_c. The samples prepared at room temperature show a coercive field of H_c = 70 Oe, whereas those prepared at T_{sub} = 200° C show H_c = 40 Oe. Smaller coercive fields are a clear indication of a smaller concentration of defects.

The FeNi and FeMn layers were prepared with a constant thickness of 50 and 100 Å, respectively, while the Cu and the Cr spacer were grown in a wedge shape geometry (wedges 0–8 Å). The chemical analysis of the prepared films was performed *in situ* by a calibrated Auger electron spectrometer. An external magnetic field of 50 Oe was applied along the film plane of the samples during the entire preparation process.

The sample magnetization loops were studied at room temperature using a magneto-optical Kerr effect magnetometer. The values of H_{eb} for the samples without any nonmagnetic spacer are

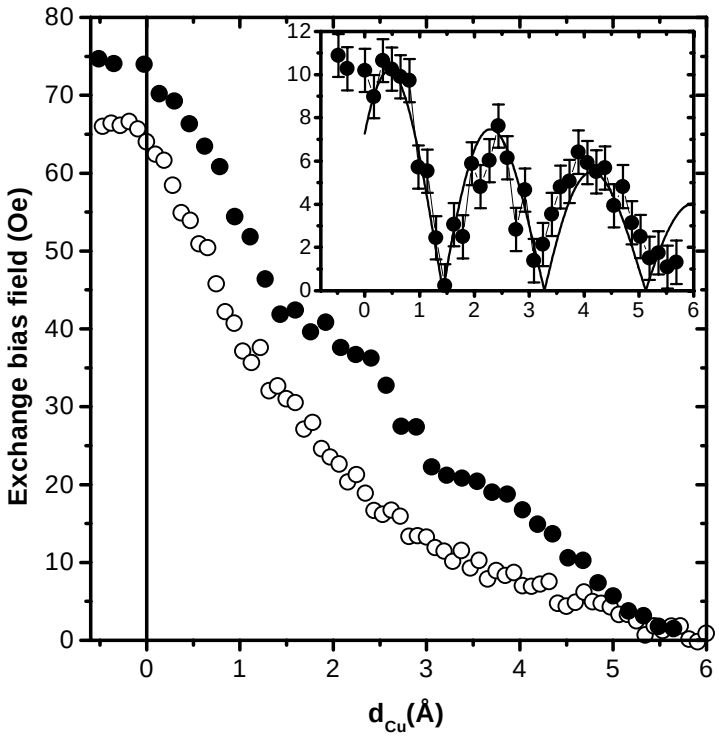

Fig. 1: Dependence of the exchange bias field H_{eb} in two trilayer systems of the composition FeNi/Cu/FeMn on the Cu spacer layer thickness d_{Cu}. ∘: sample prepared at T_{sub} = RT, ●: sample prepared at T_{sub} = 200° C. The vertical line at $d_{Cu} = 0$ indicates the begin of the Cu wedge, $d_{Cu} < 0$ corresponds to the double layer system FeNi/FeMn and is used as a reference. In the inset the oscillatory part of $H_{eb}(d_{Cu})$ after background subtraction and the data fit are shown.

about 80–100 Oe depending on the buffer material and the growth temperature. With increasing spacer thickness, *d*, the exchange bias field decays very fast. The value of the decay length depends on both the spacer material and the growth temperature, and it is in the range of 2–6 Å.

The best prepared systems show an oscillating contribution to $H_{eb}(d)$ in addition to the monotonic decay. This is shown in Fig. 1, where H_{eb} of two samples of the same composition of Si/SiO_2/100Å FeMn/50Å FeNi/d_{Cu} Cu /100Å FeMn/20Å Cr are plotted versus d_{Cu}. Open circles in Fig. 1 denote the sample prepared at T_{sub} = RT, and the full circles the sample prepared at T_{sub} = 200° C. Already the raw data show an oscillatory contribution on top of the monotonically decaying background. The oscillatory contribution is illustrated in detail in the inset of Fig. 1. Here only the oscillatory part of the dependence is presented together with the results of the fit to this part: $H_{eb} \propto \exp(-d/L)\left|\cos(2\pi d/\lambda - \phi)\right|$ with the decay length of the oscillation amplitude L = 6 Å, the oscillation wavelength $\lambda = 3.9$ Å, and the phase shift $\phi = 49°$.

In the trilayer system with a Cr spacer the exchange bias field shows a very similar behavior. This is illustrated in Fig. 2, where the $H_{eb}(d_{Cr})$ dependence, measured on the sample Si/SiO_2/100Å Cr/50Å FeNi/d_{Cr} Cr/100Å FeMn/20Å Cr is presented. The inset in Fig. 2 shows the oscillatory part of this dependence. Using the same fit function we obtain for the FeNi/Cr/FeMn system: L = 3.5 Å, $\lambda = 2.2$ Å and $\phi = 21°$.

This demonstrates that the found oscillatory exchange bias field is a general phenomenon, the oscillation periods being dependent on the spacer material. One possible cause for this lies in periodic variations of the interface morphology which can cause cosine-type oscillations of the magnetic anisotropy as observed for ultrathin Co films [7] analogously to the intensity variations in reflection high-energy electron diffraction. By assuming a monotonic dependence of the exchange bias field on the interface roughness, it is to expect that a periodic variation of the inter-

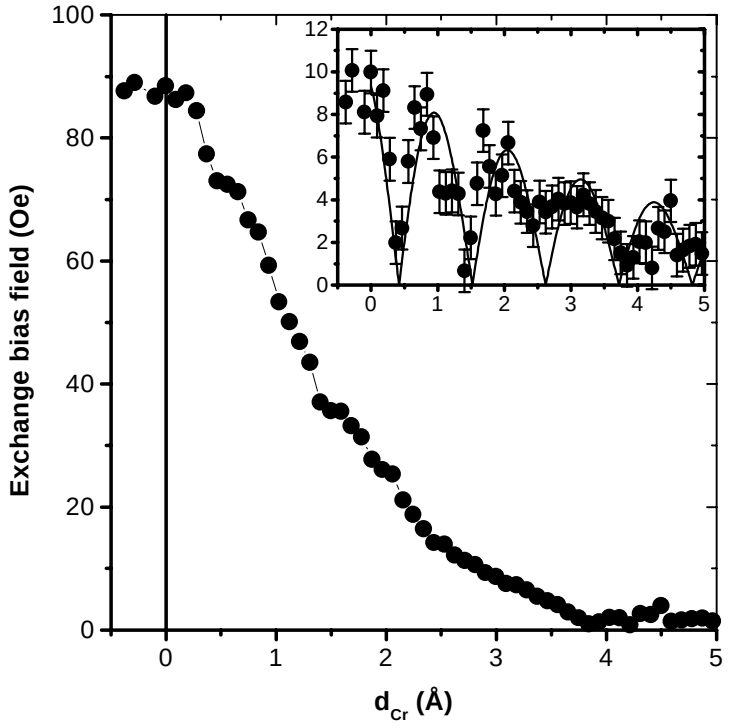

Fig. 2: Dependence of the exchange bias field H_{eb} in the trilayer system of the composition FeNi/Cr/FeMn on the Cr spacer layer thickness d_{Cr}. The vertical line at $d_{Cr} = 0$ indicates the begin of the of the Cr wedge, $d_{Cr} < 0$ corresponds to the double layer system FeNi/FeMn and is used as a reference. In the inset the oscillatory part of $H_{eb}(d_{Cr})$ after background subtraction and the data fit are shown.

face morphology will cause a cosine-type variation of H_{eb}. Experimentally the oscillating part of $H_{eb}(d)$ does not follow a simple cosine-function, as it is most clearly illustrated by its kink-type behavior near the zeros. Also note here that the investigated samples are polycrystalline.

To understand the above experimental findings, we propose to relate the oscillatory exchange bias field to the oscillatory interlayer coupling, well known in layered systems, containing two ferromagnetic layers and a nonmagnetic spacer [1, 3–5]. As described above, the exchange bias effect in a FM-AF layered system is caused by the FM-AF interface exchange interaction. If now a nonmagnetic spacer is placed between the FM and the AF layer, in analogy to the FM/spacer/FM system, the effective field induced by the FM layer in the AF layer will oscillate as a function of the spacer thickness, likely due to the quantum well effect for conduction electrons in the spacer [8]. There is no exchange biasing for those thicknesses where this oscillating function passes zero, since here the FM and AF layers do not interact. If the coupling strength is nonzero, the exchange bias caused by this indirect interaction is independent of the sign of the interaction. Thus, if the interaction depends on the spacer thickness as $\cos(2\pi d/\lambda)$, the exchange bias field should be a function of its absolute value, $H_{eb}\left(\left|\cos(2\pi d/\lambda)\right|\right)$ and an oscillatory dependence of H_{eb} on d with a period of $\lambda/2$ should be observed.

Since for both Cr and Cu spacers the interlayer coupling demonstrates short period oscillations with periods of about 2 ML (2.5 Å and 3.9 Å for Cr and Cu respectively) [3, 4], the exchange bias fields will then oscillate with periods of about 1 ML (1.25 Å and 1.85 Å correspondingly). These values, as it is seen in the insets of Fig. 1 and Fig. 2, are very close to the experimentally observed periodicities.

As it is seen in Figs. 1 and 2 the observed oscillatory dependence of $H_{eb}(d)$ has a relatively small amplitude, decreasing with the thickness, and it is superimposed on a monotonic decaying background function. To understand the origin of the reduced oscillation amplitude and of the

monotonic background, we need to consider more closely the influence of short- and long-range fluctuations of the spacer thickness (with the crossover between them being determined by the exchange correlation length in the AF layer, ξ) on the magnetic order of the FM/spacer/AF trilayer.

The influence of the short-range fluctuations can be understood as follows: These fluctuations cause fluctuations of the sign of the interaction between the FM and the AF layer across the spacer. However, in a similar way as it is in the fluctuation mechanism of the biquadratic coupling [9], small areas of a given type of the interaction cannot create different types of the AF domains. Only domains with lateral sizes larger than ξ will be created. Their types ((+) or (–)) are defined by the value of the interaction, $\bar{J}$, averaged over the domain size. $\bar{J}$, in turn, is determined by the average value of the spacer thickness, as well as by the amplitude of the fluctuation, δ. It is zero, if $\delta >> \Lambda$, where Λ is the period of the oscillatory interaction. In this case no exchange bias should be observed. If $\delta \leq \Lambda$, the average interaction is not zero. It changes periodically with the average value of the spacer thickness reflecting the oscillatory nature of the microscopic interaction. The decreasing amplitude of the oscillation is caused by an increasing function δ.

Long-range fluctuations of the spacer thickness have a different influence on the exchange bias effect. These fluctuations cause long-range fluctuations of $\bar{J}$ and H_{eb}. But, since in all cases the *same* orientation of $\vec{M}$ is stored in the AF layer, the exchange bias effect will not be washed out by the averaging process over the long-range fluctuations, even if their amplitude Δ is large compared to Λ. A macroscopic exchange bias field, although *monotonically* depending on the spacer thickness, should be observed. In the intermediate case $\Delta \approx \Lambda$ one obtains a superposition of the oscillatory and the monotonic behavior. We emphasize here, that Δ and δ characterize the fluctuations of the spacer thickness, but not the entire roughness of the interfaces.

A quantitative comparison between the morphology of the interfaces of the trilayers and the dependence $H_{eb}(d)$ is the topic of future studies.

Work supported by the Deutsche Forschungsgemeinschaft.

References

[1] S.S.P. Parkin, N. More, K.P. Roche, Phys. Rev. Lett. **64**, 2304 (1990).
[2] W.H. Mejklejohn, C.P. Bean, Phys. Rev. **102**, 1413 (1956).
[3] D. Mauri, H. Siegman, P.S. Bagus, E. Kay, J. Appl. Phys. **62**, 3047 (1987).
[4] A.P. Malozemoff, J. Appl. Phys. **63**, 3874 (1988).
[5] T.J. Morgan, J. Nogues, D. Lederman, I.K. Schuller, J. Appl. Phys. **72**, 617 (1998).
[6] J. Nogues, D. Lederman, T.J. Morgan, I.K. Schuller, Phys. Rev. Lett. **76**, 4524 (1996).
[7] W. Weber, C.H. Back, A. Bischof, Ch. Würsch, R. Allenspach, Phys. Rev. Lett. **76**, 1940 (1996).
[8] P. Bruno, Phys. Rev. B. 52, 411 (1995); M.D. Stiles, J. Appl. Phys. **79**, 5805 (1996).
[9] J.C. Slonczewski, Phys. Rev. Lett. **67**, 3172 (1991).

6.18 Influence of ion irradiation on the exchange bias effect

T. Mewes, R. Lopusnik, J. Fassbender, and B. Hillebrands[1]

Exchange bias systems, comprising a ferromagnetic (F) layer exchange coupled to an antiferromagnetic (AF) layer, are characterized by a shift in the hysteresis loop along the field axis by the so-called exchange bias field, H_{ex}, accompanied by an increase in the coercive field, H_c. Due to the interfacial character of the exchange bias effect, any modifications of the atomic structure at the interface are expected to result in changes in H_{eb} and H_c. We present results of ion irradiated FeMn/FeNi exchange bias systems, which show, that both H_{eb} and H_c can be tailored by the irradiation process. Recently it has been shown that ion irradiation of Co/Pt multilayers leads to a change in the easy direction of magnetization from perpendicular to in-plane with respect to the film plane due to a small amount of atoms displaced at the interface by the irradiation process [1,2].

We find, that the value of the exchange bias field can be modified in a controlled manner depending on the dose and the energy of the ions. A suppression of the exchange bias field to a desired value is achievable [3].

In order to test the influence of ion irradiation we chose the well known FeNi/FeMn exchange bias system. All samples were prepared in a UHV-system with a base pressure of $5 \cdot 10^{-10}$ mbar. Onto a thermally oxidized Si substrate a 20 nm thick FeMn buffer layer was deposited. Subsequently a sandwich of a 5 nm FeNi (F) and a 10 nm FeMn (AF) layer was grown on top. Finally a 2 nm Cr layer was deposited to prevent the samples from oxidation. All layers but the FeNi layer (200°C) were grown at room temperature in an applied magnetic field of 50 Oe. After the preparation the magnetic properties were controlled *ex situ* by spatially resolved longitudinal magneto-optical Kerr-effect (MOKE) measurements. The exchange bias field was found to be homogeneous across each sample.

After the initial magnetic characterization the samples were inserted into an ion optical bench to perform the ion irradiation. Helium ions were accelerated by 35 kV. Different ion doses on the samples were realized by adjusting the beam current (0.01 – 2 µA), depending on the accelerat-

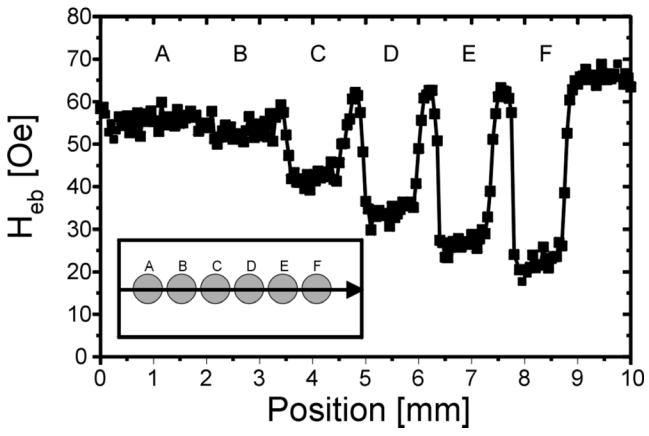

Fig. 1: Measured exchange bias fields plotted as a function of the position on the sample. The acceleration voltage is 10 kV and the doses are [ions/cm^2]: A: $1.4 \cdot 10^{14}$, B: $4.7 \cdot 10^{14}$, C: $9.4 \cdot 10^{14}$, D: $1.2 \cdot 10^{15}$, E: $1.9 \cdot 10^{15}$, F: $2.4 \cdot 10^{15}$. The inset shows a schematic sketch of the sample with the lateral scan marked. Irradiated areas are shaded.

[1] In collaboration with M. Jung, D. Engel, A. Ehresmann, and H. Schmoranzer, Fachbereich Physik, Universität Kaiserslautern.

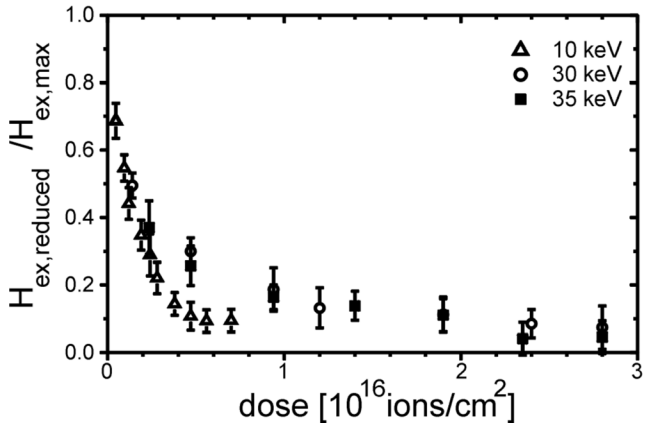

Fig. 2: Normalized exchange bias field as a function of ion dose for different acceleration voltages varying between 10 – 35 kV.

ing voltage, and varying the irradiation time (3 s – 300 s) correspondingly, covering the range from 10^{12} ions/cm^2 to 10^{17} ions/cm^2. Different ion doses at a fixed acceleration voltage are applied to one single sample by irradiating different areas of the sample.

In Fig. 1 we present a lateral scan across the sample through the centers of the irradiated areas (see inset). The exchange bias field was extracted from the hysteresis loops and plotted as a function of the position on the sample. All non-irradiated areas exhibited a value of $H_{eb} \approx 60$ Oe of the exchange bias field whereas for the irradiated areas the exchange bias field was found to be reduced. The values of the exchange bias fields were extracted by averaging the field values within the plateaus of the irradiated areas.

In Fig. 2 we have plotted the normalized exchange bias field as a function of the ion dose. For all acceleration voltages of the He ions we find a pronounced decrease of the exchange bias field in the dose regime between 10^{14} and 10^{17} ions/cm^2. For lower doses the exchange bias field has the same value as for non-irradiated areas. The main difference between irradiation with low (10 kV) and high (35 kV) acceleration voltage is the different slope of the curves, i.e., for an acceleration voltage of 10 kV lower doses are required for suppressing the exchange bias field by the same amount than for 35 kV. This becomes clear by considering the different penetration depths and the energy loss mechanism of the ions for different energies. For 35 kV He ions the average penetration depth is 350 nm, much larger than the total film thickness of the exchange bias system. By traversing the AF and F layers, the ions loose their kinetic energy mostly via electron interactions [4]. Only at the end of the ion trajectory the dominant interaction is via collisions with nuclei leading to a destruction of the crystallographic structure. Thus, at the interface between the F and AF layers, the density of displaced atoms is low. For lower acceleration voltages the penetration depth is lower, the interaction regime is located closer to the surface and thus the density of displaced atoms is increased. The reduction of the exchange bias field can thus be attributed to an increased interface roughness leading to a decrease of H_{eb}.

References

[1] C. Chappert, H. Bernas, J. Ferre, V. Kottler, J.-P. Jamet, Y. Chen, E. Cambril, T. Devolder, F. Rousseaux, V. Mathet, H. Launois, Science **280**, 1919 (1998).

[2] T. Devolder, C. Chappert, Y. Chen, E. Cambril, H. Bernas, J.P. Jamet, J. Ferre, Appl. Phys. Lett. **74**, 3383 (1999).

[3] T. Mewes, R. Lopusnik, J. Fassbender, B. Hillebrands, M. Jung, D. Engel, A. Ehresmann, H. Schmoranzer, submitted to Appl. Phys. Lett.

[4] SRIM 2000 code, J.F. Ziegler, J.P. Biersack, U. Littmark, *The Stopping and Range of Ions in Solids*, Pergamon, New York, Oxford (1985).

E. Elastic Properties

6.19 Surface acoustic waves in two-phase boron nitride bilayer films

T. Wittkowski, J. Jorzick, K. Jung, and B. Hillebrands[1]

Boron nitride in its cubic modification (c-BN) possesses a hardness exceeded only by that of diamond. Due to a higher thermal stability and a lower reactivity with ferrous materials c-BN is well suited as a wear resistant coating material. At ambient conditions the cubic modification of the BN system is the thermodynamically stable one, as opposite to the carbon system, where graphite is the thermodynamically stable modification. The deposition conditions to nucleate c-BN, however, are far away from ambient conditions. In all deposition methods known so far the phase transition from hexagonal boron nitride (h-BN) to c-BN is induced by an internal stress which must exceed a critical value in the growing film. As a consequence the deposition process leads to bilayer films with a h-BN layer at the interface to the substrate and a c-BN layer on top.

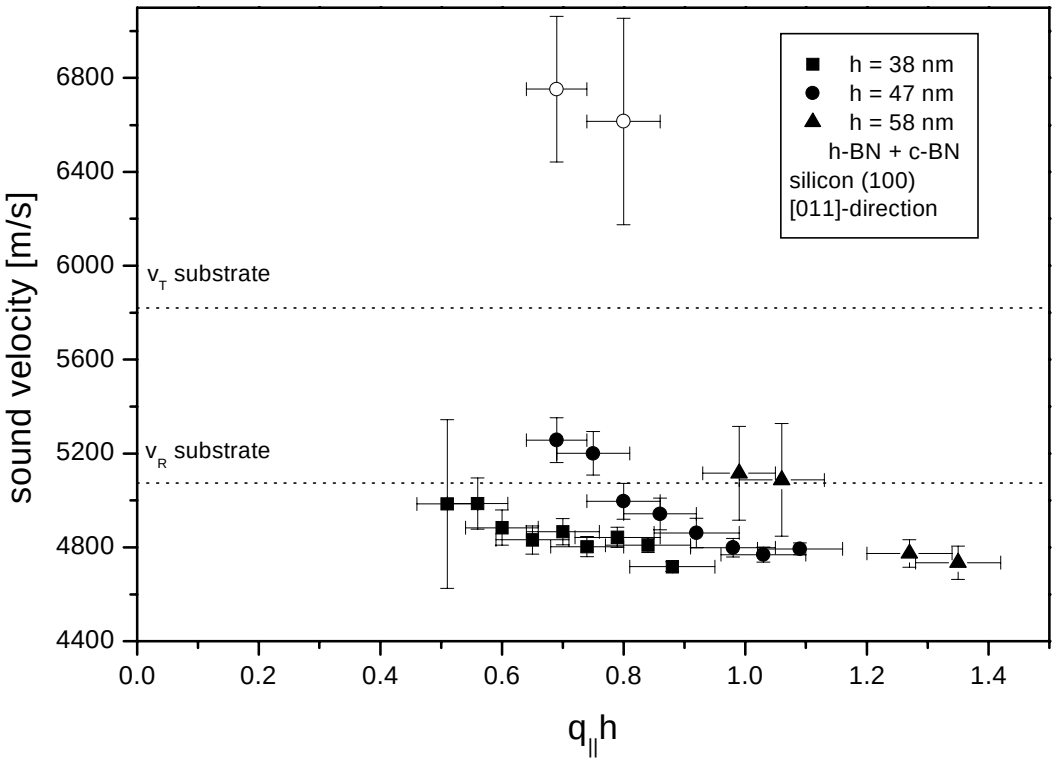

Fig. 1: Dispersion of the sound velocity of three samples measured with BLS. The excitation of the Rayleigh mode was detected for all films. In the 47 nm thick film a transversal mode above the velocity threshold of the substrate, v_T, shows up as a resonance (Lamb mode). From the dispersion of the Rayleigh modes it is seen that for different films the data points do not merge. For this reason a layered film structure must be required. The sound velocity increases with film thickness due to the influence of the fast upper c-BN layer.

[1] In collaboration with F. Richter, TU Chemnitz, A. Lunk, Universität Stuttgart, A. Schumacher and H. Oechsner, Universität Kaiserslautern, and F. Nizzoli, Universitá di Ferrara, Italien.

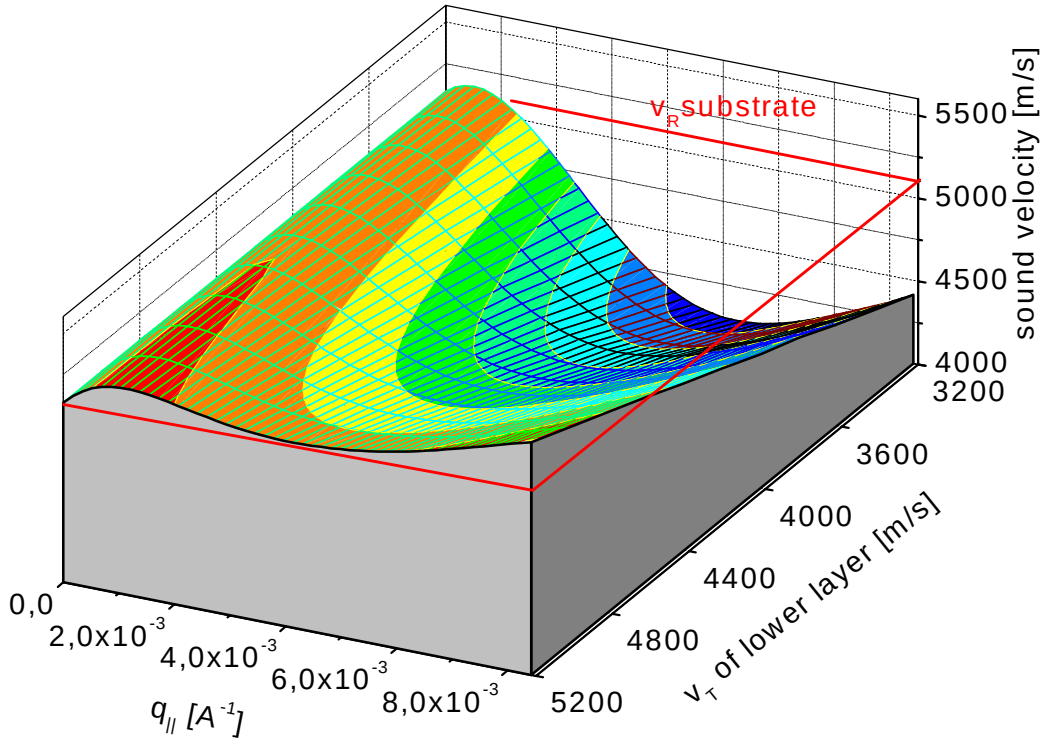

Fig. 2: Calculated sound velocities of the Rayleigh mode vs. parallel phonon wavevector, $q_{\parallel}$, and transversal sound velocity of the lower layer, v_T^L. The horizontal line indicates the sound velocity of the substrate Rayleigh mode, v_R.

Parameters:	lower layer (isotropic):	upper layer (isotropic):
	thickness 30 nm, density 2.15 g/cm^3 c_{11} = 120 GPa v_L^L = 7471 m/s	thickness 17 nm, density 3.3 g/cm^3 c_{11} = 600 GPa c_{12} = 150 GPa v_T^U = 8257 m/s v_L^U = 13484 m/s

Depending on the deposition conditions the thickness of the h-BN layer may vary between a few nanometers and a few ten nanometers. If the nucleation conditions for c-BN are not fulfilled the film will consist of pure h-BN.

In 1999 elastic properties of various boron nitride samples have been studied by our group using the Brillouin light scattering (BLS) technique. Except for the h-BN films produced in our own magnetron sputtering device, thin h-BN/c-BN bilayer films and thick c-BN films have been investigated in cooperation with several research groups. Prof. F. Richter and his coworkers (TU Chemnitz) provided us with magnetron sputtered h-BN films grown at experimental conditions close to the c-BN transition. Thick c-BN films were grown in the group of Prof. A. Lunk (Universität Stuttgart) with a hollow cathode arc evaporation device. In this report we present measurements on thin h-BN/c-BN bilayer films provided by A. Schumacher and Prof. H. Oechsner, Universität Kaiserslautern. Three samples of different thicknesses were examined. The films were grown in a PECVD process with an ECWR-plasma and borane-ammonia (BH_3NH_3) as precursor [2]. From IR spectra of the three samples grown under identical conditions, it could be concluded that the films consist of a 30 nm thick h-BN layer at the substrate and a covering c-BN

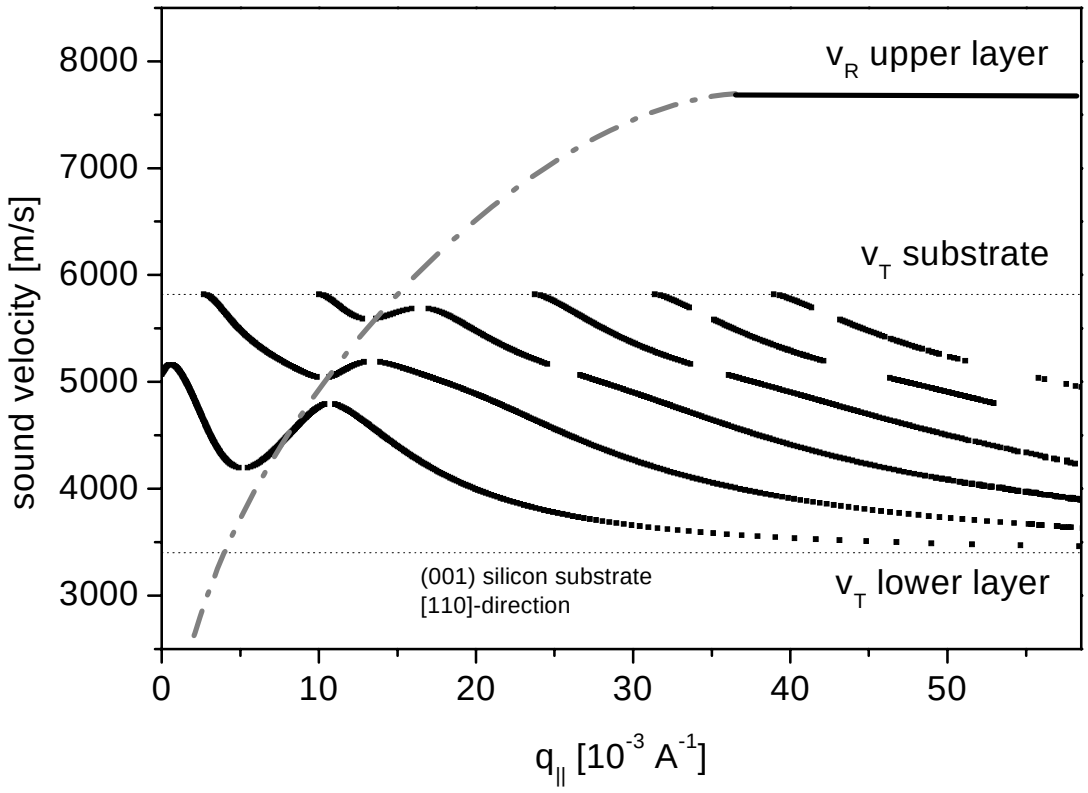

Fig. 3: Calculated sound velocities of all sagittal modes in a large wavevector range. Parameters are as in figure 2, the transversal sound velocity of the lower layer is 3410 m/s. For short wavelength the constant velocity of the upper film Rayleigh mode is found to be 7700 m/s.

layer whose thickness was 8 nm, 17 nm and 28 nm, respectively. Probably there exists a few nanometer thick interface with coexisting hexagonal and cubic phases.

In these films thermally excited surface acoustic waves are investigated at room temperature by BLS. Experiments were performed in backscattering geometry and *p-p* polarization with 514.5 nm light [1]. A Fabry-Pérot interferometer of the Sandercock type was used for the detection of the inelastically scattered light [3]. Figure 1 shows the dispersion of the phase velocity of the Rayleigh mode. Despite the small variation in film thickness the dispersion curves of all samples are clearly distinguished by their velocities. The data points of different samples do not merge, which is a proof for a layered film structure. The sound velocity increases with film thickness due to the higher sound velocity in the c-BN layer. Surprising at first sight is a phase velocity of the Rayleigh mode (most distinct for the 47 nm thick film) higher than the velocity of the Rayleigh wave of the substrate, v_R. This is a clear indication for an oscillatory behavior of the dispersion in this type of layered films.

Figure 2 shows a simulation of the sound velocity of the Rayleigh wave in a system of type "fast upper layer – slow lower layer – medium substrate". Both layers are assumed to be elastically isotropic. The wave propagates in the [011]-direction on a (100) surface of the silicon substrate. The assumption of isotropic layers is sufficient to generate an oscillating dispersion curve. As an example the transverse sound velocity of the lower (slow) layer is varied. For the used set of parameters and the plotted wavevector range it depends on this velocity whether the Rayleigh velocity decreases below the Rayleigh velocity of the substrate or not. If one regards an enlarged

wavevector range additional transverse guided modes appear. As is seen in Fig. 3 for large $q_{\parallel}$ the velocity of these modes converges to the lowest sagittally polarized bulk velocity of the slow layer. The Rayleigh mode of the upper layer possesses a constant velocity if the phonon wavevector is larger than about $3 \cdot 10^{-2}$ Å^{-1}. Below this value the mode leaks energy into the underlying layer and into the substrate and is strongly attenuated, especially directly above the velocity threshold [4, 5]. Below the velocity threshold the dash-dotted curve indicates a fundamental change of the propagation properties of the discrete modes. A calculation of the displacement field profiles in the sagittal plane shows that on the left hand side of the curve the vertical displacement is mainly localized in the film and with increasing wavevector the displacement is almost exclusively localized in the upper layer. On the right hand side of the curve the vertical displacement is localized almost completely in the lower layer. This demonstrates that for small phonon wavevectors, respectively thin films, the complex dispersion behavior of a bilayer film of this type includes enough information to determine several independent elastic constants of both layers.

However, for the analyzed films only one mode in the discrete part of the spectrum is detected due to the small film thickness and the limited experimentally accessible wavevector range. In the investigated films the h-BN layer and probably the c-BN layer is elastically anisotropic [6]. This would require a description with four independent elastic constants for each layer. Despite of this fact an estimation of the shear modulus of the c-BN layer under the assumption of isotropic layers can be made. This yields c_{44} = 239 GPa ± 20%, a value which is comparable to results on thick c-BN films [6].

Work supported by the Deutsche Forschungsgemeinschaft.

References

[1] T. Wittkowski, J. Jorzick, K. Jung, B. Hillebrands, Thin Solid Films **353**, 137 (1999).
[2] A. Schumacher and H. Oechsner, **CIP ´99**, 12th International Colloquium on Plasma Processes, Antibes, France, p. 106.
[3] R. Mock, B. Hillebrands, J.R. Sandercock, J. Phys. E **20**, 656 (1987); B. Hillebrands, Rev. Sci. Instr. **70**, 1589 (1999).
[4] O. Lefeuvre, P. Zinin, and G.A.D. Briggs, A. Every, Appl. Phys. Lett, **72**, 856 (1998).
[5] G. Carlotti, D. Fioretto, L. Giovannini, L. Palmieri, G. Socino, L. Verdini and E. Verona, 1994 Ultrasonics Symposium, p. 457.
[6] T. Wittkowski, P. Cortina, J. Jorzick, K. Jung, B. Hillebrands, Diam. Rel. Mat., to be published.

F. Instrumental

6.20 A commercially available, computer controlled, multipass tandem Fabry-Pérot spectrometer

J. Jorzick and B. Hillebrands[1]

Since August of this year a second tandem Fabry-Pérot type Brillouin light scattering spectrometer of the Sandercock design is installed in our lab. Sandercock recently made a major revision in the design of the control box. Apart from additional features like support for a shutter in front of the photon detector and a power supply for the photon detector, the control box now contains an interface to a PC to use the Sandercock system together with the software package TFPDAS3 developed over the last 10 years in our lab.

The multipass tandem Fabry-Pérot spectrometer designed by J.R. Sandercock 20 years ago has been proven to be a very successful instrument to study the weak light signals scattered inelastically from surface and thin-film phonons and spin wave excitations. The easy use and the large versatility has not been surpassed by any concurring design, and it is now widely used by many

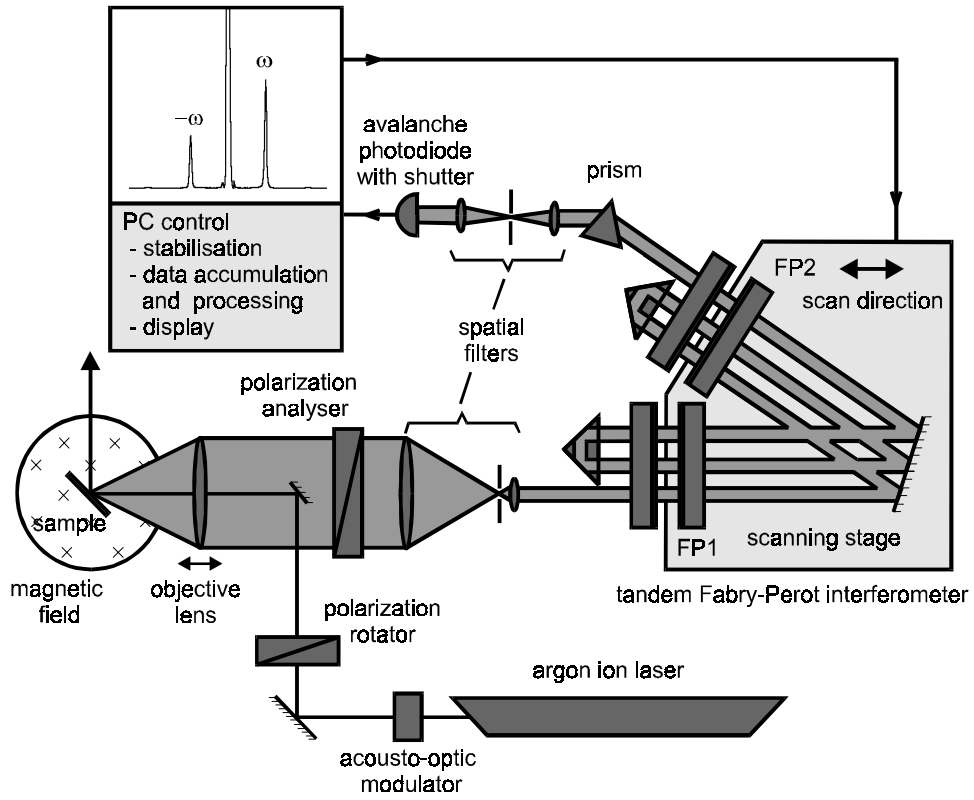

Fig. 1: Schematic setup of the spectrometer. The optical beam pass is shown for the (3+3) pass geometry. Not shown is the slide with glass blocks and half-reflecting mirrors for switching into the so-called reflection mode for alignment of the system, for details see [1]. Also not shown is the system for positioning the sample.

[1] In collaboration with Dr. J.R. Sandercock, JRS Scientific Instruments, Lindenmoosstraße 10, 8910 Affolten a.A., Switzerland.

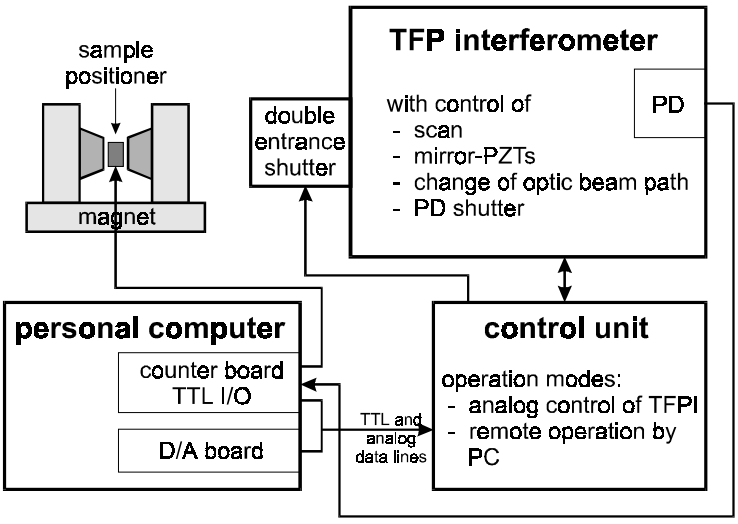

Fig. 2: Functional layout of the digitally controlled interferometer. Shown are the connections between the personal computer, the tandem Fabry-Pérot interferometer and the control unit. PD: photon detector.

research groups in the world. Figure 1 shows the schematic setup of a multipass tandem spectrometer.

Multipass-tandem Fabry-Pérot interferometry allows the unambiguous detection of inelastic excitations. The contrast of a Sandercock-type interferometer exceeds 10^{10}, only limited by the dark count rate of the photon detection system, and the resolution is typically less than a few percent of the free spectral range. To achieve this performance, an active stabilization of the etalon mirrors using a multidimensional feedback mechanism is necessary. This is solved in the original design by Sandercock by analog circuitry.

Conceptionally, using a PC, a more flexible control of an experiment can be realized. We have developed a computer control for the Sandercock instrument [1], which comprises a so-called counter board, developed in our lab, as a plug-in board for the PC performing the photon counting and handling digital input and output, a D/A board for generating the voltages applied to PZTs controlling the mirror spacings and tilts, and the software package TFPDAS3. Recently we have adapted this system to the new Sandercock control unit. It has the following features. It contains i) full support for data acquisition and display, ii) it maintains stabilization during measurements, iii) it contains routines to align the system automatically, and iv) a control of peripheral devices is implemented. In addition, v), a script language is implemented to perform a programmed sequence of measurements like a series of spectra as a function of sample position, angle of light incidence, or, in case of magnetic excitations, of the external magnetic field without the need of an operator during the course of the sequence. vi) Build-in fitting routines allow one to analyze the spectra, like fitting the peak positions, and to generate data in a format suitable for graphic program packages.

Due to the intrinsic versatility of a software solution the every-day stability of the system is superior to existing hardware solutions with the additional advantage of easy control and handling of all signal and data flow. Due to the simple interface to the user, the entire Brillouin light scattering setup can be operated by any researcher after only a few days training in the operation.

Figure 2 shows the functional layout of a Sandercock tandem Fabry-Pérot interferometer interfaced to the PC-based control. The counting board and a D/A converter board are added to the PC. The software takes over full control of the interferometer. It changes the optical beam path between the configurations for data accumulation, as shown in Fig. 1, and for alignment of the system (not shown in Fig. 1). Also by software a double shutter system, designed by Sandercock, is controlled to change between the light from the sample, containing the inelastic light contribution, and light from a reference beam used for stabilization. Alternatively, an acousto-optic modulator can be used for adjusting the light level.

The Sandercock interferometer together with TFPDAS3 is now a turn-key instrument for investigations of weak inelastic light scattering cross sections. It can be easily expanded towards new applications. We have added a full remote control for using the instrument in the space- and time-resolving BLS-microwave experiments as described in Sects. 6.1–3. Currently plans exist to add a confocal stage for high resolution applications.

Work supported by the Stiftung für Innovation in Rheinland Pfalz.

Reference

[1] B. Hillebrands, Rev. Sci. Instr. **70**, 1589 (1999).

Appendix: Sensitivity of photon detectors

Often the problem arises to compare the performance of different photon detectors. In the following $n_{\text{inelastic}}$ is the number of inelastically scattered photons per second and energy interval, n_{dark} is the dark count rate in units of counts per second, f_{QE} is the quantum efficiency of the detector and T is the duration of the measurement.

We compare the performance of

A) a standard photomultiplier tube, f_{QE} = 10%, n_{dark} = 2 counts/s,

B) a high quality photomultiplier tube, f_{QE} = 10%, n_{dark} = 0,1 counts/s,

C) the "first generation" EG&G solid state photon detector, f_{QE} = 30%, n_{dark} = 3 counts/s (which EG&G has now replaced by detector D),

D) the "second generation" EG&G solid state photon detector, f_{QE} = 60%, n_{dark} = 15 counts/s.

The signal at the detector is $n_{\text{inelastic}} \cdot f_{\text{QE}} \cdot T$ on top of a background level of $n_{\text{dark}} \cdot T$. The noise σ_{noise} (statistical noise only) is given by $\sigma_{\text{noise}} = \sqrt{\left(n_{\text{inelastic}} \cdot f_{\text{QE}} + n_{\text{dark}}\right) \cdot T}$.

We now ask for the duration T of a measurement needed to achieve a spectrum in which the noise is at least equal to the recorded signal, i.e., $\sigma_{\text{noise}} \leq n_{\text{inelastic}} \cdot f_{\text{QE}} \cdot T$, which is a minimum condition in cases where the signal is comparable to dark count contributions. After simple algebra we find:

$$T \geq \frac{1}{n_{\text{inelastic}} f_{\text{QE}}} + \frac{n_{\text{dark}}}{n_{\text{inelastic}}^2 f_{\text{QE}}^2}$$

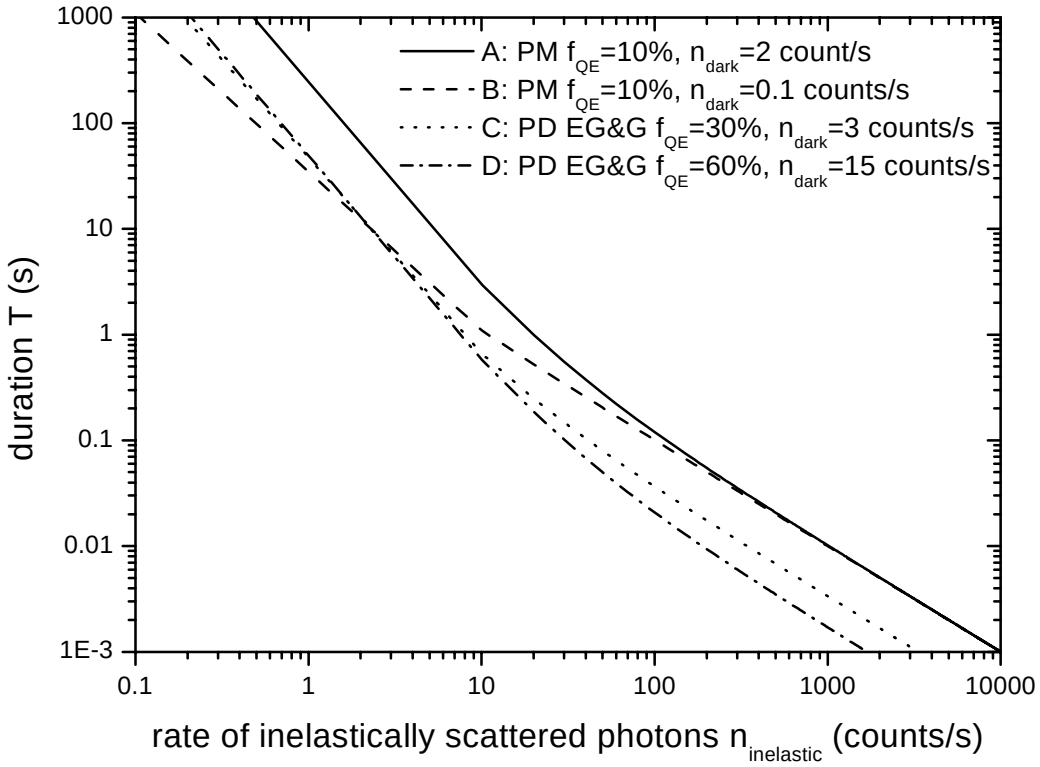

Fig. 3: Time T needed in a measurement to obtain a spectrum as specified in the text as a function of the rate $n_{\text{inelastic}}$ of inelastically scattered photons. Note the logarithmic scales of T and $n_{\text{inelastic}}$.

For strong signals the duration of measurement is inversely proportional to the quantum efficiency of the detector, and for small signals it scales with the dark count rate and the inverse quantum efficiency squared. Figure 3 shows a plot of T as a function of the rate $n_{\text{inelastic}}$ of the inelastically scattered photons for the four photon detectors A...D. For signals larger than the weak value of 5 count/s the detector D is best suited. Its large dark count rate is overcompensated by the large quantum efficiency.

6.21 A time resolved magneto-optical Kerr effect magnetometer

M. Bauer, R. Lopusnik, J. Fassbender, and B. Hillebrands

Magneto-optical Kerr effect (MOKE) magnetometry has evolved to one of the most favorite methods for investigations of the magnetization behavior of ultrathin magnetic films. Selectivity (substrate effect is mostly avoided because of limited penetration depth in metals), potential of local measurement, good sensitivity (a few atomic magnetic layers) and rapid response are powerful advantages, which can be used for the direct observation of magnetization and domain wall motion processes in micron-size regions. The measured effect is usually considered to have a linear relation to the projection of magnetization onto a reference direction defined by the MOKE geometry.

Recently time resolved experiments with sub-nanosecond resolution have been developed by several groups [1–4]. The aim is to investigate the dynamic properties of the magnetization reversal process. We have developed a time resolved magneto-optical Kerr effect magnetometer utilizing a stroboscopic technique. Time resolution is realized by the application of magnetic field pulses to the sample, and by subsequently testing the magnetization state by means of the longitudinal magneto-optic Kerr effect using a time delayed, pulsed ps-IR diode laser. Figure 1 shows the experimental setup.

A personal computer (PC) is connected via a general purpose interface bus (GPIB) to an electronic delay generator with two output channels. Channel B is used to provide a current pulse in the microstrip line on the printed circuit board (PCB) generating a magnetic field pulse. The sample (a lutetium bismuth iron garnet (BIG) film on a gadolinium gallium garnet (GGG) substrate) is located directly on top of the microstrip line. Channel A provides a time delayed pulse

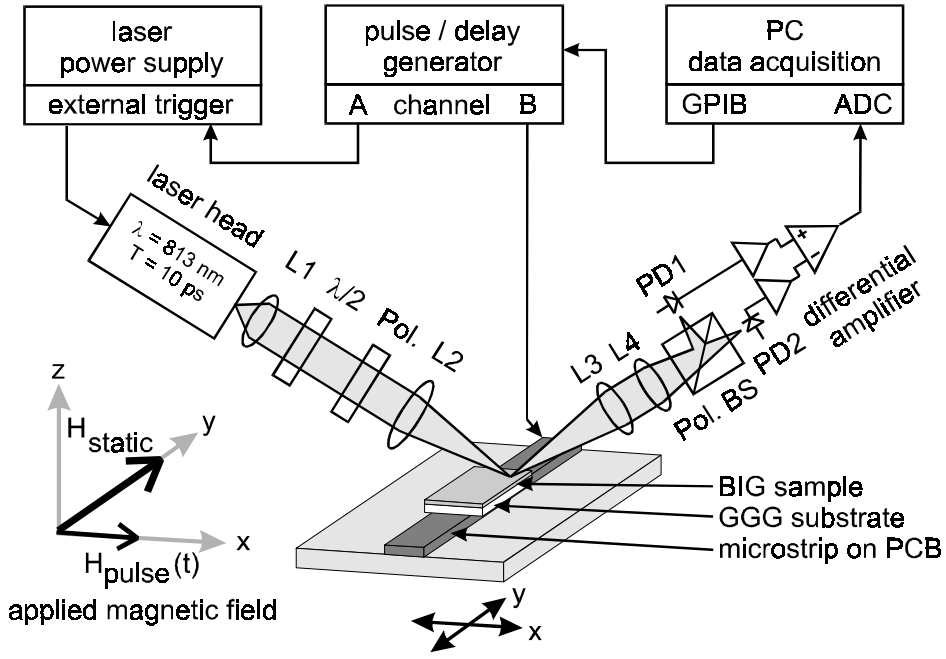

Fig. 1: Experimental setup of the time resolved magneto-optical Kerr effect magnetometer. For details see text.

used to trigger the pulsed ps-IR diode laser. The laser operates at a wavelength of $\lambda = 813$ nm and with a repetition rate from single shot up to 1 MHz (pulse duration of 10 ps, energy of 10 pJ/pulse). The delay time between the outputs of channels B and A is varied and thus the delay between the magnetic field pulse and the time of the test of the magnetization state. Lenses (L_1–L_4) are used for beam collimation and focusing, and a retardation plate ($\lambda/2$) is used to maximize the light transmission through the polarizer (Pol.). *s*-polarized light is reflected from the sample onto a polarizing beam splitter (Pol. BS). The two orthogonal polarization components are detected by photo diodes (PD1, PD2). Their signals are amplified by a differential amplifier and digitized by an analog-to-digital converter (ADC). To adjust the signal levels of both photo diodes to the same value and to increase the dynamic range of the differential amplifiers, the whole detection system is rotated by a stepper motor about the axis of the incident light. In order to investigate the spatial distribution of the magnetization dynamics, the sample is mounted on a (*x*,*y*)-scanning stage. The overall time resolution is 100 ps, the lateral resolution is 100 µm.

First experimental results obtained with this setup are presented in Sect. 6.11.

Work supported by Siemens AG, BMBF and the European Union (TMR project "Dynaspin").

References

[1] W.K. Hiebert, A. Stankiewicz, M.R. Freeman, Phys. Rev. Lett. **79**, 1134 (1997);
M.R. Freeman, W.K. Hiebert, A. Stankiewicz, J. Appl. Phys. **83**, 6217 (1998).
[2] R.H. Koch, J.G. Deak, D.W. Abraham, P.L. Touilloud, R.A. Altman, Yu Lu, W.J. Gallagher, Phys. Rev. Lett. **81**, 4512 (1998).
[3] T.J. Silva, C.S. Lee, T.M. Crawford, C.T. Rogers, J. Appl. Phys. **85**, 7849 (1999).
[4] C.H. Back, J. Heidmann, J. McCord, IEEE Trans. Magn. **35**, 637 (1999).

G. Transfer of Technology

6.22 Center for Technology Transfer “Hard and wear resistant coatings” (Institute of Thin Film Technology)

C. Osthöver, K. Jung, and B. Hillebrands

The Center for Technology Transfer "Hartstoff- und Verschleißschutzschichten" ("Hard and wear resistant coatings"), also called the "Institut für Dünnschichttechnologie" (Institute of Thin Film Technology), serves for the transfer of thin film know-how into small and medium size companies, preferably located in the state of Rheinland-Pfalz. It is part of the University of Kaiserslautern, and it was founded by H. Ehrhardt and K. Jung in 1993. Since 1997 the Center is located in the Technologiezentrum Oberfläche (TZO, "Competence Center for Surface Technology") in Rheinbreitbach at the northern boarder of the state of Rheinland-Pfalz.

Rising demands on the properties of construction components and tools make the use of modern coating procedures indispensable in many industrial fields. One of the key issues is the development and application of highly strain- and wear-resistant surfaces. Today, modern thin-film technology can combine extreme surface properties of thin layers with almost any volume material and thus guaranteeing a particularly high product upgrading. In this way, contrasting requirements, such as high tenacity and simultaneously a large degree of hardness can be combined through surface coating with suitable hard material layers. It is the aim of the Center to develop such high-tech films and to transfer the process know-how into industry. The institute also searches for new applications for high tech films. For example, a diffusion barrier of SiC for use in solar cells has been developed. Another example is a deposition of a composite material as a wear resistant layer on pumps used in dental industry.

Besides the development of product-specific coatings the institute performs the following tasks:

- analysis of wear and tear processes
- test and series coating
- support during introduction of coating technology into production
- consulting on tribological problems and on possibilities to use hard coatings
- lectures and seminars on coating problems.

The goal of these seminars is to make the industry familiar with coating technology and to support companies with the knowledge of the institute. In 1999 the institute had started a cooperation with the HWK (Handwerkskammer) in Koblenz to intensify the contact to industry. The HWK Koblenz is an organization of trade companies with 17,200 partners in the northern part of Rheinland-Pfalz. As a first step a seminar about “Advantages of surface technology” was organized.

After the initial phase of establishing the new Center two main projects have been started in close collaboration with industrial partners:

1. Biomedical thin films, described in Sect. 6.23
2. Coating of precision tools and machine parts with wear-resistant and low friction amorphous carbon thin films at ambient temperatures

In the second project the aim is to develop very hard carbon films for use in technical applications. For this purpose a coating process involving ta-C films has been developed. They consist of a highly tetrahedral form of amorphous carbon, referred to as ta-C, containing up to 90% sp^3 bonds. The hardness of these films is approximately 7.000 HV, the friction coefficient is as low as 0.03, comparable to an oil lubricated steel on steel combination, and the films are chemically inert.

Due to the near to diamond-like properties and the low friction coefficient ta-C films have a very good potential in industrial applications. Contrary to other deposition methods ta-C films can be prepared at room temperature. We use a plasma beam deposition process developed at the University of Kaiserslautern [1]. The plasma beam source (CCR Beschichtungstechnologie GmbH, Rheinbreitbach) is based on the electron cyclotron wave resonance (ECWR) effect. The process gas is C_2H_2 at a pressure of about $5 \cdot 10^{-4}$ mbar, and the ion energy is about 180 eV. A key issue is to make films of large enough thickness (typically 1 µm) with internal stresses small enough to avoid delamination. This is achieved by doping the films with, e.g., boron [2].

Doping of 2-3 % boron, measured with elastic recoil detection analysis (ERDA), reduces the inner stress down to 2 GPa. This is a value normally used in hard coatings like TiN. The thickness of the film is 1.7 µm and its hardness is 4.000 GPa. These values fulfill the requirements for many industrial applications.

Further experiments are in progress to understand more deeply the processes of stress reduction. A surprising result is that the use of boron dopants reduces the stress while simultaneously keeping the hardness unaffected. Adhesion experiments for films deposited onto steel surfaces are currently underway.

Work supported by the Stiftung für Innovation in Rheinland Pfalz.

References

[1] M. Weiler, S. Sattel, T. Giessen, K. Jung, V.S. Veerasamy, J. Robertson, Phys. Rev. B **53**, 1594 (1996).
[2] M. Chowalla, Y. Yin, G.A.J. Amaratunga, D.R. McKenzie, Th. Frauenheim, Diamond and Related Materials.

6.23 A new procedure to manufacture radioisotope stents

H. Busch, U. Grabowy

Preface (*B. Hillebrands*)**:** The state of Rheinland-Pfalz has started a program "Institutsgestützte Unternehmensgründung" (IUG, "Founding companies by assistance through research institutions"). It is aimed to help young scientists to leave their research environments, typically a department or an institute at a university or a state-operated research institute, and to found their own company. The idea is to convert technological know-how into products and to create new jobs. The program pays half the salary for an initial period of half a year while the participants still work at their home institutions, to prepare the foundation of the new company. In a second step, after the foundation, loans are provided. During the entire process the participants of the program are assisted by the Business Innovation Center, Kaiserslautern, an state-operated institute specialized in consultance and support for new high-tech companies. Dr. H. Busch and Dr. U. Grabowy are presently employed part time at the Center for Technology Transfer, and they use the facilities of the Center to prepare the foundation of their company. They report their concept in the following.

Today in all industrial countries heart disease is responsible for about 30% of all actual deaths. In the case of cardiac infarction a part of the heart muscle dies, because it is not sufficiently provided by blood and oxygen. The origin of this is the stricture of coronary arteries (arteriosclerosis). Fatty constituent materials, like cholesterin and lipoids, as well as lime salts are deposited on the walls of the vessel and in consequence it becomes harder and thicker. The building of a thrombosis is promoted causing a closure of the vessel.

The state of the art technique to open the tight areas is the so-called percutaneous transluminal coronary angioplasty (PTCA). Under use of a catheter a balloon is placed at the stricture (stenosis), and with pressure of a few bar the stenosis is opened. Frequently a new stenosis arises already after a short time of 4 – 12 weeks in approximately 35 – 45% (restenosis). In many cases

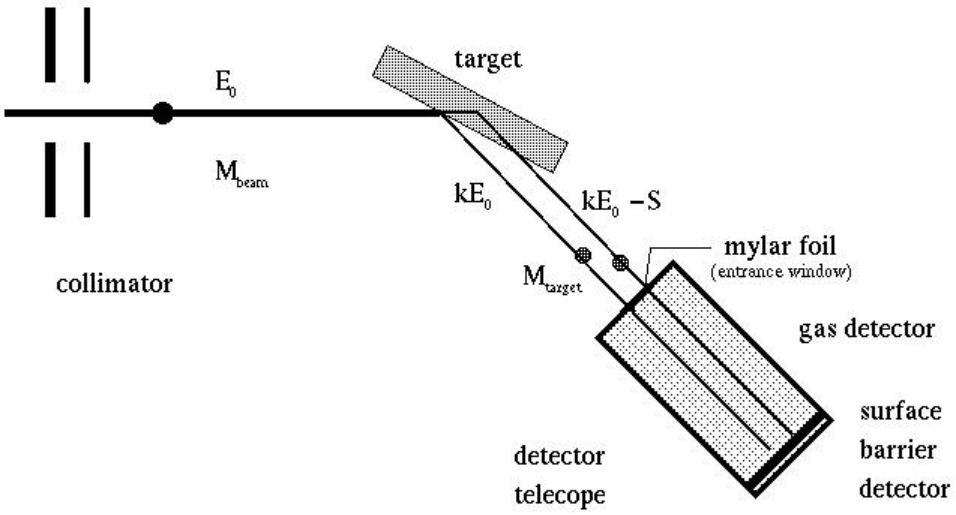

Fig. 1: Schematic view of the scattering geometry.

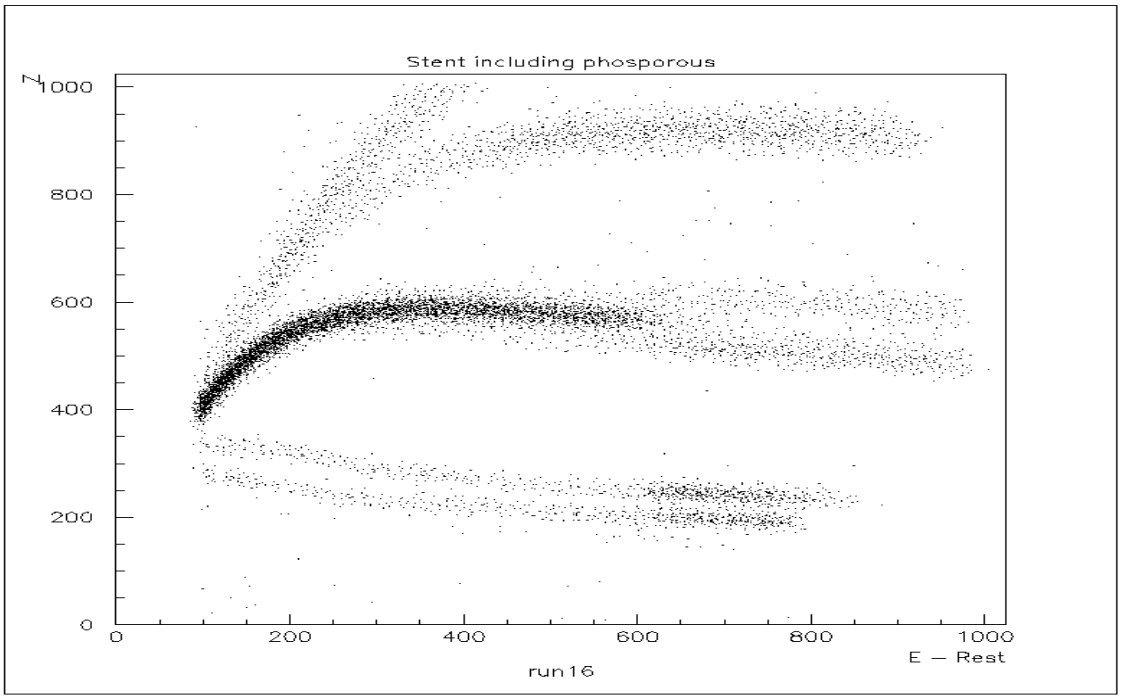

Fig. 2: Elastic recoil detection analysis (ERDA) spectrum from a coated stent. Layer contains phosphorous.

an expandable metal scaffold (stent) is placed after the PTCA in the critical area and the restenosis rate is reduced to 25%.

Arguably the most innovative and exciting recent development in interventional cardiology and radiology has been the application of ionizing radiation to prevent restenosis in arthereosclerotic vessels treated by balloon angioplasty and stenting. Prolonged low dose irradiation in the form of a beta emitting stent and brief high dose irradiation using an afterloading device has been proposed as methods [1].

The fundamental problem of the afterloading method is the high decay rate of the radioactive source. In order to achieve radiation doses of 10 – 20 Gy within a few minutes in the desired area, it is necessary to use sources with β-rates of about 10 Curie. All available emitters of β-radiation additionally have a γ-radiation share of at least 20 %. The handling of such radiating sources needs extensive effort in shielding and protection of the environment, and the exploding costs would represent a barrier for the most hospitals.

An alternative approach to temporary intravascular radiation is the use of a stent as a store for local radiation source, with an appropriate lifetime, as a mean to prevent restenosis. Here the most convenient isotope is the pure β-emitter ^{32}P with a maximum energy of 1.7 MeV and a half-life of $T_{½}$ = 14.3 days. Studies have documented that the restenosis rate can be reduced to 10 % [2,3].

There are two different ways to manufacture β-emitting stents. One way is to implant radioactive ^{32}P in the surface of the stent. The complete manufacture must be carried out in a radiation protected environment. Because of the relative short half-life of ^{32}P, production and medical application have to follow just in time.

The second way for the production of a β-emitting stent is to coat a stent with natural ^{31}P and then to activate the stent in a nuclear reactor. The aim of this project is to develop this new low cost method.

In a PVD-procedure a layer with a thickness of 1–2 µm and a content of approximately $5 \cdot 10^{17}$ ^{31}P atoms per cm² is deposited on the stent. Subsequently the stent is exposed to a neutron flux in a nuclear reactor to transform the ^{31}P into β-emitting ^{32}P. The composition of the material and the neutron flux is tuned in that way to achieve a β-activity of 50 kBq/cm^2. The value of the γ-activity is in the range of 5 kBq and a mean half-life of 50 days.

The atomic concentration profiles of the layers are analyzed by elastic recoil detection analysis (ERDA) [4, 5] at the tandem accelerator of the University of Cologne. The ERDA method is used to determine the profile of a wide range of elements simultaneously in thin layers (0.1 – 4 µm) with a depth resolution of a few hundred Å and high sensitivity. The representation of the Z value of the recoiled atoms is achieved by an ΔE-E detector-telescope. We used for the analysis a 100 MeV ^{58}Ni-beam. The general geometry is shown in Fig. 1. The ERDA method is based on elastic collision (Rutherford scattering) between an impinging ion and a target nucleus. The information about the origin in the layer of the detected (recoiled) atoms is determined by the energy loss data of charged particles in matter. A typical spectrum is shown in Fig. 2.

References

[1] Vascular Radiotherapy Monitor, No 2, 2 (1998); No 3, 1 (1999).

[2] *Low – Dose β – Particle Emission From Stent Wire. Results in Complete, Localized Inhibition of Smooth Muscle Cell Proliferation*, T.A. Fischell, B.K. Kharma, D.R. Fischell, P.G. Loges, C.W. Coffey, D.M. Duggan, A.J. Naftilan Circulation **90**, 2956-2963 (1994).

[3] *Pure β – Particle Emitting Stent Inhibit Neointima Formation in Rabbits*, C. Hehrlein, M. Stintz, R. Kinscherf, K. Schlösser, E. Huttel, L. Friedrich, P. Fehsenfeld, W. Kübler, Circulation **93**, 641-644 (1996).

[4] *Determination of concentration profiles by elastic recoil detection with a ΔE-E gas telescope and high-energy incident heavy ions*, J.P.Stoquert, G.Guillaume, M.Hage-Ali, J.J. Grob, C.Ganter, P.Siefert, Nucl. Inst. and Meth. B **44** 184 (1989).

[5] *Preparation and analysis of targets with implanted thick Ar layers for in-beam, γ - spectroscopy*, U.Grabowy, H.Busch, A.Gohla, K.-H.Speidel, S.Kremeyer, G.Jakob, K.Freitag, J.Gerber, W.Assmann Nucl. Inst. and Meth. B **101**, 422 (1995).

Publications – November 1998 to date

published:

1. *Lateral quantization of spin waves in micron size magnetic wires*
   C. Mathieu, J. Jorzick, A. Frank, S.O. Demokritov, B. Hillebrands, A.N. Slavin, B. Bartenlian, C. Chappert, D. Decanini, F. Rousseaux, E. Cambril
   Phys. Rev. Lett. **81**, 3968 (1998).
2. *Arrays of interacting magnetic dots and wires: static and dynamic properties*
   B. Hillebrands, S.O. Demokritov, C. Mathieu, S. Riedling, O. Büttner, A. Frank, B.F.P. Roos, J. Jorzick, A.N. Slawin, B. Bartenlian, C. Chappert, F. Rousseaux, D. Decanini,
   E. Cambril, A. Müller, U. Hartmann
   J. Mag. Soc. Jpn. **23**, 670 (1999).
3. *Progress in multipass tandem Fabry-Pérot interferometry: I. A fully automated, easy to use, self-aligning spectrometer with increased stability and flexibility*
   B. Hillebrands
   Rev. Sci. Instr. **70**, 1589 (1999).
4. *In-plane anomalies of the exchange bias field in $Ni_{80}Fe_{20}/Fe_{50}Mn_{50}$ bilayers on Cu(110)*
   S. Riedling, M. Bauer, C. Mathieu, B. Hillebrands, R. Jungblut, J. Kohlhepp, A. Reinders
   J. Appl. Phys. **85**, 6648 (1999).
5. *Epitaxial growth of metastable Pd(001) on bcc-Fe(001)*
   B.F.P. Roos, A. Frank, S.O. Demokritov, B. Hillebrands
   J. Magn. Magn. Mater. **198-199**, 725 (1999).
6. *Magnetic ordering and anisotropies of atomically layered Fe/Au(001) multilayers*
   S. Riedling, N. Knorr, C. Mathieu, J. Jorzick, S.O. Demokritov, B. Hillebrands
   J. Magn. Magn. Mater. **198-199**, 348 (1999).
7. *Spindynamik in magnetischen Schichten und Vielfachschichten*
   B. Hillebrands
   Beitrag zur Ferienschule "Magnetische Schichtsysteme", IFF, Forschungszentrum Jülich (1999).
8. *Collisions of spin wave envelope solitons and self-focused spin wave packets in magnetic films*
   O. Büttner, M. Bauer, S.O. Demokritov, B. Hillebrands, M.P. Kostylev, B.A. Kalinikos, A.N. Slavin
   Phys. Rev. Lett. **82**, 4320 (1999).
9. *Enhanced coercivity of exchange-biased Fe/MnPd bilayers*
   Y.J. Tang, B.F.P. Roos, T. Mewes, S.O. Demokritov, B. Hillebrands, Y.J. Wang
   Appl. Phys. Lett. **75**, 707 (1999).
10. *Biased switching of small magnetic particles*
    R.L. Stamps, B. Hillebrands
    Appl. Phys. Lett. **75**, 1143 (1999).

11. *Inelastic light scattering in magnetic dots and wires*
    S.O. Demokritov, B. Hillebrands
    J. Magn. Magn. Mater. **200**, 706 (1999).
12. *Elastic properties of thin h-BN films investigated by Brillouin light scattering*
    T. Wittkowski, J. Jorzick, K. Jung, B. Hillebrands
    Thin Solid Films **353**, 137 (1999).
13. *Collisions of spin wave envelope solitons and self-focused spin wave packets in Yttrium iron garnet films*
    O. Büttner, M. Bauer, S.O. Demokritov, B. Hillebrands, M.P. Kostylev, B.A. Kalinikos, A.N. Slavin
    Phys. Rev. Lett. **82**, 4320 (1999).

in press:

14. *Brillouin light scattering from quantized spin waves in micron-size magnetic wires*
    J. Jorzick, S.O. Demokritov, C. Mathieu, B. Hillebrands, B. Bartenlian, C. Chappert, F. Rousseaux, A.N. Slavin
    Phys. Rev. B, in press.
15. *Brillouin light scattering from layered magnetic structures*
    B. Hillebrands
    Light Scattering in Solids VII, Topic in Applied Physics **75**, Springer Verlag, in press. (will appear in November 1999).
16. *Space- and time-resolved Brillouin light scattering from nonlinear spinwave packets*
    O. Büttner, M. Bauer, A. Rueff, S.O. Demokritov, B. Hillebrands, A.N. Slavin, M.P. Kostylev, B.A. Kalinikos
    Ultrasonics, in press.
17. *Spin wave quantization and dynamic coupling in micron-size circular magnetic dots*
    J. Jorzick, S.O. Demokritov, B. Hillebrands, B. Bartenlian, C. Chappert, D. Decanini, F. Rousseaux, E. Cambril
    Appl. Phys. Lett., in press.
18. *Characterization of elastic properties of hard carbon and boron nitride films using the Brillouin light scattering technique*
    T. Wittkowski, V. Wiehn, J. Jorzick, K. Jung, B. Hillebrands
    Thin Solid Films, in press.
19. *Switching behavior of a Stoner particle beyond the relaxation time limit*
    M. Bauer, J. Fassbender, B. Hillebrands, R.L. Stamps
    Phys. Rev. B, in press.
20. *Switching behavior of Stoner-like magnetic thin film elements*
    M. Bauer, J. Fassbender, B. Hillebrands
    J. Appl. Phys., in press.

submitted:

21. *Spin dynamics in magnetic films patterned into dots and wires*
J. Jorzick, S.O. Demokritov, B. Hillebrands, B. Bartenlian, C. Chappert, F. Rousseaux, A.N. Slavin
Submitted to the Proceedings of the 2nd Int. Symp. on Frontiers in Magnetism.

22. *Spatial and spatio-temporal self-focusing of spin waves in garnet films observed by space and time-resolved Brillouin light scattering*
O. Büttner, M. Bauer, S.O. Demokritov, B. Hillebrands, Yu.S. Kivshar, V. Grimalsky, Yu. Rapoport, M.P. Kostylev, B.A. Kalinikos, A.N. Slavin
Submitted to J. Appl. Phys.

23. *Quantized spin wave modes in micron size magnetic discs*
J. Jorzick, S.O. Demokritov, B. Hillebrands, B. Bartenlian, C. Chappert, D. Decanini, F. Rousseaux, E. Cambril
submitted to J. Appl. Phys.

24. *Growth and Magnetic Properties of Fe films on vicinal to (001) substrates*
A.R. Frank, J. Jorzick, M. Rickart, M. Bauer, J. Fassbender, S.O. Demokritov, B. Hillebrands, M. Scheib, A. Keen, A. Petukhov, A. Kirilyuk, Th. Rasing
submitted to J. Appl. Phys.

25. *Oscillatory exchange bias effect in FeNi/Cu/FeMn and FeNi/Cr/FeMn trilayer systems*
T. Mewes, B.F.P. Roos, S.O. Demokritov, B. Hillebrands
submitted to J. Appl. Phys.

26. *Linear and nonlinear diffraction of dipolar spin waves in Yttrium Iron Garnet films observed by space- and time-resolved Brillouin light scattering*
O. Büttner, M. Bauer, S.O. Demokritov, B. Hillebrands, Yu.S. Kivshar, V. Grimalsky, Yu. Rapoport, A.N. Slavin
submitted to Phys. Rev. B.

27. *Suppression of exchange bias by ion irradiation*
T. Mewes, R. Lopusnik, J. Fassbender, B. Hillebrands, M. Jung, D. Engel, A. Ehresmann, H. Schmoranzer
submitted to Appl. Phys. Lett.

28. *Suppression of magnetic-field pulse-induced magnetization precession by pulse tailoring*
M. Bauer, R. Lopusnik, J. Fassbender, B. Hillebrands
submitted to Appl. Phys. Lett.

29. *Magnetization reversal in ultrashort magnetic field pulses*
M. Bauer, R. Lopusnik, J. Fassbender, B. Hillebrands
submitted to J. Magn. Magn. Mater.

Conference Contributions and Seminars

Conferences

Invited talks

J. Fassbender:
Progress in laser interference lithography for nanoscale magnetic structures
MRS Spring Meeting, San Francisco, U.S.A., April 1999

B. Hillebrands:
Characterization of elastic properties of hard and superhard coating materials using the Brillouin light scattering technique
ASIAN CVD Conference, Shanghai, China, May 1999

S.O. Demokritov:
Propagation and collision of non-linear spin wave packets in magnetic films
Moscow International Symposium on Magnetism, Moscow, Russia, June 1999

B. Hillebrands:
Space- and time-resolved Brillouin light scattering from nonlinear spinwave packets
Ultrasonics International ´99 and 1999 World Congress on Ultrasonics, Copenhagen, Danmark, June 1999

B. Hillebrands:
Spin Dynamics in Patterned Magnetic Films
2nd International Symposium on Frontiers in Magnetism, Stockholm, Sweden, August 1999

Other conference contributions

1 contribution:	43rd Annual Conference on Magnetism and Magnetic Materials, Miami, November 1998
1 contribution:	APS Spring Meeting Atlanta, March 1999
12 contributions:	Frühjahrstagung der DPG, Münster, March 1999
3 contributions:	Drei-Königs-Treffen, Bad Honnef, January 1999
1 contribution:	DFG-Rundgespräch Bad Honnef, February 1999
6 contributions:	44th Annual Conference on Magnetism and Magnetic Materials, San Jose, USA, November 1999

Spring and Summer Schools

"Magnetische Schichtsysteme", 30. Ferienkurs des Instituts für Festkörperforschung 1999, Forschungszentrum Jülich, Germany, March 1999

Lecture: *Spindynamik in magnetischen Schichten und Vielfachschichten* (B. Hillebrands)

EU-TMR Summer School on "Mesomagnetism, Spin Dynamics and Spin Electronics", Rhodes, Greece, September 1999

Lectures: *Introduction to the spin dynamics in the regime of spin precession at GHz frequencies* (B. Hillebrands)

Spin waves in patterned structures (S.O. Demokritov)

Posters: 6 contributions

Invited colloquia and seminars

B. Hillebrands, Department of Physics, University of Prague, Czech Republic, December 1998

B. Hillebrands, IPHT Jena, Germany, February 1999

B. Hillebrands, Oakland University, Rochester, U.S.A., March 1999

B. Hillebrands, Universität Mainz, Germany, May 1999

M. Bauer, SRCAMMP Seminar, Perth, Australia, December 1998

T. Wittkowski, University of Ferrara, Italy, January 1999

J. Jorzick, Institute of Physics of the Czech Academy of Sciences, Prague, Czech Republic, May 1999

J. Fassbender, Laboratoire des Physique des Materiaux UMR-CNRS, Nancy, France, June 1999

O. Büttner, Oakland University, Rochester, U.S.A., October 1999

S.O. Demokritov, Universität Erlangen, Germany, July 1999

Contributions at other meetings

T. Wittkowski, J. Jorzick, K. Jung, B. Hillebrands

Brillouin-Lichtstreuung zur Untersuchung der elastischen Eigenschaften dünner c-BN Schichten

c-BN Expertentreffen, Stockerau, June 1999

EU-TMR Summer School

"Mesomagnetism, Spin Dynamics and Spin Electronics"

Rhodes, Greece, September 1999

back row: Stefan Poppe, André Frank, Martin Bauer, Dr. Jürgen Fassbender, Tim Mewes

front row: Marc Rickart, Dr. Alexandra Mougin, Björn Roos, Jörg Jorzick, Prof. Dr. Burkard Hillebrands

on the ground: Radek Lopusnik

Lectures: *Introduction to the spin dynamics in the regime of spin precession at GHz frequencies* (B. Hillebrands)

Spin waves in patterned structures (S.O. Demokritov)

Posters: *Switching behavior of a Stoner particle beyond the relaxation time limit* (M. Bauer, J. Fassbender, B. Hillebrands)

Switching behavior of Stoner-like magnetic thin film elements (M. Bauer, J. Fassbender, B. Hillebrands)

A time resolved magneto-optical Kerr effect magnetometer (M. Bauer, R. Lopusnik, J. Fassbender, B. Hillebrands)

Progress in laser interference lithography for magnetic nanostructures (S. Poppe, P. Kimmel, M. Bauer, J. Fassbender, B. Hillebrands)

Oscillatory exchange bias effect in FeNi/Cu/FeMn and FeNi/Cr/FeMn trilayer systems (T. Mewes, B.F.P. Roos, S.O. Demokritov, B. Hillebrands)

Spin wave quantization in micron size patterned magnetic dots and wires (J. Jorzick, C. Mathieu, S.O. Demokritov, B. Hillebrands, A.N. Slavin, B. Bartenlian, D. Decanini, F. Rousseaux)